Non-Local Correlations within Dynamical Mean Field Theory

Dissertation

zur
Erlangung des Doktorgrades (Dr. rer. nat.)
der
Mathematisch-Naturwissenschaftlichen Fakultaet
der
Rheinischen Friedrich-Wilhelms-Universität Bonn

vorgelegt von
Li, Gang

aus
Liaoning, P.R. China

Bonn (October, 2008)

Tag der Promotion: 20. February 2009

Erscheinungsjahr 2009

Angefertigt mit Genehmigung der Mathematisch-Naturwissenschaftlichen Fakultät der Rheinischen Friedrich-Wilhelms-Universität Bonn

Referent: Prof. Dr. Hartmut Monien
Korreferent: Prof. Dr. Rainald Flume

Contents

Chapter 1

Introduction

To understand the properties of many-body interacting systems is one of the fundamental problems in condensed matter physics. Many solids are well explained by either the tight-binding theories or the mean field (especially the time-independent) treatment of the Coulomb interaction between electrons. These weak-coupling methods have been proven to satisfactorily describe the material properties when the electron-electron interaction is not strong. Various band structure theories, for example the density functional theory (DFT), especially the local density approximation (LDA), can make precise predictions for many materials with only demanding of crystal structure parameters. The energy band theory identifies the metal and insulator in terms of the filled or partially filled energy band which always characterizes the system as metal when it is half filled. The discovery of the transition-metal oxides like V_2O_3 [Rice and McWhan (1970)] shows the transition between metal and insulator which is not expected from the band theory. Mott pointed out that this is due to the electron-electron interaction which could make a crystal insulating even if the energy band is half filled [Mott (1968)]. The strongly interacting nature of some materials can generate complicated phases, like this "unusual[1]" metal insulator transition, superconducting and magnetically ordered state, localization. More and more theoretical methods try to go beyond the band theory to explicitly include the interaction effect between electrons. Based on the Hubbard model which explicitly includes the interaction effect between the two electrons which stay on the same crystal site[2], a lot theoretical and numerical methods are developed to understand the competition between the itinerant nature of the electrons and the Coulomb interaction effect. Weakly correlated systems can be described by the mean field or the perturbative method, like various diagram expansion methods. The strongly interacting system can be described by mapping the Hubbard model to the effective $t-J$ model or performing the atomic expansion. While the intermediate interaction region is difficult to access by these methods.

To seriously understand the metal-insulator transition induced by the Coulomb effect between electrons, we need a non-perturbative method with respect to the electron interaction. In this sense, Dynamical Mean-Field Theory (DMFT) [Georges *et al.*

[1] Now it is called the Mott insulator which is caused by the strong electron interaction.

[2] This is simplest Hubbard model which only considers the on-site Coulomb interaction. The more general description of the Hubbard model is given in the reference. [Hubbard (1963)]

(1996)] is a reliable method for describing the electronic correlations. It correctly yields a weakly correlated metal, a strongly correlated metal, or a Mott insulator. DMFT is exact in the infinite dimension (or coordination number) limit by mapping an interacting electron system to an impurity embedded in the non-interacting bath. The thermal fluctuation is treated exactly while the spatial fluctuation is taken in a mean field level. The combination of LDA and DMFT has been successfully applied to the band structure calculation to understand the strongly correlated materials.

The major flaw of DMFT is the neglect of the spacial fluctuation. To go beyond the local approximation of DMFT, some cluster extentions of DMFT have been proposed, for a review see [Maier *et al.* (2005)]. The demand of computational resources for accessing the larger system becomes heavy with the increase of system size. The long-range correlation therefore is hard to consider. In this thesis, we are going to introduce a more easy and reliable method which can take the short and long range correlation on a equal footing with less computational burden.

Outline

The main topic of this thesis is the determination of the non-local corrections to DMFT. This thesis is organized in the following way:

In Chapter 1 we offer an very simple introduction of the Hubbard model focusing on the conceptual explanation of the Metal-Insulator transition. The atomic Hubbard model was solved exactly with the help of the partition function, some useful matrix notations were introduced as a preparation for later use.

Chapter 2 gives a detailed derivation of the single site and cluster DMFT equations. The cavity construction and the locator expansion methods are adopted, which are basically similar to each other. The approximation introduced in DMFT is analyzed. Both C-DMFT and DCA are then formulated in real space in order to show the comparison between them. The DCA equations can be tranformed to the widely used form by diagonalizing the one particle matrix. One simple but useful example is given for both the C-DMFT and DCA to show their difference.

In Chapter 3 two variants of the continuous-time Quantum Monte Carlo method (CTQMC) are described in detail. The general formulism is presented before going into the details of the weak and strong-coupling CTQMC. These methods are powerful finite temperature solvers of the DMFT equations. The low temperature and strong interaction regime can be accessed by these methods relatively easily compared to the other methods, for example the Hirsch Fye method. The performance of these methods were discussed in a two-layer Hubbard model example.

The extensions of DMFT to include the long range correlation effect are given in Chapter 4, including the dual fermion (DF) method and the dynamical vertex approximation (DΓA). They base on the lowest order vertex correction to the DMFT, where we only consider the vertex from the two-particle scattering process. The single and two particle properties are studied, the comparison to the larger cluster DMFT results shows the good performance of these methods. The less demand on the computational resources and the ability to access the long range correlation are the major advantages of these methods compared to the general cluster extensions of DMFT. The DF method has a better convergence and effectively weak-coupling

nature compared to DΓA, which indicates the better convergence and effectively weak-coupling nature of this method.

In the last chapter, the frustration effect on the Metal-Insulator transition is studied in a triangular system. The first order metal to insulator transition is identified by the jump of the double occupancy. The non-local correlations seriously reduce the critical interaction in the triangular system where one might think the single site DMFT would be sufficient for describing this frustrated system. The competition between different magnetic orders in the insulating phase is observed. There is a (π, π) anti-ferromagnetic insulator to 120-degree state transition at larger frustration regime. The bilayer Hubbard model was also studied as an toy model of the High-Tc superconductor. The low temperature phase diagram was given for both the single site DMFT and C-DMFT calculations focusing on the paramagnetic metal to paramagnetic insulator transition.

1.1 Hubbard Model: Atomic limit

Being an exactly solvable model, the atomic Hubbard model contains some basic properties of strongly corrected electron systems. There is no electron hopping term in this model. To solve more complicated models, one needs to rely on analytical approximation or numerical methods. Due to the absence of the electron movement, the atomic Hubbard model is completely controlled by Coulomb interaction effect. It provides us a very simple way to understand the interaction-driven metal insulator transition. In this section, we will show some basic notations and results for the atomic Hubbard model, including the total particle density, double occupancy, total energy and the one particle Green's function. Let us start from the discussion of the partition function of this model.

The Hilbert space in this case has dimension four, with the basis $|0>, |\uparrow>, |\downarrow>$, $|\uparrow\downarrow>$ which correspond to no particle, one spin-up, one spin-down and doubly occupied states. The Hamiltonian of the atomic Hubbard model has no kinetic term which can be written as:

$$H = Un_{\uparrow}n_{\downarrow} - \mu(n_{\uparrow} + n_{\downarrow}) \tag{1.1}$$

The above particle number basis is also the eigenbasis of the atomic Hubbard model with the eigenvalues $0, -\mu, -\mu, -2\mu + U$. Then the partition function is given as

$$\mathcal{Z} = Tre^{-\beta H} = 1 + 2e^{\beta\mu} + e^{-\beta(U-2\mu)}. \tag{1.2}$$

In principle, once the partition function is known to us, we can determine every property, for example the one particle Greeen's function, the density of state, etc. from it.

1.2 Total particle density

The total particle density is defined as $\langle n \rangle = \langle n_{\uparrow} + n_{\downarrow} \rangle = \langle n_{\uparrow} \rangle + \langle n_{\downarrow} \rangle$. To make our derivation easily understood and also do some preparations for later use, we write

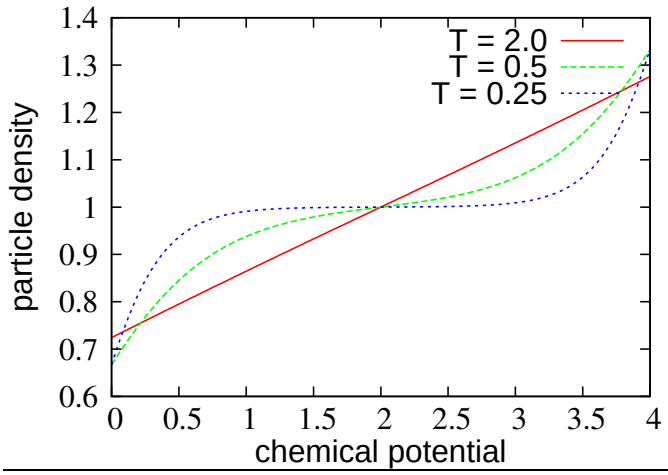

Figure 1.1: *Density of particles in the single site Hubbard model as a function of chemical potential. The jump of chemical potential indicates a transition between metal and insulator.*

down the creation and elimination operator in the above particle number basis as

$$c_\uparrow^\dagger = \begin{pmatrix} 0 & 0 & 0 & 0 \\ 1 & 0 & 0 & 0 \\ 0 & 0 & 0 & 0 \\ 0 & 0 & 1 & 0 \end{pmatrix}, c_\downarrow^\dagger = \begin{pmatrix} 0 & 0 & 0 & 0 \\ 0 & 0 & 0 & 0 \\ 1 & 0 & 0 & 0 \\ 0 & 1 & 0 & 0 \end{pmatrix} \tag{1.3}$$

With the help of the above definition, we can explicitly evaluate the trace in the thermal average.

$$\begin{aligned} \langle n_\uparrow \rangle &= \frac{1}{\mathcal{Z}} Tr[e^{-\beta H} c^\dagger c] \\ &= \frac{1}{\mathcal{Z}} Tr \begin{pmatrix} 1 & 0 & 0 & 0 \\ 0 & e^{\beta\mu} & 0 & 0 \\ 0 & 0 & e^{\beta\mu} & 0 \\ 0 & 0 & 0 & e^{-\beta(U-2\mu)} \end{pmatrix} \times \begin{pmatrix} 0 & 0 & 0 & 0 \\ 0 & 1 & 0 & 0 \\ 0 & 0 & 0 & 0 \\ 0 & 0 & 0 & 1 \end{pmatrix} \\ &= \frac{(e^{\beta\mu} + e^{2\beta\mu - \beta U})}{1 + 2e^{\beta\mu} + e^{2\beta\mu - \beta U}} \end{aligned} \tag{1.4}$$

It is easy to prove that the spin down particle density has exactly the same form. Then the total particle density is

$$\langle n \rangle = \langle n_\uparrow \rangle + \langle n_\downarrow \rangle = \frac{2(e^{\beta\mu} + e^{2\beta\mu - \beta U})}{1 + 2e^{\beta\mu} + e^{2\beta\mu - \beta U}}. \tag{1.5}$$

Note that in the atomic Hubbard model we do not have any hopping term, all the interesting physics is directly introduced by the Coulomb interaction. A very important phenomenon of this kind of interaction is the so-called Mott transition. It is different from the transition between metal and band insulator which is caused by the different filling of particles. This kind of transition can not be explained by the traditional band theory. It is one of the typical phenomenon in the strongly correlated electron systems. It is also the central topic of this thesis which will be discussed in more detail later. Based on the atomic Hubbard model, we want to

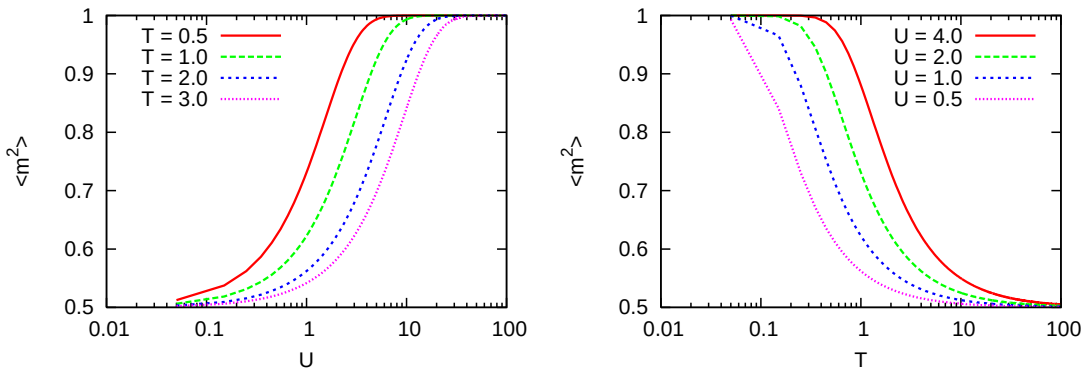

Figure 1.2: *Local moment as a function of temperature T and interaction U. At strong-coupling and low temperature region, the local moment forms and takes the value of 1.*

look for insights into this kind of transition. In Fig. 1.1, we calculate the average particle number as a function of chemical potential at $U/t = 4.0$. In this diagram, one can see clearly that the transition from metal to insulator appears with the decrease of the temperature. With the lowering of temperature, the particle density curve shows a platform at $\langle n \rangle \approx 1$. In this case in order to increase the particle density, more energy is needed to overcome the energy gap. In Fig. 1.1, $T = 2.0$ case corresponds to metal. When T decreases to 0.25, the energy gap forms completely.

1.3 Local moment and total energy

Another important indicator of Mott type metal insulator transition is the formation of the local moment. The local moment is definition as $< m^2 > = < (n_\uparrow - n_\downarrow)^2 >$. In the classical limit, the local moment takes the value of zero for the states $|0>$ and $|\uparrow\downarrow>$, but takes the value of 1 for $|\uparrow>$ and $|\downarrow>$. When the spin-up and spin-down particles have different filling density, the local moment has a non-zero value, which means the net spin is non-zero. The system is in a magnetic state. Therefore the local moment can be viewed as magnetic order parameter.

$$\langle m^2 \rangle = \langle (n_\uparrow - n_\downarrow)^2 \rangle = \langle n \rangle - 2\langle n_\uparrow n_\downarrow \rangle = \frac{2e^{\beta\mu}}{1 + 2e^{\beta\mu} + e^{2\beta\mu - \beta U}} \tag{1.6}$$

Fig. 1.2 shows the local moment as a function of temperature and interaction respectively. From this diagram, we can see that at low temperature and strong interaction region, the local moment forms which takes the value of 1. The system only has two possible occupied states $|\uparrow>$ and $|\downarrow>$. No empty and doubly occupied state exist. But at weak-coupling and high temperature regime, all the four basis states have the same probability to be occupied. Therefore, the local moment takes the value of 0.5[3]. In this case, the system is totally disordered. In the lower temperature and strong interaction regime, there is an energy gap caused by the Coulomb

[3]In this single site Hubbard model, the Hilbert space has four basis states, any state has a probability of 0.25 to be occupied in this case.

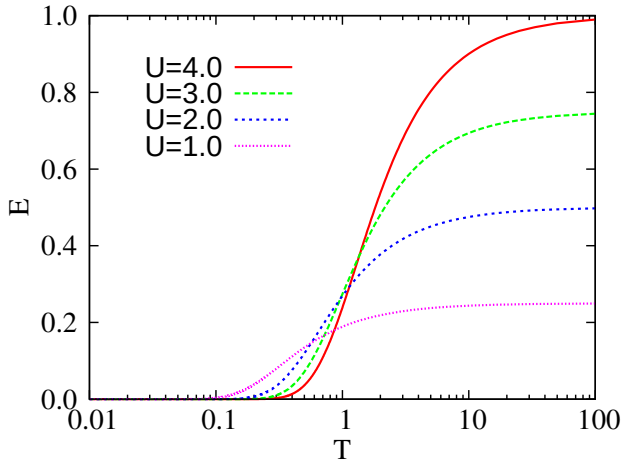

Figure 1.3: *Total energy of the atomic Hubbard model as a function of temperature at four different interaction* $U/t = 1.0, 2.0, 3.0, 4.0$

interaction. It requires amount of energy to make two particles stay on the same site. Therefore, only a singly occupied state exists in this case, where we observed the formation of local moment. At half filling case, each crystal site is occupied by one electron which is forbidden to move freely by the interaction between electrons. The system is in the insulating phase.

The total energy is another useful observable to characterize the metal-insulator transition. It contains two parts, the kinetic energy and potential energy. Since we are considering the atomic Hubbard model which does not have the hopping terms, the total energy equals the potential energy.

$$E = \langle H + \mu n \rangle = \frac{U e^{2\beta\mu - \beta U}}{1 + 2e^{\beta\mu} + e^{2\beta\mu - \beta U}} \tag{1.7}$$

As shown in figure 1.3, we can see the total energy becomes zero from a finite value with the decrease of temperature. Since the total energy is just the potential energy which is always positive in this model, the zero value of total energy in the low termperature regime indicateds the doubly occupied state is completely suppressed. At half filling average particle density is one. Each site is averagely occupied by one particle, the absence of the doubly occupied state means the particle can not move freely. Therefore the system is an insulator. In contrast, at high temperature regime, the total energy tends to be constant with the increase of temperature. And this value is proportional to the interaction strength U. As we know that each of the four states has the same probability to be occupied which is 0.25 at the high temperature regime. This disordered state does not change with a further increase of the temperature. This effect is clearly seen from Fig. 1.3.

1.4 Green's function

In the previous section, the Mott transition based on the Hubbard model has been shown from the jump of chemical potential, the formation of local moment and the change of total energy. In this section, we want to study this phenomenon with the help of the Green function. The imaginary part of the one particle Green's

function has a close relation with the density of states, which will directly show us the formation of the energy gap in the insulating state.

The Green's function can be determined by two ways. One way uses the partition function method to evaluate the thermal average in the Green's function definition. The other way is the equation of motion method. Here, we adopt the first one. Firstly, let us introduce the definition of the Green function in imaginary time space:

$$G_\sigma(\tau-\tau') = -<T_\tau c_\sigma(\tau)c_\sigma^\dagger(\tau')> \tag{1.8}$$

here, T_τ is time ordering operator and the creation/annihilation operator is defined in the Heisenberg picture.

$$c^\dagger(\tau)/c(\tau) = e^{H\tau}c^\dagger/ce^{-H\tau} \tag{1.9}$$

The definition of the Green's function breaks into two parts with respect to the time ordering operator.

$$G_\sigma(\tau-\tau') = \begin{cases} -c_\sigma(\tau)c_\sigma^\dagger(\tau') & if \quad \tau > \tau' \\ c_\sigma^\dagger(\tau')c_\sigma(\tau) & if \quad \tau' > \tau \end{cases} \tag{1.10}$$

It can be written in another form,

$$G_\sigma(\tau-\tau') = \theta(\tau-\tau')<c_\sigma(\tau)c_\sigma^\dagger(\tau')> -\theta(\tau'-\tau)<c_\sigma^\dagger(\tau')c_\sigma(\tau)> \tag{1.11}$$

In fact, the absolute time has no meaning, we are only interested in the time difference. Green function represents the propagation of one particle from imaginary time τ' to τ. If we expand the creation/annihilation operator in Heisenberg picture,

$$c_\sigma(\tau)c_\sigma^\dagger(\tau') = e^{H\tau}c_\sigma e^{-H(\tau-\tau')}c_\sigma^\dagger e^{-H\tau'} \tag{1.12}$$

Under the tracing operation, the above Green function definition is same as

$$G_\sigma(\tau-\tau') = -<T_{\tau-\tau'}c_\sigma(\tau-\tau')c_\sigma^\dagger> \tag{1.13}$$

Therefore, normally, we can shift the creation time of particle to zero and the definition of Green function looks like:

$$G_\sigma(\tau) = -<T_\tau c_\sigma(\tau)c_\sigma^\dagger> \tag{1.14}$$

The evaluation of the Green's function from the partition function is easily done in the matrix form introduced above. With the help of the Heisenberg operator definition, we have

$$\begin{aligned} G_\uparrow(\tau) &= -\frac{1}{\mathcal{Z}}Tr[e^{-\beta H}c_\uparrow(\tau)c_\uparrow^\dagger] = \frac{1}{\mathcal{Z}}Tr[e^{-(\beta-\tau)H}c_\uparrow e^{-H\tau}c_\uparrow^\dagger] \\ &= Tr\begin{pmatrix} 1 & 0 & 0 & 0 \\ 0 & e^{(\beta-\tau)\mu} & 0 & 0 \\ 0 & 0 & e^{(\beta-\tau)\mu} & 0 \\ 0 & 0 & 0 & e^{-(\beta-\tau)(U-2\mu)} \end{pmatrix} \times \begin{pmatrix} 0 & 1 & 0 & 0 \\ 0 & 0 & 0 & 0 \\ 0 & 0 & 0 & 1 \\ 0 & 0 & 0 & 0 \end{pmatrix} \\ &\quad \times \begin{pmatrix} 1 & 0 & 0 & 0 \\ 0 & e^{\tau\mu} & 0 & 0 \\ 0 & 0 & e^{\tau\mu} & 0 \\ 0 & 0 & 0 & e^{-\tau(U-2\mu)} \end{pmatrix} \times \begin{pmatrix} 0 & 0 & 0 & 0 \\ 1 & 0 & 0 & 0 \\ 0 & 0 & 0 & 0 \\ 0 & 0 & 1 & 0 \end{pmatrix} \\ &= -\frac{e^{\tau\mu} + e^{(\beta-\tau)\mu}e^{-\tau(U-2\mu)}}{1+2e^{\beta\mu}+e^{2\beta\mu-\beta U}} \end{aligned} \tag{1.15}$$

The corresponding frequency Green's function can be obtained by Fourier transform

$$G_\uparrow(i\omega_n) = \int_0^\beta e^{i\omega_n\tau} G_\uparrow(\tau) = \frac{1}{\mathcal{Z}}[\frac{1+e^{\beta\mu}}{i\omega_n+\mu} + \frac{e^{\beta\mu}+e^{-\beta(U-2\mu)}}{i\omega_n+\mu-U}] \tag{1.16}$$

Note that $(1+e^{\beta\mu})/\mathcal{Z} = 1-\langle n_\downarrow\rangle$, $(e^{\beta\mu}+e^{-\beta(U-2\mu)})/\mathcal{Z} = \langle n_\downarrow\rangle$, so the imaginary frequency Green's function with spin-σ can be further written as

$$G_\sigma(i\omega_n) = \frac{1-\langle n_{\bar\sigma}\rangle}{i\omega_n+\mu} + \frac{\langle n_{\bar\sigma}\rangle}{i\omega_n+\mu-U} \tag{1.17}$$

Fig. 1.4 shows the imaginary time Green's function at $U/t = 4.0$ and four different temperatures. With the decrease of temperature, $G(\beta/2)$ becomes zero from a finite value which indicates the metal-insulator transition.

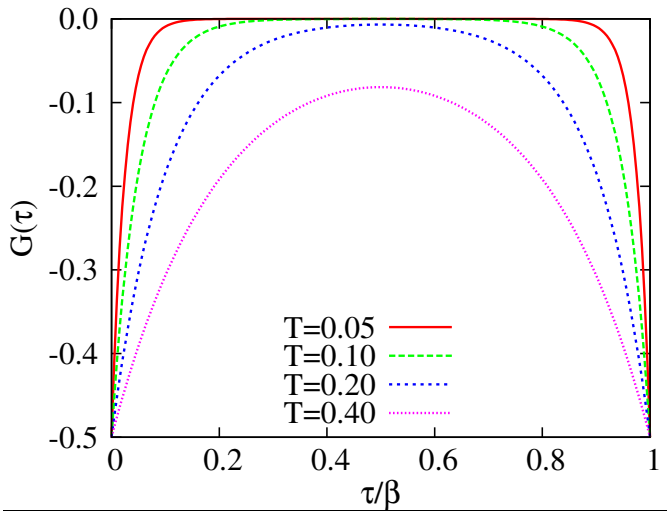

Figure 1.4: *Imaginary time Green's function of the atomic Hubbard model at $U/t = 4.0$ for various temperature.*

Single particle Green function has a very important feature in that its imaginary part has a relation with the density of state which can be obtained directly from experimental observation.

$$A(\omega) = -\frac{1}{\pi}\Im G(\omega+i0^\dagger) \tag{1.18}$$

$G(\omega+i0^\dagger)$ is the analytic continuation of $G(i\omega_n)$

$$G(\omega+i0^\dagger) = \mathcal{P}\frac{1-n_{-\sigma}}{\omega+\mu} + \mathcal{P}\frac{n_{-\sigma}}{\omega+\mu-U} - i\pi[(1-n_{-\sigma})\delta(\omega+\mu) + n_{-\sigma}\delta(\omega+\mu-U)]^4 \tag{1.19}$$

As one can see, the spectral density only has nonzero value only at two points, μ and $\mu-U$. The energy gap U in the density of state clearly shows the insulating nature of this system. In the later chapters, we will see that these two δ-function will be broadened to energy band, namely the lower and upper Hubbard band, and Mott transition will occur at some finite critical Coulomb interaction instead of at zero value.

[4] $\mathcal{P}$ denotes a Cauchy principal value. $\frac{1}{\omega\pm i\eta} = \mathcal{P}\frac{1}{\omega} \mp i\pi\delta(\omega)$

Chapter 2

Dynamical Mean Field Theory and Its Cluster extensions

This chapter provides a review of the dynamical mean field theory (DMFT), which is exact in the infinite coordination number limit. There are several ways to derive the DMFT equations, we give a detailed derivation here by using the cavity construction.

The Hubbard model and its variants have been taken as the standard model to study the essential physics of the strongly correlated system. Various attempts have been proposed to solve this type of Hamiltonian. Random Phase Approximation (RPA), Fluctuation Exchange approximation (FLEX) [Bickers *et al.* (1989); Bickers and White (1991)] and Two-Particle Self-Consistent Approximation (TPSC) [Allen and Tremblay (1995); Vilk *et al.* (1994)] are the perturbative methods basing on the certain diagram summation technique. They have been proven as weak-coupling methods. These methods suffer the same problem that they are only valid within a certain limit with respect to the Coulomb interaction U. The intermediate regime cannot be precisely described by these analytical methods. For this reason the well controlled numerically exact methods like Exact Diagonalization (ED) and Quantum Monte Carlo (QMC) have been widely accepted. They basically diagonalize the Hamiltonian for a small size system, each property within this small system can be determined exactly. The whole Coulomb interaction range can be visited by these methods. But these methods encounter another problem that the computational burden grows rapidly with the lattice size. Only a number of degrees of freedom can be considered, and furthermore the finite size inhibits the study of the low temperature region because of the finite size gaps in the low energy spectrum.

Compared to the above methods and their limitations, DMFT [Georges *et al.* (1996)] provides another non-perturbative way to study the Hubbard model and it has a well defined thermal dynamic limit. DMFT maps a many-body interacting system to an impurity embedded in a non-interacting bath which is determined self-consistently. DMFT was first proposed in 1989 by Metzner and Mueller Hartmann in the limit of infinite dimension [Metzner and vollhardt (1989); Mueller-Hartmann (1984)]. The resulting dynamics are purely local in this limit. The DMFT equations can be solved by various well controlled numerical method, like ED and QMC.

2.1 DMFT equation - Cavity Method

Now we are going to derive the DMFT equations for the many-body interacting system. Take the single band Hubbard Model as example:

$$H = -\sum_{<i,j>,\sigma} t_{ij}(c^{\dagger}_{i\sigma}c_{j\sigma} + h.c.) + U\sum_{i} n_{i\uparrow}n_{i\downarrow} - \mu\sum_{i} n_i \tag{2.1}$$

$c/c^{\dagger}$ are the creation and annihilation operators which generate/eliminate an electron at a specific site. The Coulomb interaction is restricted between the on-site spin-up and spin-down electrons.

It is convenient to write partition function (2.1) as a functional integral over the Grassman variables:

$$\mathcal{Z} = \int \prod_{i} \mathcal{D}c^{\dagger}_{i\sigma}\mathcal{D}c_{i\sigma}\exp(-S) \tag{2.2}$$

with the total action given as:

$$S = \int_0^{\beta}\left[\sum_{i,\sigma} c^{\dagger}_{i\sigma}(\tau)(\frac{\partial}{\partial\tau} - \mu)c_{i\sigma}(\tau) - \sum_{ij,\sigma} t_{ij}(c^{\dagger}_{i\sigma}(\tau)c_{j\sigma}(\tau) + h.c.) + U\sum_{i} n_{i\uparrow}(\tau)n_{i\downarrow}(\tau)\right] \tag{2.3}$$

In the "cavity construction", the full lattice is divided into two parts. One is the action for the given site which can be seen as a "cavity" after removing it and its adjacent bonds, the other part is the remaining of the full lattice. So the full action is broken into three parts, which correspond to the cavity site (S_0), the inter-site interaction between the cavity site and the rest of the system (ΔS), and the lattice action in the presence of the cavity ($S^{(0)}$).

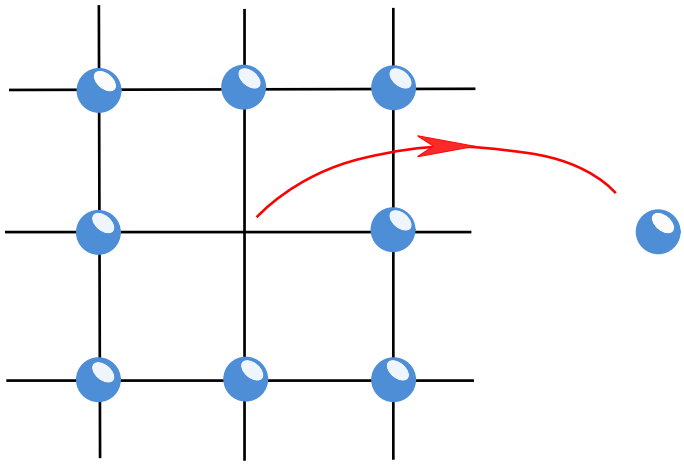

Figure 2.1: *Cavity created in the full lattice by removing a single site and its adjacent bonds.*

$$S_0 = \int_0^{\beta} d\tau\left[\sum_{\sigma} c^{\dagger}_{0\sigma}(\tau)(\frac{\partial}{\partial\tau} - \mu)c_{0\sigma}(\tau) + Un_{0\uparrow}(\tau)n_{0\downarrow}(\tau)\right] \tag{2.4}$$

$$\Delta S = -\int_0^{\beta} d\tau\sum_{i,\sigma}\left[t_{i0}c^{\dagger}_{i\sigma}(\tau)c_{0\sigma}(\tau) + t_{0i}c^{\dagger}_{0\sigma}(\tau)c_{i\sigma}(\tau)\right] \tag{2.5}$$

$$S^{(0)} = \int_0^\beta d\tau \left[\sum_{i\neq 0,\sigma} c^\dagger(\tau)(\frac{\partial}{\partial\tau} - \mu)c_{i\sigma}(\tau) - \sum_{i,j\neq 0,\sigma} t_{ij}(c^\dagger_{i\sigma}(\tau)c_{j\sigma}(\tau) + h.c.) \right] \quad (2.6)$$

The partition function can be written as:

$$\mathcal{Z} = \int \prod_i \mathcal{D}c^\dagger_{i\sigma}\mathcal{D}c_{i\sigma} \exp\left[-S_0 - \Delta S - S^{(0)}\right] \quad (2.7)$$

Now, let us integrate over the degrees of freedom of all sites except for the cavity (labeled as 0) in the partition function.

$$\mathcal{Z} = \int \mathcal{D}c^\dagger_{0\sigma}\mathcal{D}_{0\sigma} \exp\left[-S_0\right] \int \prod_{i\neq 0} \mathcal{D}c^\dagger_{i\sigma}\mathcal{D}c_{i\sigma} exp\left[-S^{(0)} - \Delta S\right] \quad (2.8)$$

here $\Delta S = -\int_0^\beta d\tau \Delta S(\tau)$, where $\Delta S(\tau) = \sum_{i,\sigma}\left[t_{i0}c^\dagger_{i\sigma}(\tau)c_{0\sigma}(\tau) + t_{0i}c^\dagger_{0\sigma}c_{i\sigma}(\tau)\right]$. To perform the integral over the bath degrees of freedom, we do the series expansion over $\exp\left[\int_0^\beta d\tau \Delta S(\tau)\right]$ which can be written as:

$$\exp\left[\int_0^\beta d\tau \Delta S(\tau)\right] = 1 + \int_0^\beta d\tau \Delta S(\tau) + \frac{1}{2!}\int_0^\beta d\tau_1 \int_0^\beta d\tau_2 \left[T_\tau \Delta S(\tau_1)\Delta S(\tau_2)\right] + \cdots \quad (2.9)$$

Now the total action becomes

$$\begin{aligned}
\mathcal{Z} &= \int \mathcal{D}c^\dagger_{0\sigma}\mathcal{D}_{0\sigma} \exp\left[-S_0\right] \int \prod_{i\neq 0} \mathcal{D}c^\dagger_{i\sigma}\mathcal{D}c_{i\sigma} exp\left[-S^{(0)}\right] \left(1 - \int_0^\beta d\tau \Delta S(\tau)\right. \\
&\quad \left. + \frac{1}{2!}\int_0^\beta d\tau_1 \int_0^\beta d\tau_2 \left[T_\tau \Delta S(\tau_1)\Delta S(\tau_2)\right] + \cdots \right) \\
&= \int \mathcal{D}c^\dagger_{0\sigma}\mathcal{D}_{0\sigma} exp\left[-S_0\right] \mathcal{Z}^{(0)} \left(1 - \int_0^\beta d\tau < \Delta S(\tau) >^{(0)}\right. \\
&\quad \left. + \frac{1}{2!}\int_0^\beta d\tau_1 \int_0^\beta d\tau_2 < T_\tau \Delta S(\tau_1)\Delta S(\tau_2) >^{(0)} + \cdots \right)
\end{aligned} \quad (2.10)$$

Where $\mathcal{Z}^{(0)} = \int \prod_{i\neq 0} \mathcal{D}c^\dagger_{i\sigma}\mathcal{D}c_{i\sigma} exp\left[-S^{(0)}\right]$, it is the partition function of the lattice in the presence of the cavity. And $<>^{(0)}$ means average over $\mathcal{Z}^{(0)}$. The condition that free-energy should be minimized makes all the odd terms in the bracket to be zero. So one can easily see that the lowest contribution is from the second term, which

reads:

$$\begin{aligned}
&\frac{1}{2!}\int_0^\beta d\tau_1\int_0^\beta d\tau_2\big\langle T_\tau \Delta S(\tau_1)\Delta S(\tau_2)\big\rangle^{(0)} \\
=\;& \frac{1}{2!}\int_0^\beta d\tau_1\int_0^\beta d\tau_2\Big\langle T_\tau \sum_{i,\sigma}\Big[t_{i0}c^\dagger_{i\sigma}(\tau)c_{0\sigma}(\tau)+t_{0i}c^\dagger_{0\sigma}(\tau)c_{i\sigma}(\tau)\Big] \\
&\qquad\qquad \times\sum_{j,\sigma}\Big[t_{j0}c^\dagger_{j\sigma}(\tau)c_{0\sigma}(\tau)+t_{0j}c^\dagger_{0\sigma}(\tau)c_{j\sigma}(\tau)\Big]\Big\rangle^{(0)} \\
=\;& \frac{1}{2!}\int_0^\beta d\tau_1\int_0^\beta d\tau_2\Big\langle \sum_{ij,\sigma} T_\tau\Big[t_{i0}t_{0j}c^\dagger_{i\sigma}(\tau_1)c_{0\sigma}(\tau_1)c^\dagger_{0\sigma}(\tau_2)c_{j\sigma}(\tau_2) \\
&\qquad\qquad +t_{0i}t_{j0}c^\dagger_{0\sigma}(\tau_1)c_{i\sigma}(\tau_1)c^\dagger_{j\sigma}(\tau_2)c_{0\sigma}(\tau_2)\Big]\Big\rangle^{(0)}
\end{aligned} \tag{2.11}$$

Now, we will show that the two parts in the bracket are equal. As for the first part, one can take $\tau_1 > \tau_2$, which becomes that

$$\begin{aligned}
&\int_0^\beta d\tau_1\int_0^{\tau_1} d\tau_2\Big\langle \sum_{ij,\sigma} T_\tau\Big[t_{i0}t_{0j}c^\dagger_{i\sigma}(\tau_1)c_{0\sigma}(\tau_1)c^\dagger_{0\sigma}(\tau_2)c_{j\sigma}(\tau_2)\Big]\Big\rangle^{(0)} \\
=\;& \int_0^\beta d\tau_1\int_0^{\tau_1} d\tau_2\sum_\sigma c^\dagger_{0\sigma}(\tau_2)\sum_{ij}t_{i0}t_{0j} < c_{j\sigma}(\tau_2)c^\dagger_{i\sigma}(\tau_1) >^{(0)} c_{0\sigma}(\tau_1)
\end{aligned} \tag{2.12}$$

Because τ_1 and τ_2 are only dummy arguments, we can exchange them freely, which results in

$$\int_0^\beta d\tau_2\int_0^{\tau_2} d\tau_1\sum_\sigma c^\dagger_{0\sigma}(\tau_1)\sum_{ij}t_{i0}t_{0j} < c_{j\sigma}(\tau_1)c^\dagger_{i\sigma}(\tau_2) >^{(0)} c_{0\sigma}(\tau_2) \tag{2.13}$$

At the same time, in the condition of $\tau_1 < \tau_2$, the second part in the bracket becomes

$$\int_0^\beta d\tau_2\int_0^{\tau_2} d\tau_1\sum_\sigma c^\dagger_{0\sigma}(\tau_1)\sum_{ij}t_{0i}t_{j0} < c_{j\sigma}(\tau_1)c^\dagger_{i\sigma}(\tau_2) >^{(0)} c_{0\sigma}(\tau_2) \tag{2.14}$$

As for the hopping amplitude, we always take the amplitude of hopping into and out of the cavity site to be equal, $t_{0i} = t_{i0}$, it is same for "j". So one finds that Eq.(2.13) and Eq.(2.14) are same. One can prove that the first term is the same as the second term in the bracket.

$$\begin{aligned}
&\frac{1}{2!}\int_0^\beta d\tau_1\int_0^\beta d\tau_2\big\langle T_\tau \Delta S(\tau_1)\Delta S(\tau_2)\big\rangle^{(0)} \\
=\;& \int_0^\beta d\tau_1\int_0^\beta d\tau_2\sum_\sigma c^\dagger_{0\sigma}(\tau_1)\sum_{ij}t_{i0}t_{0j} < T_\tau c_{i\sigma}(\tau_1)c^\dagger_{j\sigma}(\tau_2) >^{(0)} c_{0\sigma}(\tau_2) \\
=\;& \int_0^\beta d\tau_1\int_0^\beta d\tau_2\sum_\sigma c^\dagger_{0\sigma}(\tau_1)\sum_{ij}t_{i0}t_{0j}G^{(0)}_{ij}(\tau_1-\tau_2)c_{0\sigma}(\tau_2)
\end{aligned} \tag{2.15}$$

Similarly, all the higher order terms can be written down in a similar way. Then the effective action can be expressed as:

$$S_{eff} = \sum_{n=1}^{\infty} \sum_{i_1 \cdots j_n} \int \eta^{\dagger}_{i_1}(\tau_{i_1}) \cdots \eta^{\dagger}_{i_n}(\tau_{i_n}) \eta_{j_1}(\tau_{j_1}) \cdots \eta_{j_n}(\tau_{j_n}) G^{(0)}_{i_1 \cdots j_n}(\tau_{i_1} \cdots \tau_{i_n}, t_{j_1} \cdots \tau_{j_n}) + S_0 \tag{2.16}$$

where, $\eta_i = t_{i0} c_{0\sigma}$ plays the role of a source coupled to $c^{\dagger}_{i\sigma}$.

At the limit of $d \to \infty$, this equation can be significantly simplified. Note that in order to keep the hopping amplitude well defined in this limit, t_{ij} should be scaled as $1/\sqrt{d}^{|i-j|}$. Then only can the first term survive in this case. This can be understood from the analysis of the first few terms. In the case that only the nearest neighbor hopping is considered, the pre-factor gives t^2 and $G^{(0)}_{ij}$ also gives a factor of t^2 in the first expansion term, so the total factor is $t^4 = 1/d^2$. But the d-dimensional summation of i and j gives d^2, so the first term is of the order of 1. The second-order term involves a connected four-point function $G^{(0)}_{ijkl}$ which falls off as $(1/\sqrt{d})^{|i-j|}(1/\sqrt{d})^{|i-k|}(1/\sqrt{d})^{|i-l|}$. When i, j, k, l are all different, it gives at least $1/d^3$ in the condition of the nearest neighbor hopping. And the four summations give another factor of d^4. The four t scale as $1/d^2$. So the total factor of the second-order term is $1/d$ which is zero in the limit of $d \to \infty$. Similarly, the terms where $i = j \neq k \neq l$ contains three summations, which give d^3, four factors of t gives $1/d^2$, and a factor of $1/d^2$ is given by $G^{(0)}$. Then this term scales again as $1/d$. In the limit of $d \to \infty$, the effective action therefore reduces to

$$\begin{aligned} S_{eff} &= -\int_0^{\beta} d\tau \int_0^{\beta} d\tau' \sum_{\sigma} c^{\dagger}_{0\sigma}(\tau) \mathcal{G}_0^{-1}(\tau - \tau') c_{0\sigma}(\tau') + U \int_0^{\beta} d\tau n_{0\uparrow}(\tau) n_{0\downarrow}(\tau) \\ &= S_0 + \int_0^{\beta} d\tau_1 \int_0^{\beta} d\tau_2 \sum_{\sigma} c^{\dagger}_{0\sigma}(\tau_1) \sum_{ij} t_{i0} t_{0j} G^{(0)}_{ij}(\tau_1 - \tau_2) c_{0\sigma}(\tau_2) \end{aligned} \tag{2.17}$$

it yields that

$$\mathcal{G}_0^{-1}(\tau_1 - \tau_2) = -(\frac{\partial}{\partial \tau_1} - \mu)\delta_{\tau_1, \tau_2} - \sum_{ij} t_{i0} t_{0j} G^{(0)}_{ij}(\tau_1 - \tau_2) \tag{2.18}$$

In the momentum space, it can be rewritten as

$$\mathcal{G}_0^{-1}(i\omega_n) = i\omega_n + \mu - \sum_{ij} t_{i0} t_{0j} G^{(0)}_{ij}(i\omega_n) \tag{2.19}$$

The only assumption we have introduced is the infinite dimension limit under which DMFT becomes an exact theory. From a diagrammatical point of view, in the limit $D \to \infty$ the skeleton expansion for Σ collapses onto the local diagram. As a result the single particle self energy in infinite dimension is purely local in real space $\Sigma_{ij}(i\omega_n) = \Sigma(i\omega_n)\delta_{ij}$. The higher order expansion terms represent the vertex correction which has been omitted in DMFT, which means the two particles coming into a vertex (for example with momentum $\mathbf{k_1}$ and $\mathbf{k_3}$) are exactly same as the

ones going out (for example with momentum $\mathbf{k_2}$ and $\mathbf{k_4}$). The Laue-function then reduces to

$$\Delta(\mathbf{k_1}, \mathbf{k_2}, \mathbf{k_3}, \mathbf{k_4}) = \sum_r e^{i(\mathbf{k_1}-\mathbf{k_2}+\mathbf{k_3}-\mathbf{k_4})\cdot r} = N\delta_{\mathbf{k_1}-\mathbf{k_2}+\mathbf{k_3}+\mathbf{K_4}} \tag{2.20}$$

Thus the momentum conservation at the internal vertices of irreducible diagrams can be disregarded in infinite dimensions. DMFT assumes the same Laue-function even in the finite dimension, resulting in the momentum independent self-energy function and one particle Green's function.

$$G(i\omega_n) = \frac{1}{N}\sum_{\mathbf{k}} G(\mathbf{k}, i\omega), \qquad \Sigma(i\omega_n) = \frac{1}{N}\sum_{\mathbf{k}} \Sigma(\mathbf{k}, i\omega) \tag{2.21}$$

Thus the DMFT contains only local correlations and neglects the contribution for the non-local fluctuation.

2.2 Implementations of DMFT

The simplification introduced by the DMFT is mapping a many-body interacting problem to a single impurity problem, the locality of the self-energy function reduces the full one particle Green's function

$$G(\mathbf{k}, i\omega_n) = \frac{1}{i\omega_n + \mu - \epsilon(\mathbf{k}) - \Sigma(\mathbf{k}, i\omega_n)} \tag{2.22}$$

to the one which only depends on frequency

$$G(i\omega_n) = \frac{1}{N}\sum_{\mathbf{k}} \frac{1}{i\omega_n + \epsilon(\mathbf{k}) - \Sigma(i\omega_n)} = \frac{1}{i\omega_n + \mu - \epsilon_0 - \Delta(i\omega_n) - \Sigma(i\omega_n)} \tag{2.23}$$

Here, $\epsilon_0 = 1/N\sum_{\mathbf{k}}\epsilon(\mathbf{k})$ and $\Delta(i\omega_n)$ describes the hybridization with the remaining part of the lattice.

In DMFT the lattice geometry comes into calculation through the dispersion relation $\epsilon_{\mathbf{k}}$. The momentum sum is performed in the corresponding first Brillouin zone (**B.Z.**). Normally, we replace the momentum sum with the integral over energy ϵ if we know the density of state $D(\epsilon)$. Fig. 2.2 shows the density of state for tight-binding model at $d = 2$ square lattice, $d = 3$ cubic lattice, and also $d = 4$ and $d = 5$ lattice which only have hopping between the nearest neighboring sites. At $d = 2$ case, the density of state shows the Van Hove singularity at $\epsilon = 0$, with the increasing of dimensionality, $D(\epsilon)$ tends to be smooth and when $d \to \infty$, it becomes semicircular.

Since the self-energy function is momentum independent, this problem can be viewed as an interacting impurity coupled to a dynamic bath $\Delta(i\omega_n)$, which has been extensively studied in the so-called Single Impurity Anderson model (SIAM).

$$H^{SIAM} = \sum_{\sigma}(\epsilon_0 - \mu)f^{\dagger}_{\sigma}f_{\sigma} + Un^f_{\uparrow}n^f_{\downarrow} + \frac{1}{\sqrt{N}}\sum_{\mathbf{k},\sigma}(V_{\mathbf{k}}f^{\dagger}_{\sigma}a_{\mathbf{k},\sigma} + V^*_{\mathbf{k}}a^{\dagger}_{\mathbf{k},\sigma}f_{\sigma}) + \sum_{\mathbf{k},\sigma}\epsilon_{\mathbf{k}}a^{\dagger}_{\mathbf{k}\sigma}a_{\mathbf{k}} \tag{2.24}$$

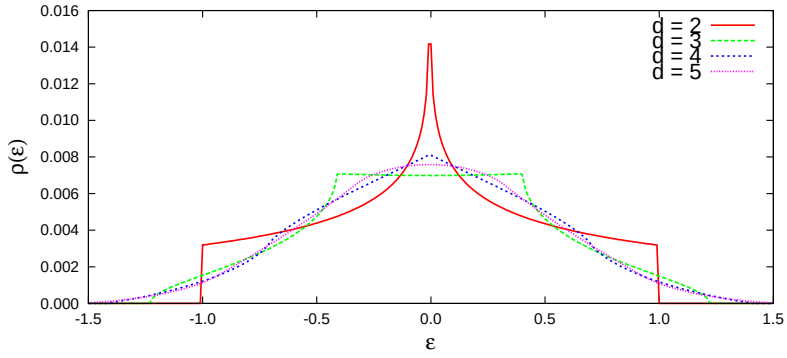

Figure 2.2: *The density of state for various lattice geometry (see context). To know bare density of state $D(\epsilon)$ for the lattice studied is always the first step one needs to do in DMFT.*

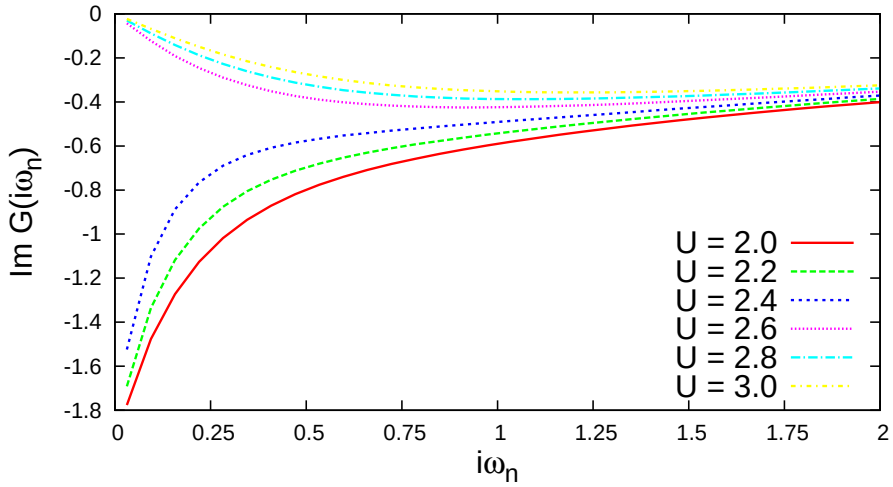

Figure 2.3: *Imaginary part of the local Green's function for $\beta = 100$ and interaction U from 2.0 to 3.0, with bandwith $W = 2.0$.*

The first two terms belong to the impurity site, the last term is the dispersion relation for the bath which is described by $\Delta(i\omega_n)$ as a conduction band. The third term represents the hybridization between the impurity site and the conduction band. Solve this Hamiltonian with the equation of motion, the impurity Green's function has the following form

$$G^f(i\omega_n) = \frac{1}{i\omega_n + \mu - \epsilon_0 - \Delta(i\omega_n) - \Sigma(i\omega_n)} \text{ with } \Delta(i\omega_n) = \frac{1}{N}\sum_{\mathbf{k}} \frac{|V_{\mathbf{k}}^2|}{i\omega_n - \epsilon_{\mathbf{k}}} \tag{2.25}$$

which is identical to the local Green's function obtained in DMFT. It can also show that the skeleton diagrams from SIAM is formally identical to that of DMFT [Jarrell (1992)]. Thus the lattice self energy can be obtained by solving the impurity model

where the bare Green's function is replaced by the inverse of Weiss field. Normally, the DMFT equation can be solved in the following way

1. Start with a guess for the self-energy function $\Sigma(i\omega_n)$ which is usually taken as zero.
2. Determine the Green's function from Eq. (2.23) by performing the momentum summation[1].
3. Construct the Weiss field from the Dyson equation $\mathcal{G}^{-1} = G^{-1} + \Sigma$.
4. By using some kind of impurity solver to calculate the self-energy function from the dressed Green's function.
5. Repeat the above procedure until the desired convergence is reached.

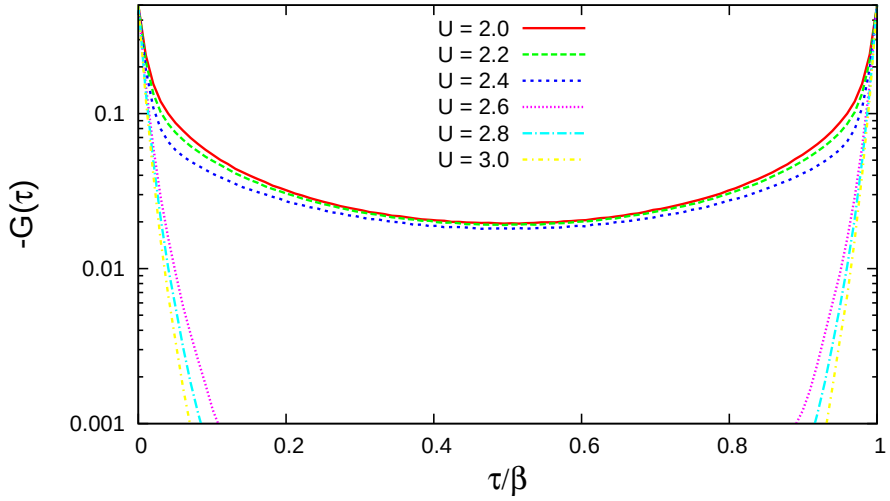

Figure 2.4: *Imaginary time Green's function for $\beta = 100$ and various interaction U from 2.0 to 3.0. $G(\beta/2)$ drops from a finite value to zero with the increasing of interaction.*

Note, here $D(\epsilon)$ is only the density of state for the non-interacting lattice which is described by the tight-binding model. The non-zero values at $\epsilon = 0$ indicates the metallic behavior. When the Coulomb interaction is turned on, some interacting systems gradually change from metal to insulator. With respect to the total density, the peak at $\epsilon = 0$ gradually smears out, finally a gap opens. The Mott-Hubbard transition can be observed by calculating the dressed impurity Green's function. Fig. 2.3 shows the imaginary part of the one particle Green's function $G(i\omega_n)$ for $\beta = 64$, and U from 2.0 to 3.0. Here the semicircular density of state is used with band width $W = 2$. From this diagram, we can see with the increase of interaction strength,

[1]Normally, if we know the density of state of the bath, we can replace this sum with integral, see context.

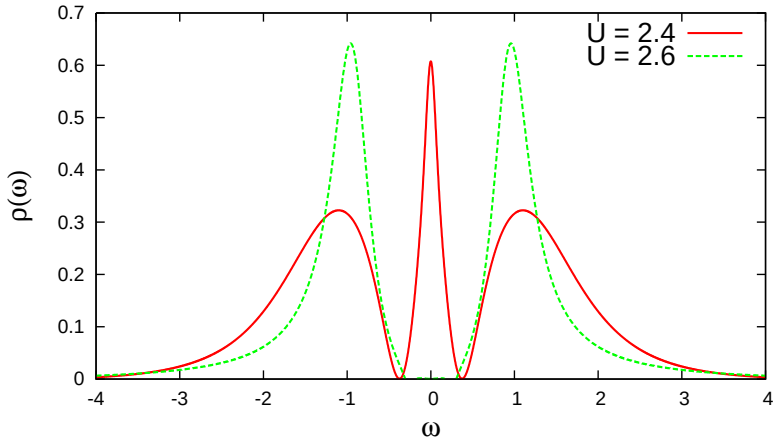

Figure 2.5: *Local density of state for $\beta = 100$, $U = 2.4$ and 2.6. Here the same band width $W = 2$ is used. With the increasing of interaction, the peak at $\omega = 0$ disappears and the Mott gap forms.*

the lowest frequency point of the imaginary part of the dressed Green's function becomes smaller and jumps to a very small value at U around 2.4 - 2.6. This clear change of $Im[G(i\omega_1)]$ indicates the system gradually changes from metallic phase (corresponds to curves of $U = 2, 2.2, 2, 4$) to insulating phase (corresponding to curve of $U = 2.6, 2.8, 3.0$) and the critical U_c is between $U = 2.4$ - 2.6. Similar behavior can be seen from the imaginary time Green's function $G(\tau)$. In Fig. 2.4, the same parameter regime was studied. To observe the Metal-Insulator transition in $G(\tau)$, one can compare the value for $\tau = \beta/2$. For interaction $U = 2.0, 2.2, 2.4$, $G(\beta/2)$ has a small but still non-zero value. Further increasing the interaction, $G(\beta/2)$ rapidly dropped to zero which shows the transition.

The clearest way to show the Metal-Insulator transition is to calculate the total density of state, which is related to the imaginary part of the one particle dressed Green's function in real frequency space, see Eq. (1.18). Since we used the Quantum Monte Carlo method as impurity solver, which works in the imaginary frequency or imaginary time space. To calculate the real frequency Green's function, one has to perform the analytical continuation to change G from imaginary frequency to real frequency. Here, we used the simple Padé approximation method. The Metal-Insulator transition is clearly seen from the disappearance of the coherence peak at Fermi surface.

2.3 Quantum Cluster Methods

The exact formulation of DMFT at infinite dimension ensures the validity of this method, when it is applied to the system where the spatial fluctuation is not strong. Strongly correlated electron systems are often characterized by short range dynamical fluctuations. Consequently, local approximations like DMFT successfully describe many of the qualitative properties. However, in some systems (especially in

the low-dimensional systems), spatial correlations become increasingly important and are thought to be responsible for e.g. non-Fermi-liquid behavior and d-wave superconductivities.

Explicitly including the non-local fluctuations to DMFT method has been studied extensively [Maier *et al.* (2005)], such as Cellular Dynamical Mean Field Theory (C-DMFT) [Kotliar *et al.* (2001)], Dynamical Cluster Approximation (DCA) [Hettler *et al.* (2000)], Fictive Impurity Model [Okamoto *et al.* (2003)], Variational Cluster Approximation which is based on the self-energy functional theory [Potthoff (2003)], etc. In this chapter we will mainly discuss two methods, C-DMFT and DCA. These two methods are formulated in different spaces. We will start with a general extension of single site DMFT. By introducing a cluster in real and momentum space respectively, we then go into the details of these two methods. The C-DMFT and DCA implementations of in a square lattice are then given as example.

2.3.1 General formulism

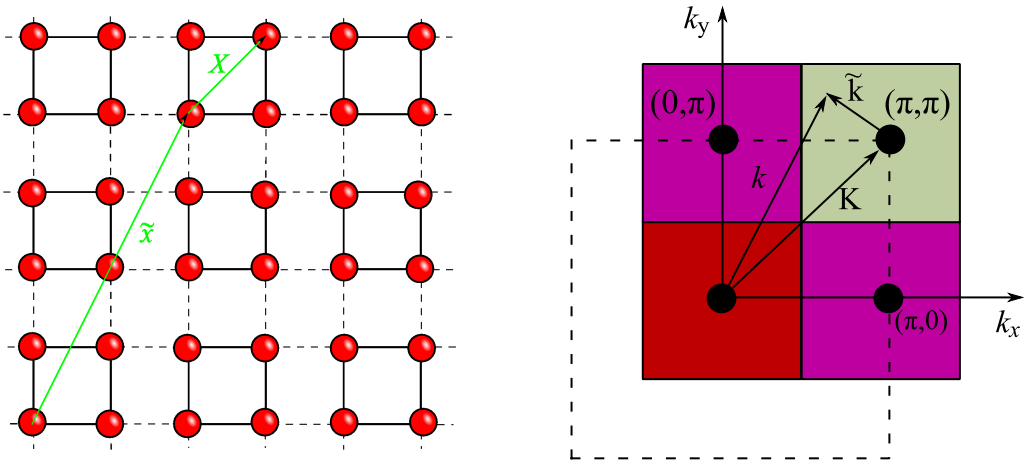

Figure 2.6: *$L_C \times L_C$ cluster embedded in the lattice forms a surperlattice. It's reduced Brillouin Zone is $L_C \times L_C$ smaller of the first B.Z for the original lattice. Here we took $L_C = 2$ as example. The position of Each site in the lattice can be identically expressed as $x = \tilde{x} + X$, correspondingly the wave vector is $k = K + \tilde{k}$.*

In the derivation of single site DMFT equations, we employed the cavity method. By separating impurity degrees of freedom from the remaining degrees of freedoms which we named as bath, the total action can be written into three parts, where the non-interacting bath degrees of freedom can be integrated out precisely. In the end, the effective action is only a function of the impurity degree of freedom which is local. Now, we apply the same idea to a cluster embedded in lattice. Here the impurity is replaced by a small cluster, in which way we can partially include the non-local correlations. But here we will not formulate C-DMFT and DCA via action, we will perform the locator expansion instead. We will see this method is equivalent to the cavity construction. We expand the one particle Green's function over the inter-cluster coupling by separating the cluster degrees of freedom from those of the remaining.

In this section, we derive formalisms of dynamical cluster approximation and cellular dynamical mean-field theory based on the review work of T. Maier [Maier *et al.* (2005)]. As discussed in the introduction, after expanding a single impurity to a cluster we want to separate the degrees of freedom within the cluster from the remaining degrees of freedom. Thus we divide a D-dimensional lattice of N sites into a set of finite-size clusters, each have N_c sites of linear size L_c such that $N_c = L_c^D$. Here we take a two-dimensional lattice with $L_c = 2$ as example. There are $N_c = L_c \times L_c = 4$ sites in each cluster. Note that it is not necessary to ask for the same L_c at every dimension. L_c is taken freely in each dimension, $N_c = \prod_{i=1}^{D} L_c^i$. Although each L_c^i is arbitrarily selected, a better choice of cluster should have the same symmetry of the lattice.

The first Brillouin zone will be divided into a corresponding set of reduced zones which are called cells. From now on, we use the coordinate $\tilde{\mathbf{x}}$ to label the origin of the clusters and $\mathbf{X}$ to label the N_c sites within a cluster, so that the lattice site can be identically labeled as $\mathbf{x} = \mathbf{X} + \tilde{\mathbf{x}}$. $\tilde{\mathbf{k}}$ is the wave vector corresponding to the super-lattice points $\tilde{\mathbf{x}}$. And the wave vector corresponding to the sites $\mathbf{X}$ within a cluster is labeled $\mathbf{K}$, so in the full Brillouin zone, the wave vectors are given by $\mathbf{k} = \mathbf{K} + \tilde{\mathbf{k}}$.

With these notations, one can easily expand the definition of Fourier transforms of a given function $f(\mathbf{x})$ as

$$f(\mathbf{X}, \tilde{\mathbf{x}}) = \frac{N_c}{N} \sum_{\tilde{\mathbf{k}}} e^{i(\mathbf{K}+\tilde{\mathbf{k}})\cdot\tilde{\mathbf{x}}} f(\mathbf{X}, \tilde{\mathbf{k}}) = \frac{N_c}{N} \sum_{\tilde{\mathbf{k}}} e^{i\tilde{\mathbf{k}}\cdot\tilde{\mathbf{x}}} f(\mathbf{X}, \tilde{\mathbf{k}}) \tag{2.26}$$

$$f(\mathbf{X}, \tilde{\mathbf{k}}) = \sum_{\tilde{\mathbf{x}}} e^{-i(\mathbf{K}+\tilde{\mathbf{k}})\cdot\tilde{\mathbf{x}}} f(\mathbf{X}, \tilde{\mathbf{x}}) = \sum_{\tilde{\mathbf{x}}} e^{-i\tilde{\mathbf{k}}\cdot\tilde{\mathbf{x}}} f(\mathbf{X}, \tilde{\mathbf{x}}) \tag{2.27}$$

$$f(\mathbf{X}, \tilde{\mathbf{k}}) = \frac{1}{N_c} \sum_{\mathbf{K}} e^{i(\mathbf{K}+\tilde{\mathbf{k}})\cdot\mathbf{X}} f(\mathbf{X}, \tilde{\mathbf{k}}) \tag{2.28}$$

$$f(\mathbf{K}, \tilde{\mathbf{k}}) = \sum_{\mathbf{X}} e^{-i(\mathbf{K}+\tilde{\mathbf{k}})\cdot\mathbf{X}} f(\mathbf{X}, \tilde{\mathbf{k}}) \tag{2.29}$$

In the first two equations, the identity $e^{i\mathbf{K}\cdot\tilde{\mathbf{x}}} = 1$ was used since $\mathbf{K}_i = i(2\pi/L_c)$.

After the separation of cluster, correspondingly, the hopping amplitude t and the self-energy Σ are also split into two parts, which are called intra-cluster and inter-cluster parts.

$$\mathbf{t}(\mathbf{x_i} - \mathbf{x_j}) = \mathbf{t}_c \delta_{\tilde{\mathbf{x}}_\mathbf{i}, \tilde{\mathbf{x}}_\mathbf{j}} + \delta\mathbf{t}(\tilde{\mathbf{x}}_\mathbf{i} - \tilde{\mathbf{x}}_\mathbf{j}) \tag{2.30}$$

$$\mathbf{\Sigma}(\mathbf{x_i} - \mathbf{x_j}, z) = \mathbf{\Sigma}_c \delta_{\tilde{\mathbf{x}}_\mathbf{i}, \tilde{\mathbf{x}}_\mathbf{j}} + \delta\mathbf{\Sigma}(\tilde{\mathbf{x}}_\mathbf{i} - \tilde{\mathbf{x}}_\mathbf{j}, z) \tag{2.31}$$

$\mathbf{t}_c = \mathbf{t}(\tilde{\mathbf{x}} = 0)$ and $\mathbf{\Sigma}_c(\tilde{\mathbf{x}} = 0, z)$ are the intra-cluster hopping and self-energy, $\delta\mathbf{t}(\tilde{\mathbf{x}})$ and $\delta\mathbf{\Sigma}(\tilde{\mathbf{x}}, z)$ are the inter-cluster parts of hopping and self-energy. Note it is not necessary to ask for $\mathbf{t_c} = t$. Later on it will become clear that C-DMFT and DCA are different in the choice of $\mathbf{t_c}$.

Analogously to the cavity construction where the coupling between the impurity site and the remainder of the lattice is expanded, we take an expansion in $\delta\mathbf{t}$ and

$\delta\mathbf{\Sigma}$ around the cluster limit to rewrite the Green's function of super-lattice as

$$\begin{aligned} & \mathbf{G}^{-1}(\tilde{\mathbf{x}_\mathbf{i}} - \tilde{\mathbf{x}_\mathbf{j}}, z) \\ = \; & \mathbf{G}_0^{-1}(\tilde{\mathbf{x}_\mathbf{i}} - \tilde{\mathbf{x}_\mathbf{j}}) - \mathbf{\Sigma}(\tilde{\mathbf{x}_\mathbf{i}} - \tilde{\mathbf{x}_\mathbf{j}}, z) \\ = \; & z - [\mathbf{t}(\tilde{\mathbf{x}_\mathbf{i}} - \tilde{\mathbf{x}_\mathbf{j}}) - \mu] - \mathbf{\Sigma}(\tilde{\mathbf{x}_\mathbf{i}} - \tilde{\mathbf{x}_\mathbf{j}}, z) \\ = \; & [z + \mu - \mathbf{t_c} - \mathbf{\Sigma_c}(z)] - [\delta\mathbf{t}(\tilde{\mathbf{x}_\mathbf{i}} - \tilde{\mathbf{x}_\mathbf{j}}) + \delta\mathbf{\Sigma}(\tilde{\mathbf{x}_\mathbf{i}} - \tilde{\mathbf{x}_\mathbf{j}}, z)] \\ = \; & \mathbf{g}^{-1}(z) - [\delta\mathbf{t}(\tilde{\mathbf{x}_\mathbf{i}} - \tilde{\mathbf{x}_\mathbf{j}}) + \delta\mathbf{\Sigma}(\tilde{\mathbf{x}_\mathbf{i}} - \tilde{\mathbf{x}_\mathbf{j}}, z)] \end{aligned} \tag{2.32}$$

where $\mathbf{g}(z)$ is a $N_c \times N_c$ matrix, which is the dressed Green's function of the isolated cluster.

$$\mathbf{g}(z) = [(z+\mu)\hat{I} - \mathbf{t}_c - \mathbf{\Sigma}_c(z)]^{-1} \tag{2.33}$$

In the standard notation, the full Green's function is given as

$$\mathbf{G}(\tilde{\mathbf{x}_\mathbf{i}} - \tilde{\mathbf{x}_\mathbf{j}}, z) = \mathbf{g}(z)\delta_{\tilde{\mathbf{x}_\mathbf{i}},\tilde{\mathbf{x}_\mathbf{j}}} + \mathbf{g}(z)\sum_l \left[\delta\mathbf{t}(\tilde{\mathbf{x}_\mathbf{i}} - \tilde{\mathbf{x}_\mathbf{l}}) + \delta\mathbf{\Sigma}(\tilde{\mathbf{x}_\mathbf{i}} - \tilde{\mathbf{x}_\mathbf{l}}, z)\right]\mathbf{G}(\tilde{\mathbf{x}_\mathbf{l}} - \tilde{\mathbf{x}_\mathbf{j}}, z) \tag{2.34}$$

This equation contains all the expansion order around the cluster limit. The influence of the correlation beyond the cluster scope becomes the correction to the cluster dressed Green's function $g(z)$. The corrections are in two parts, δt and $\delta\Sigma$. $\delta\Sigma$ contains the vertex correction.

In momentum space the above equation can be written into a simpler form,

$$\mathbf{G}(\tilde{\mathbf{k}}, z) = \mathbf{g}(z) + \mathbf{g}(z)[\delta\mathbf{t}(\tilde{\mathbf{k}}) + \delta\tilde{\mathbf{\Sigma}}(\tilde{\mathbf{k}}, z)]\mathbf{G}(\tilde{\mathbf{k}}, z) \tag{2.35}$$

This is a general formula for quantum cluster theory. Though every method focus on different physical consideration, they have a common approximation. They all truncate the self-energy to the cluster by neglecting $\delta\mathbf{\Sigma}$ to arrive at:

$$\mathbf{G}(\tilde{\mathbf{k}}, z) = \mathbf{g}(z) + \mathbf{g}(z)\delta\mathbf{t}(\tilde{\mathbf{k}})\mathbf{G}(\tilde{\mathbf{k}}, z) = [\mathbf{g}^{-1}(z) - \delta\mathbf{t}(\tilde{\mathbf{k}})]^{-1} \tag{2.36}$$

Here it is very clear that various cluster approximations fully consider the correlation within the cluster (Σ_c), while taking the spatial fluctuation beyond the cluster in one-particle mean field approximation[2]. A further improvement to the current cluster DMFT methods starts from the reconsideration of $\delta\Sigma$. If we average $\mathbf{G}(z)$ over $\tilde{\mathbf{k}}$, then the Green's function will restrict to the cluster.

$$\bar{\mathbf{G}}(z) = \frac{N_c}{N}\sum_{\tilde{\mathbf{k}}} \mathbf{G}(\tilde{\mathbf{k}}, z) \tag{2.37}$$

Compared to Eq. (2.28), the coarse graining is equivalent to omit the momentum conservation law for the super-lattice. The sequence of the coarse graining is that it smears out the spatial fluctuation in the super-lattice.

[2]Since the vortex correction from the outside of cluster has been omitted ($\delta\Sigma$), only the one particle correction has been taken into account (δt)

2.3.2 Cellular DMFT and DCA

In this section, we will go into the details of the Cellular DMFT and DCA. Here, both of them will be formulated in real space. The most popular formulation of DCA is in the reciprocal space. In order to address the difference between C-DMFT and DCA, we prefer to use the real space formulation. The reciprocal space representation of DCA will be easily obtained afterwards.

Starting with Eq. (2.36), the basic difference in C-DMFT and DCA as we discussed in the above section is the choice of $t(x_i - x_j)$. Both the inter-cluster hopping and intra-cluster hopping are different in these two methods. In the lattice, the full dispersion relation can be calculated from the Fourier-Transform of t as $\epsilon(k) = \sum_{i,j} e^{-ik\cdot(x_i - x_j)} t_{i,j}$. If we only consider the nearest neighbor hopping in the Hubbard model, it is $-2t\cos(k)$. After we divided the lattice into a collection of clusters, the hopping term becomes of a combination of the inter-cluster and intra-cluster parts. This results in the violation of the translational invariance in real space. The inter and intra cluster hopping amplitudes are different. From Eq. (2.28)

$$\begin{aligned}
[t(\tilde{k})]_{\mathbf{X}_i\mathbf{X}_j} &= \frac{1}{N_c}\sum_{\mathbf{K}} e^{i(\mathbf{K}+\tilde{\mathbf{k}})\cdot(\mathbf{X}_i-\mathbf{X}_j)}\epsilon(k) = \frac{-t}{N_c}\sum_{\mathbf{K}} e^{i(\mathbf{K}+\tilde{\mathbf{k}})\cdot(\mathbf{X}_i-\mathbf{X}_j)} e^{-i(\mathbf{K}+\tilde{\mathbf{k}})\cdot(\mathbf{x}_i-\mathbf{x}_j)} \\
&= -\frac{t}{N_c}\sum_{\mathbf{K}} e^{-i(\mathbf{K}+\tilde{\mathbf{k}})\cdot(\tilde{\mathbf{x}}_i-\tilde{\mathbf{x}}_j)} = -te^{-i\tilde{\mathbf{k}}\cdot(\tilde{\mathbf{x}}_i-\tilde{\mathbf{x}}_j)} \qquad (2.38)
\end{aligned}$$

This is the dispersion relation used in C-DMFT. It has different values for the inter and the intra-cluster hopping. If X_i and X_j are in the same cluster, $t(\tilde{k}) = -t$ which is same as the hopping in the original lattice. If X_i and X_j belong to different clusters, the pre-factor $e^{i\tilde{\mathbf{k}}\cdot(\tilde{\mathbf{x}}_i-\tilde{\mathbf{x}}_j)}$ is not zero, which means the inter-cluster hopping is mediated by the super-lattice wave vector $\tilde{\mathbf{k}}$.

The C-DMFT cluster problem can be solved self-consistently as shown in Fig. 2.7

1. Start from an initial cluster self-energy Σ_c which is normally taken as zero.
2. From the dispersion relation for C-DMFT, calculate the cluster Green's function $\bar{G}(z)$ which is in matrix form[3].
3. Construct the Weiss field $\bar{\mathcal{G}}^{-1}$ from the cluster Green's function $\bar{G}$ and self-energy function $\bar{\Sigma}$.
4. Determine the dressed cluster Green's function from a suitable cluster solver.
5. The new self-energy function is given by the Dyson equation.
6. The above iteration will go on until convergence is reached.

In C-DMFT the violation of the translational invariance can be restored in two possible ways. By introducing periodization for either cluster self-energy, which can

[3]Note in this step, matrix inversion is needed since $t(\tilde{\mathbf{k}})$, $\bar{\Sigma}$ are matrices

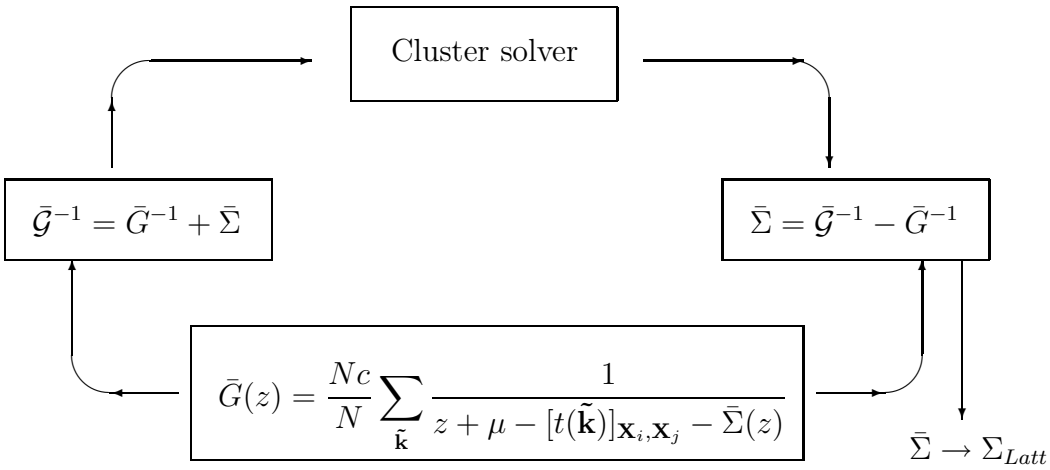

Figure 2.7: *Sketch of C-DMFT loop. Note the lattice self-energy is calculated when the DMFT loop reaches the convergence.*

generate the spurious mid-gap states in the Mott insulator [Kyung *et al.* (2006)], or for the irreducible cumulant [Stanescu and Kotliar (2006)], one can make the lattice Green's function to be periodic. More details and discussion can be found in corresponding references.

Although the only approximation introduced here is the division of the lattice, this little approximation breaks the translational invariance of the original lattice. DCA trys to restore the translational invariance even inside the cluster. The violation is caused by the factor $e^{i\tilde{\mathbf{k}}\cdot(\mathbf{X}_i-\mathbf{X}_j)}$, thus in DCA this term is explicitly omitted.

$$[t^{DCA}(\tilde{\mathbf{k}})]_{\mathbf{X}_i\mathbf{X}_j} = e^{-i\tilde{\mathbf{k}}\cdot(\mathbf{X}_i-\mathbf{X}_j)}[t^{C-DMFT}(\tilde{\mathbf{k}})]_{\mathbf{X}_i\mathbf{X}_j} = -te^{-i\tilde{\mathbf{k}}\cdot(\mathbf{x}_i-\mathbf{x}_j)} \tag{2.39}$$

where t^{C-DMFT} is given in Eq. (2.38). DCA dispersion relation is cyclic both inside and outside cluster. Basically we can say in C-DMFT the gauge is chosen such that phase factors appear only in matrix elements involving different clusters, which breaks the symmetry of the original lattice. DCA distributes this phase factor to all the matrix elements. In both C-DMFT and DCA, the eigenvalues of $H(\tilde{\mathbf{k}})$ are identical to the eigenvalues of the non-interacting part of H, which can be used as internal check of C-DMFT and DCA equations.

The DCA equations can be solved in a similar way like the C-DMFT loop. The execution of DCA loop depends on the specific cluster solver used[4]. In Fig. 2.7, one only needs to replace $t(\tilde{\mathbf{k}})$ with t^{DCA}. Every property is still in matrix form, one has to perform matrix inversion for each specific $\tilde{\mathbf{k}}$. This is equivalent to the momentum space implementation since t^{DCA} can be diagonalized by the Fourier transform. One can also use the diagonal form of t^{DCA} with the advantage that the full matrix inversion is replaced by the inversion of the diagonal elements. Once the diagonal form of $\bar{\mathcal{G}}(z)$ is obtained, one has to Fourier transform it back to real

[4]While most of the DCA implementation is in momentum space, here we use real space notation to show the comparison with C-DMFT, it is easy to switch from one to the other, once one has implemented one of them

space in order to calculate the dressed Green's function from the cluster solver. In DCA, the self-energy function and the dressed Green's function are in a diagonal form, therefore one does not need to re-periodize them.

Here we take the 2×2 cluster on a square lattice as an example to show the difference of C-DMFT and DCA. Furthermore, here we consider the more interesting full frustration case. The real space cluster geometry is given in Fig. 2.8 with the same Reduced Brillouin Zone (R.B.Z) as shown in Fig. 2.6. The hopping matrices

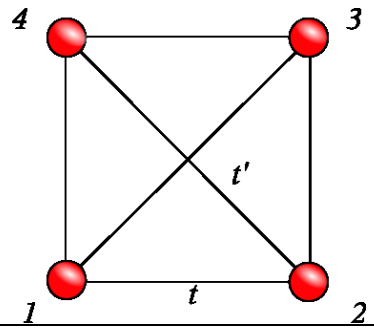

Figure 2.8: *2×2 cluster in a frustrated square lattice. Here we take $t' = t$.*

in real space for C-DMFT and DCA are given as below

$$t^{C-DMFT} = \begin{pmatrix} 0 & 1+t_x & 1+t_x+t_y+t_xt_y & 1+t_y \\ 1+t_x^* & 0 & 1+t_y & 1+t_x^*+t_y+t_x^*t_y \\ 1+t_x^*+t_y^*+t_x^*t_y^* & 1+t_y^* & 0 & 1+t_x^* \\ 1+t_y^* & 1+t_x+t_y^*+t_xt_y^* & 1+t_x & 0 \end{pmatrix} \tag{2.40}$$

where $t_x = e^{2i\tilde{\mathbf{k}}_\mathbf{x}}$, $t_y = e^{2i\tilde{\mathbf{k}}_\mathbf{y}}$ and every element is in the unit of $-t$. In DCA it is

$$t^{DCA} = \begin{pmatrix} 0 & 2\cos\tilde{\mathbf{k}}_x & 4\cos\tilde{\mathbf{k}}_x\cos\tilde{\mathbf{k}}_y & 2\cos\tilde{\mathbf{k}}_y \\ 2\cos\tilde{\mathbf{k}}_x & 0 & 2\cos\tilde{\mathbf{k}}_y & 4\cos\tilde{\mathbf{k}}_x\cos\tilde{\mathbf{k}}_y \\ 4\cos\tilde{\mathbf{k}}_x\cos\tilde{\mathbf{k}}_y & 2\cos\tilde{\mathbf{k}}_y & 0 & 2\cos\tilde{\mathbf{k}}_x \\ 2\cos\tilde{\mathbf{k}}_y & 4\cos\tilde{\mathbf{k}}_x\cos\tilde{\mathbf{k}}_y & 2\cos\tilde{\mathbf{k}}_x & 0 \end{pmatrix} \tag{2.41}$$

This equation can be diagonalized easily by the transformation

$$U = \frac{1}{2}\begin{pmatrix} 1 & 1 & 1 & 1 \\ -1 & -1 & 1 & 1 \\ -1 & 1 & 1 & -1 \\ -1 & 1 & -1 & 1 \end{pmatrix} \tag{2.42}$$

as $Diag[Ut^{DCA}U^\dagger] = [\epsilon(\tilde{\mathbf{k}}_x, \tilde{\mathbf{k}}_y), \epsilon(\tilde{\mathbf{k}}_x, \tilde{\mathbf{k}}_y + \pi), \epsilon(\tilde{\mathbf{k}}_x + \pi, \tilde{\mathbf{k}}_y), \epsilon(\tilde{\mathbf{k}}_x + \pi, \tilde{\mathbf{k}}_y + \pi)]$. $\tilde{\mathbf{k}}_x$ and $\tilde{\mathbf{k}}_y$ are in the Reduced Brillouin Zone $[-\pi/2, \pi/2]$ and $\epsilon(\tilde{\mathbf{k}}_x, \tilde{\mathbf{k}}_y) = -2t(\cos\tilde{\mathbf{k}}_x + \cos\tilde{\mathbf{k}}_y + 2\cos\tilde{\mathbf{k}}_x\cos\tilde{\mathbf{k}}_y)$. The diagonal form of the hopping matrix is the commonly used form of DCA. The original first Brillouin Zone is divided into 2×2 parts, with $\mathbf{K}_c = (0,0), (0,\pi), (\pi,0), (\pi,\pi)$ as shown in Fig. 2.6. In the end the real-space and momentum-space representations of DCA equations are equivalent and relate with each other through the transformation matrix U.

The difference of C-DMFT and DCA equations are clearly shown in the expression of t^{CDMFT} and t^{DCA}. The translational invariance is violated in t^{CDMFT} while t^{DCA} restores it. The real space formulation of DCA equations ensures that one can switch from one method to the other easily once the codes for one of them are avaliable.

Fig. 2.9 shows the Fermi surface and density of states of the Hubbard model on the 2×2 cluster shown in Fig. 2.8 for different ratio of t'/t. Here, we only showed the non-interacting density of state and Fermi surface from the DCA dispersion relation, the dressed Green's function and full density of states can be calculated straightforwardly in the cluster solver. The non-zero values of t'/t destroyed the perfect nested Fermi-surface of 2D square lattice. Later on we will see that t' term introduces very interesting competition between the (π, π) state and the 120-degree state.

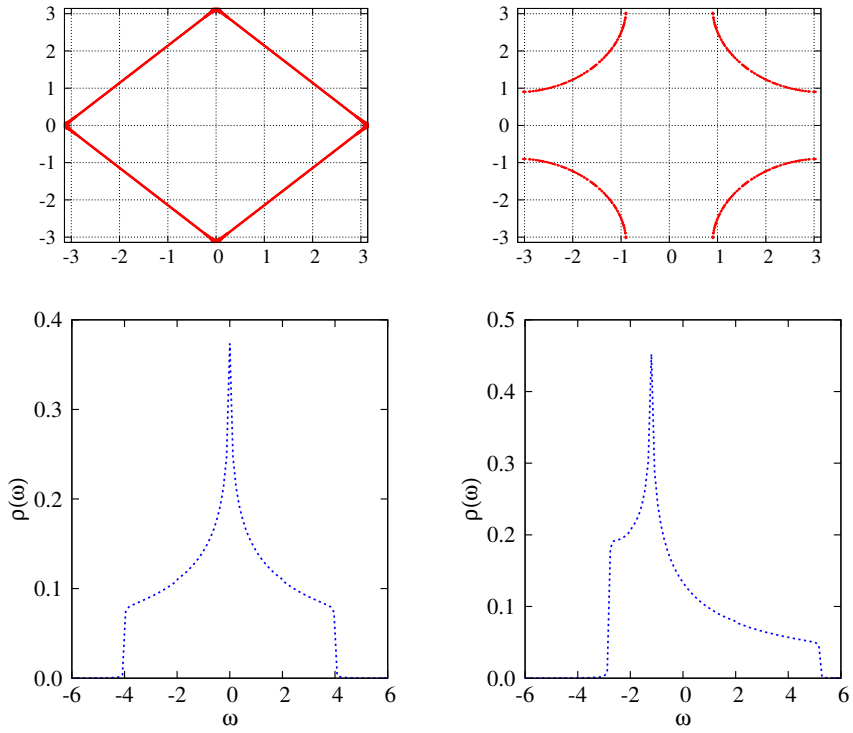

Figure 2.9: *The Fermi surface and density of state of the Hubbard model on a frustrated square lattice with different next nearest neighbor hopping amplitude. When $t'/t = 0$, the Fermi surface is nested and the density of state shows the van Hove singularity at $\omega = 0$ (see the left panel). When $t'/t = -0.3$, the nested Fermi surface is destroyed, therefore the antiferromagnetism is suppressed.*

Chapter 3

Continuous-Time Quantum Monte Carlo Methods

The accuracy of DMFT results greatly relies on the impurity solver. The widely used numerically exact impurity solvers are ED and Hirsch-Fye QMC. Both of them have their own advantages and disadvantages. ED is a good solver in zero temperature and suffers the problem of finite number of bath sites. Hirsch-Fye QMC works on finite temperature, and relatively difficult to approach the lower temperature regime. The most serious problem of Hirsch-Fye is the well-known minus sign problem.

Hirsch-Fye QMC introduces the discretization parameter L in imaginary time $[0, \beta)$, each time slice has a length of $\Delta_\tau = \beta/L$. It performs the Trotter decomposition and decouples the four fermion operator terms by Hubbard-Stratonovich transformation and introduces a collection of auxiliary fields which only have two discrete values like the Ising spin. This makes the Monte Carlo Sampling possible since the whole Hilbert space can now be represented by the configurations of Ising spins. This method has become a very widely used QMC method in solving the interacting fermion systems. The only error introduced by this method is the Trotter error which is proportional to Δ_τ^2.

With the Hirsch-Fye method it is hard to access the low temperature regime since the Hilbert Space grows rapidly with the decrease of temperature. In order to nicely control the Trotter error, one has to use more time grid points L, while this seriously increases the computational burden. To examine the low temperature properties of strong coupling systems is a serious challenge to Hirsch-Fye methods. At the same time, the Hirsch-Fye method cannot be easily extended to include non density-density interactions, such as spin-spin correlation and pairing interaction in high-temperature superconductivity.

Recently, another type of Quantum Monte Carlo method has been proposed based on the series expansion [Rubtsov *et al.* (2005); Werner *et al.* (2005); Werner and Millis (2006)]. Both of these two methods can access the low temperature regime relatively easily and can be applied to multi-band models with complicated interaction form. They do not discrete the imaginary time, thus there is no Trotter error introduced. The central idea of these two methods is to perturbatively expand the partition function $\mathcal{Z}$ and sample basically all the expansion terms by the Monte Carlo random walk. The difference between them is that in the weak-coupling expansion

method [Rubtsov *et al.* (2005)], the Coulomb interaction term is expanded, while in the strong coupling expansion method [Werner *et al.* (2005); Werner and Millis (2006)] the hybridization function is taken as the expansion parameter. In the rest of this chapter, we will present the details of these two methods including the fast update algorithm and the sampling method. And some simple but useful examples are given as illustration of the practical implementation. The performance of these two methods is also analyzed.

3.1 General concepts of ct-qmc

Here, we use the one band Hubbard Model to illustrate some basic or common features of these two ct-qmc methods.

$$H = -t \sum_{<i,j>,\sigma} (c^{\dagger}_{i\sigma} c_{j\sigma} + h.c.) + U \sum_{i} n_{i\uparrow} n_{i\downarrow} - \mu \sum_{i} n_i \tag{3.1}$$

As we have discussed in the first chapter, the partition function of a many-body interacting system governs the basic properties of the system. Once we know the partition function, we can write down all its thermodynamical properties. Generally the partition function has the following form:

$$\mathcal{Z} = Tr T_{\tau} e^{-S} \tag{3.2}$$

Action S is normally written in the coherent state basis as we did in the derivation of the DMFT equations. But here we adopt the particle number basis. In this case, the action has the form:

$$S = -\int\int_0^{\beta} t \sum_{<i,j>,\sigma} c^{\dagger}_{i\sigma}(\tau) c_{j\sigma}(\tau') d\tau d\tau' + \int_0^{\beta} U \sum_{i} n_{i\uparrow}(\tau) n_{i\downarrow}(\tau) = H_0 + H_U \tag{3.3}$$

This partition function is the starting point of both of these two methods. We split the Hamiltonian into two parts, $H = H_1 + H_2$. Here H_1(or H_2) could be or not be H_0 (or H_U), it depends on which term actually we want to expand. Here we want to keep the generality by using H_1 and H_2. In the next step, we expand the whole action over H_2.

$$\begin{aligned} \mathcal{Z} &= Tr e^{-\beta H_1} T_{\tau} e^{-\int_0^{\beta} d\tau H_2(\tau)} \\ &\sum_{k} \frac{1}{k!} \int_0^{\beta} d\tau_1 \cdots \int_0^{\beta} d\tau_n Tr[e^{-(\beta-\tau_n)H_1}(-H_2) \cdots e^{-(\tau_2-\tau_1)H_1}(-H_2) e^{-\tau_1}] \end{aligned} \tag{3.4}$$

and operator $H_2(\tau)$ with its Heisenberg definition. Suppose we know the value of $H_2(\tau)$ in each expansion term, then we can calculate the partition function for each specific expansion order k. In principle the perturbative expansion yields a power series up to the infinite order k. But the presence of factor $1/k!$ ensures only finite order terms contribute most to the partition. In order to determine the optimal perturbation order k, we use Monte Carlo random walk to sample basically each order by the corresponding weight w_c

$$w_c = Tr[e^{-(\beta-\tau_n)H_1}(-H_2) \cdots e^{-(\tau_2-\tau_1)H_1}(-H_2) e^{-\tau_1}] \tag{3.5}$$

In the following part, we discuss the two variants of the above scheme.

3.2 Weak-coupling expansion-Rubtsov method

3.2.1 General formulas

If the interaction is not very strong, one can take the interaction as a small parameter and expand the partition function over it. This is the basic idea of the Rubtsov method. For generality, we consider the one band Hubbard model which has the following action,

$$S = -\iint_0^\beta t \sum_{<i,j>,\sigma} c_{i\sigma}^\dagger(\tau) c_{j\sigma}(\tau') d\tau d\tau' + \int_0^\beta U \sum_i n_{i\uparrow}(\tau) n_{i\downarrow}(\tau) \tag{3.6}$$

One important feature of Rubtsov method is that it introduces another parameter α to decrease the influence of the minus sign problem. It is equivalent to shift the chemical potential μ. With α, the non-interacting action becomes

$$S_0 = \iint_0^\beta d\tau d\tau' \sum_{<i,j>\sigma} (-t + \alpha_{i\bar{\sigma}} U \delta_{i,j})\, c_{i\sigma}^\dagger(\tau) c_{j\sigma}(\tau') \tag{3.7}$$

The interaction term will be written as:

$$W = \int_0^\beta U \sum_i [c_{i\uparrow}^\dagger c_{i\uparrow}(\tau) - \alpha_\uparrow][c_{i\downarrow}^\dagger c_{i\downarrow}(\tau) - \alpha_\downarrow] d\tau \tag{3.8}$$

Now split the partition function into two terms H_1 and H_2, take $H_2 = H_U$. Then the partition function is expanded as

$$\mathcal{Z} = Tr T_\tau e^{-S_0} \sum_{k=0}^\infty \frac{(-U)^k}{k!} \sum_{\{a\}} \int d\tau_{a_1} \cdots \int d\tau_{a_k} \prod_{i=1}^{2k} [c_{a_i}^\dagger c_{a_i}(\tau_{a_i}) - \alpha_{a_i}] \tag{3.9}$$

Here a represents site index and spin direction. The sum over $\{a\}$ can be written explicitly as $\sum_i \sum_\sigma$. This is the typical way of doing perturbative expansion over the Coulomb interaction term. Various analytical methods, like RPA, FLEX and TPSC, consider a subset of diagrams from this expansion. Here, we are going to take basically all the expansion orders into account.

The evaluation of trace can be written as thermal average with respect to the non-interacting action S_0.

$$\mathcal{Z}_k = \langle T[(c_{a_1}^\dagger c_{a_1}(\tau_{a_1}) - \alpha_{a_1}) \cdots (c_{a_{2k}}^\dagger c_{a_{2k}}(\tau_{a_{2k}}) - \alpha_{a_{2k}})] \rangle \tag{3.10}$$

Now the total partition function becomes

$$\mathcal{Z} = \mathcal{Z}_0 \sum_k \frac{(-U)^k}{k!} \int_0^\beta d\tau_{a_1} \cdots \int_0^\beta d\tau_{2k} \mathcal{Z}_k \tag{3.11}$$

where $\mathcal{Z}_0$ is the partition function for the non-interacting action $\mathcal{Z}_0 = Tr e^{-S_0}$. To evaluate the trace in $\mathcal{Z}_k$, basically one has to rewrite each operator in the eigenstate basis of H_0, and perform matrix production from the beginning to the end according

to the right time sequence. While here H_0 is a non-interacting Hamiltonian, the Wicks theorem works. Furthermore, the spin-up and spin-down component are totally independent to each other, thus $\mathcal{Z}_k$ reduces to the product of that for each spin

$$\mathcal{Z}_k = \mathcal{Z}_k^{\uparrow} \cdot \mathcal{Z}_k^{\downarrow} \tag{3.12}$$

With the help of Wicks theorem, each trace can be written as a determinant

$$\mathcal{Z}_k^{\sigma} = det \begin{pmatrix} \mathcal{G}^{\sigma}_{a_1,a_1}(\tau_{a_1},\tau_{a_1}) - \alpha_\sigma & \mathcal{G}^{\sigma}_{a_1,a_2}(\tau_{a_1},\tau_{a_k}) & \cdots & \mathcal{G}_{a_1,a_k}(\tau_{a_1},\tau_{a_k}) \\ \mathcal{G}^{\sigma}_{a_2,a_1}(\tau_{a_2},\tau_{a_1}) & \mathcal{G}^{\sigma}_{a_2,a_2}(\tau_{a_2},\tau_{a_2}) - \alpha_\sigma & \cdots & \mathcal{G}^{\sigma}_{a_2,a_k}(\tau_{a_2},\tau_{a_k}) \\ \vdots & \vdots & \cdots & \vdots \\ \mathcal{G}^{\sigma}_{a_k,a_1}(\tau_{a_k},\tau_{a_1}) & \mathcal{G}^{\sigma}_{a_k,a_2}(\tau_{a_k},\tau_{a_2}) & \cdots & \mathcal{G}^{\sigma}_{a_k,a_k}(\tau_{a_k},\tau_{a_j}) - \alpha_\sigma \end{pmatrix} \tag{3.13}$$

where $\mathcal{G}_\sigma(\tau,\tau') = -\langle T_\tau c_\sigma(\tau) c_\sigma^\dagger(\tau')\rangle$ is the Green's function measured with respect to action S_0. In each specific order k, the resulting determinant for each spin can be calculated from a $k \times k$ matrix which elements are known to us. The evaluation of determinant is always time consuming, especially for larger k. While the determinant for order k can be easily obtained if we know that for order $k+1$ or $k-1$, see Appendix A.

3.2.2 Quantum random walk

In perturbation theory, in principle one has to consider all the perturbation terms in the series expansion. But in practice, the terms corresponding to the order beyond some cutoff point contribute little. The most important contribution normally comes from the lower order terms. Since at each order k we can basically know the partition function $\mathcal{Z}_k$, to obtain the full partition function now only requires the value of k. From the analysis of the determinant calculation (see Appendix A), it is reasonable to think that it might be helpful if we calculate the partition function order by order, and compare their weights to see which terms contribute to the partition function most. In this way, the optimal order k can be determined. To practically apply this idea, we perform Monte Carlo random walk in k space.

$$\mathcal{Z} = \mathcal{Z}_0 + \cdots + \overbrace{\mathcal{Z}_{k-2} + \underbrace{\mathcal{Z}_{k-1} + \mathcal{Z}}_{k-1}}^{k-2} \overbrace{\underbrace{k + \mathcal{Z}_{k+1}}_{k+1} + \mathcal{Z}_{k+2}}^{k+2} + \cdots \tag{3.14}$$

MC random walk has two possible directions, either increasing k or decreasing k. In each walk, the weight (or the partition function) of the current order k can be calculated. The MC walk to each direction is determined by the ratio of these two adjacent weights $w_c^{(k)}$ and $w_c^{(k\pm1)}$ which is called the detailed balance condition. Eventually, this condition depends on the determinant ratio $\mathcal{Z}^{k+1}/\mathcal{Z}^k$. From the above description, one can notice that this random walk is in one dimensional space, and normally, the procedure of increasing/decreasing the perturbation order by one is already enough for the ergodicity[1].

[1] Sometimes, the $k \to k\pm2$ are needed in order to avoid trapping into only part of configurations, and globally change the time configuration is also needed sometimes especially in the magnetic ordered state.

Once we know the partition function, we can measure the one particle Green's function $G_{a,a'}(\tau,\tau') = -\langle T_\tau c_a(\tau)c^\dagger_{a'}(\tau')\rangle$, here the thermal average is taken with respect to the full partition function. Under the series expansion over the interaction term, it becomes

$$G^{(k)}_{a,a'}(\tau,\tau_\prime) = \frac{\left\langle Tc^\dagger_{a'}(\tau')c_a(\tau)(c^\dagger_{a'_1}c_{a_1}-\alpha)\cdots(c^\dagger_{a'_k}c_{a_k}-\alpha)\right\rangle_0}{\left\langle T(c^\dagger_{a'_1}c_{a_1}-\alpha)\cdots(c^\dagger_{a'_k}c_{a_k}-\alpha)\right\rangle_0} \tag{3.15}$$

Note, now in each Monte Carlo step G depends on order k. Here, we have dropped the spin index and the evaluation of G only dependents on trace in the same spin sector. As we have discussed, the thermal average with respect to S_0 can be written as a determinant, thus the above equation is easily written as

$$G^{(k)}_{a,a'}(\tau,\tau') = \frac{\mathcal{Z}^{(k+1)}}{\mathcal{Z}^{(k)}} = \frac{Det\begin{pmatrix}\bar{\mathcal{G}}^{(k)} & \mathcal{G}_{a_i,a'}(\tau_i,\tau') \\ \mathcal{G}_{a,a_j}(\tau,\tau_j) & \mathcal{G}_{a,a'}(\tau,\tau')\end{pmatrix}}{Det\bar{\mathcal{G}}^{(k)}} \tag{3.16}$$

This determinant ratio is easily calculated from a 2×2 block matrix operation, finally we obtain

$$G_{a,a'}(\tau,\tau') = \mathcal{G}_{a,a'}(\tau,\tau') - \sum_{i,j}\mathcal{G}_{a,a_i}(\tau,\tau_i)\bar{\mathcal{G}}^{-1}_{i,j}\mathcal{G}_{a_j,a'}(\tau_j,\tau') \tag{3.17}$$

In imaginary frequency space, this equation becomes

$$G_{a,a'}(\omega) = \mathcal{G}_{a,a'}(\omega) - \mathcal{G}_{a,a'}(\omega)\left[\frac{1}{\beta}\sum_{i,j}M_{i,j}e^{i\omega(\tau_i-\tau_j)}\right]\mathcal{G}_{a,a'}(\omega) \tag{3.18}$$

where $M=\bar{\mathcal{G}}^{-1}$, $\bar{\mathcal{G}}$ is the matrix whose determinant is $\mathcal{Z}_k$, see Eq. (3.13).

To get the M-matrix is the central task of this method. We update this matrix in the incremental and decremental step according to a certain ratio. Normally the metropolis sampling method is enough for this job. For more details of the update method, the reader is refereed to Appendix. A. Every time, one gets a new M-matrix from the previous one. After several MC steps for warmup, one can sample the M-matrix and get the Green's function directly from this matrix.

Here, we use a simple example to illustrate the power of this method. Single-atom Hubbard model is a good choice since we know the exact Green's function

$$G(i\omega) = \frac{1-n}{i\omega+\mu} + \frac{n}{i\omega+\mu-U} \tag{3.19}$$

here, $n = (e^{\beta\mu}+e^{\beta(2\mu-U)})/(1+2e^{\beta\mu}+e^{\beta(2\mu-U)})$. At half-filling case $n=0.5$. The following figure illustrates the comparison of the numerical result and the exact one. Here, we take α as 0.45. The distribution of the history diagram is also presented below.

From the comparison with analytical results, CTQMC gives satisfactory results for the one-particle Green's function. Note in the histogram diagram, each odd order

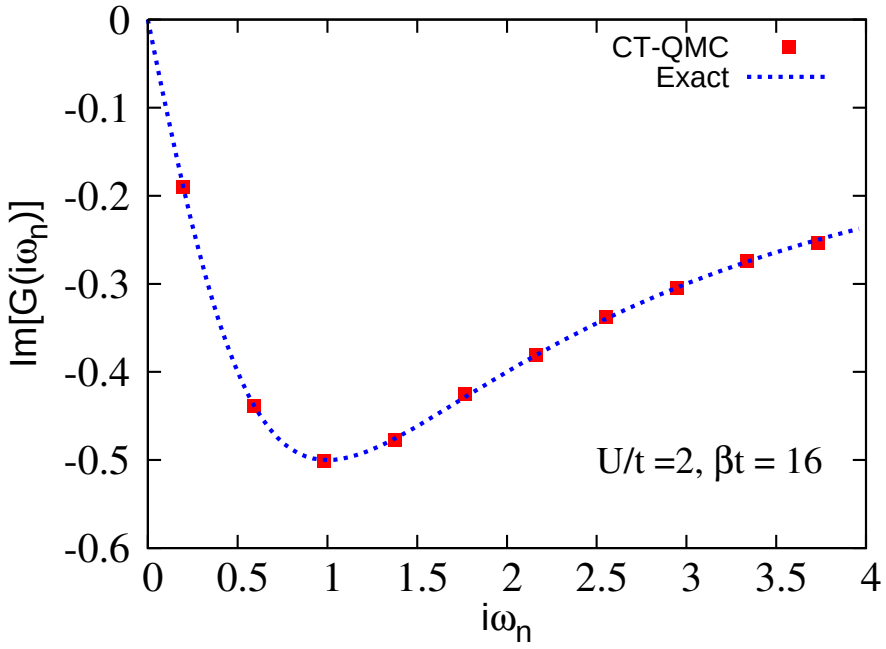

Figure 3.1: *The Green function for the single atom Hubbard Model. As comparison the analytical result is also given.*

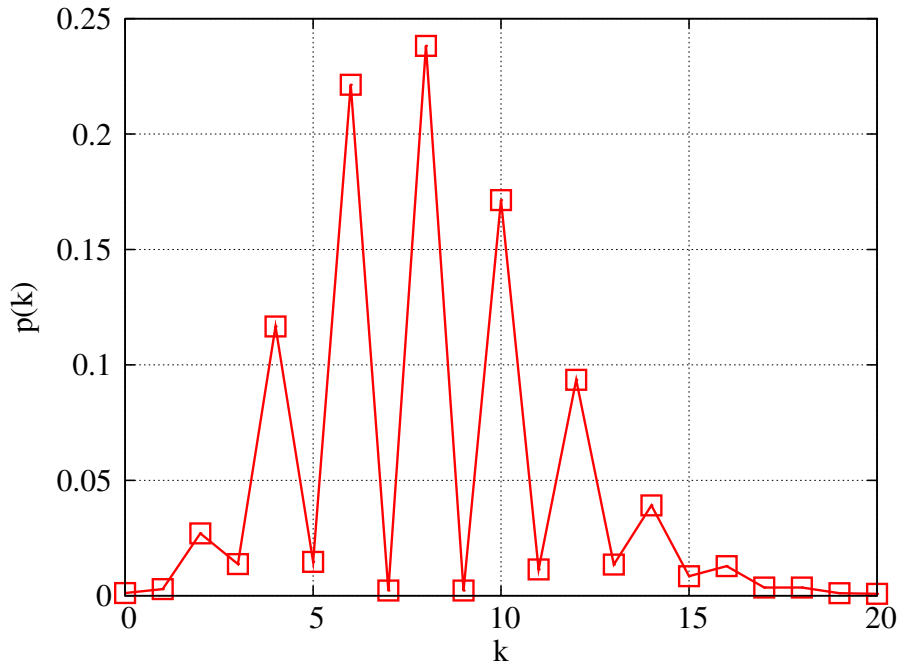

Figure 3.2: *Distribution of the perturbation order for single site Hubbard model at* $U/t = 2$ *and* $\beta t = 16$.

has very low probability since we choose $\alpha = 0.45$ which is closed to $\mathcal{G}(0) = 0.5$. Thus the diagonal elements in the determinant matrix are closed to zero. The determinant value for odd order terms are therefore very small. The move to such terms is hard to be accepted by the MC random walk.

This method can be used as impurity solver not only for single site DMFT, but also for various cluster extentions of DMFT which we will discuss later on. In the remainder this section, we will discuss the functionality of parameter α, which is introduced for reducing the minus sign problem. The single site Hubbard model serves as an example.

Corresponding to single atom Hubbard model, the action can be separated into two parts as following:

$$S_0 = \int [(-\mu + U\alpha_\downarrow)n_\uparrow(\tau) + (-\mu + U\alpha_\uparrow)n_\downarrow(\tau)]d\tau \tag{3.20}$$

$$W = U \int (n_\downarrow(\tau) - \alpha_\downarrow)(n_\uparrow(\tau) - \alpha_\uparrow)d\tau \tag{3.21}$$

S_0 consists of the non-interacting partition function $\mathcal{Z}_0$. Since there is no spin flip term in this model, the operators corresponding to up and down spins can be separated completely. Therefore, $\Omega_k = (-U)^k/k!\mathcal{Z}_k$ looks like

$$\Omega_k = \frac{(-U)^k}{k!} \det D_\uparrow^{(k)} \det D_\downarrow^{(k)} \tag{3.22}$$

In the eigenvalues basis ($|0>, |\uparrow>, |\downarrow>, |\uparrow\downarrow>$), $D_\uparrow^{(k)}$-function can be written as:

$$\begin{pmatrix} (-\alpha_\uparrow)^k & & & \\ & e^{\beta(\mu - U\alpha_\downarrow)}(1-\alpha_\uparrow)^k & & \\ & & (-\alpha_\uparrow)^k & \\ & & & e^{\beta(\mu - U\alpha_\downarrow)}(1-\alpha_\uparrow)^k \end{pmatrix} \tag{3.23}$$

Taking the trace of this matrix, one obtains that $\det D_\uparrow^{(k)} = 2\alpha_\uparrow^k[1 + e^{\beta(\mu - U\alpha_\downarrow)}(1 - \alpha_\uparrow^{-1})^k]$. Therefore,

$$\Omega_k = 4\frac{(-U\alpha_\uparrow\alpha_\downarrow)^k}{k!}[1 + e^{\beta(\mu - U\alpha_\downarrow)}(1-\alpha_\uparrow^{-1})^k][1 + e^{\beta(\mu - U\alpha_\uparrow)}(1-\alpha_\downarrow^{-1})^k] \tag{3.24}$$

For the negative interaction($U < 0$), Ω_k is always positive for any value of α, there is no minus sign problem. This conclusion is also true for the one dimensional Hubbard model, see [Assaad and Lang (2007)]. For the repulsion case, if we take $\alpha_\uparrow + \alpha_\downarrow = 1$, Ω_k has a form like:

$$\Omega_k = e^{\beta(\mu - U\alpha)}\frac{(U\alpha^2)^k}{k!}[1 + e^{\beta(\mu - U + U\alpha)}(1-\alpha^{-1})^k][1 + e^{\beta(-\mu + U\alpha)}(1-\alpha^{-1})^k] \tag{3.25}$$

Ω_k is still positive for any α. In conclusion, we have no minus sign problem for the negative interacting case, and also the positive interacting case if we take the condition that $\alpha_\uparrow + \alpha_\downarrow = 1$. The introduction of the parameter α is equivalent to applying an external Ising field on the system. For spin up and spin down sector, α takes specific values. One can also take α randomly, which improves the sampling and allows to retain the original H_0. [Assaad and Lang (2007)]

3.3 Strong-coupling expansion-Werner method

Rubtsov's method overcomes some drawbacks of Hirsch-Fye algorithm and effectively improves the ability to study the low temperature regime. In this method, the perturbation order increases with interaction U, it is the same for the computational burden. Philipp Werner and his collaborators proposed another continuous time method [Werner *et al.* (2005); Werner and Millis (2006)] which is slightly different from Rubtsov's in this sense. Werner's method is based on the expansion of the hybridization term between the system and bath. The interaction term is taken as part of the local term and is evaluated exactly. As a result, the perturbation order decreases with the increase of the interaction strength. This method is called strong coupling CTQMC and is especially suitable for investigating the strong interaction regime.

In this section we discuss two practical implementations of the strong-coupling CTQMC, which are proposed by P. Werner [Werner and Millis (2006)][2] and K. Haule [Haule (2007)][3]. The similarity and difference will be discussed. The single site and single band impurity problem turns out to be a very special case in the multi-band implementation, which allows us to simulate more efficiently in the so-called segment representation.

3.3.1 General Formalism

Suppose we have a multi-impurity problem with fermions labeled by $a = 1, \cdots, N$, this label includes the spin, site and orbital indices. We call them as flavor. Such a multi-impurity problem is solved in the cluster version of DMFT by separating the degree of freedom of the cluster in the total Hamiltonian with those of the bath. Then the total Hamiltonian is given as

$$H = H_{loc} + H_{bath} + H_{hyb} + H_{hyb}^{\dagger} \tag{3.26}$$

The bath is non-interacting with a Gaussian form Hamiltonian. The hybridization part can be written as $H_{hyb} = \sum_{ab} V_{ab} c_a^{\dagger} c_b$. V_{ab} is the hybridization strength between the cluster and its bath which needs to be determined self-consistently. The total partition function then is expressed as

$$\mathcal{Z} = Tr_{ab} T_{\tau} e^{-\int_0^{\beta} [H_{loc}(\tau) + H_{bath}(\tau) + H_{hyb}(\tau) + H_{hyb}^{\dagger}(\tau)]} \tag{3.27}$$

Trace is taken over both the cluster and bath degrees of freedom. Here we expand the partition function over the hybridization term.

$$\mathcal{Z} = T_{\tau} Tr_a e^{-\int_0^{\beta} H_{loc}} Tr_b e^{-\int_0^{\beta} H_{bath}} \sum_{k_1} \frac{1}{k_1!} [H_{hby}(\tau)]^{k_1} \sum_{k_2} \frac{1}{k_2!} [H_{hby}^{\dagger}(\tau)]^{k_2} \tag{3.28}$$

It is easily understood that $k_1 = k_2 = k$ since the integration over the bath degrees of freedom requires that the creation and annihilation operators are paired. Explicitly

[2]Here, we call it the multi-band implementation since in this method each flavor decouples to the other. The hybridization function is given in a diagonal matrix form.

[3]Here, we call it the multi-site implementation since it does not diagonalize the hybridization function and is in principle more suitable for the larger cluster implementation.

write down the expression of H_{hyb} and $H_{hyb}^{\dagger}$ in the above equation, the total partition function looks like

$$\begin{aligned}\mathcal{Z} =&\mathcal{Z}_b T_\tau Tr_a e^{-\int_0^\beta H_{loc}} \sum_k \frac{1}{k!} \int_0^\beta \prod_{i=1}^k d\tau_i \int_0^\beta \prod_{i=1}^k d\tau_i' \sum_{aa'} \prod_{i=1}^k [c_{a_i'}(\tau_i') c_{a_i}^\dagger(\tau_i)] \times \\ &\frac{1}{k!}\frac{1}{\mathcal{Z}_b} e^{-\int_0^\beta H_{bath}} \prod_{i=1}^k \sum_{bb'} [V_{a_i b_i} V_{b_i' a_i'} c_{b_i}^\dagger(\tau_i) c_{b_i'}(\tau_i')]\end{aligned} \tag{3.29}$$

where $\mathcal{Z}_b = Tr_b e^{-\int_0^\beta H_{bath}}$. Since the bath is totally non-interacting, the integration over the bath degrees of freedom now can be performed exactly, which yields the hybridization function.

$$\Delta_{aa'}(\tau_i, \tau_i') = \frac{1}{\mathcal{Z}_b} e^{-\int_0^\beta H_{bath}} \sum_{bb'} [V_{a_i b_i} V_{b_i' a_i'} c_{b_i}^\dagger(\tau_i) c_{b_i'}(\tau_i')] \tag{3.30}$$

The existence of the production from 1 to k in the front of the sum over bb' makes the total integral over the bath degree of freedom to be a determinant from the Wicks theorem. Then the total partition function becomes

$$\begin{aligned}\mathcal{Z} =&\mathcal{Z}_b T_\tau Tr_a e^{-\int_0^\beta H_{loc}} \sum_k \frac{1}{k!} \int_0^\beta \prod_{i=1}^k d\tau_i \int_0^\beta \prod_{i=1}^k d\tau_i' \sum_{aa'} \prod_{i=1}^k [c_{a_i'}(\tau_i') c_{a_i}^\dagger(\tau_i)] \times \\ &\times \frac{1}{k!} Det \begin{pmatrix} \Delta_{a_1 a_1'}(\tau_1, \tau_1') & \Delta_{a_1 a_2'}(\tau_1, \tau_2') & \cdots & \Delta_{a_1 a_k'}(\tau_1, \tau_k') \\ \Delta_{a_2 a_1'}(\tau_2, \tau_1') & \Delta_{a_2 a_2'}(\tau_2, \tau_2') & \cdots & \Delta_{a_2 a_k'}(\tau_2, \tau_k') \\ \vdots & \vdots & \cdots & \vdots \\ \Delta_{a_k a_1'}(\tau_k, \tau_1') & \Delta_{a_k a_2'}(\tau_k, \tau_2') & \cdots & \Delta_{a_k a_k'}(\tau_k, \tau_k') \end{pmatrix}\end{aligned} \tag{3.31}$$

Now the bath degrees of freedom have been integrated out which turns to be the hybridization function acting on the cluster degrees of freedom , working like an external field. Since the hybridization functions are just complex numbers, to know the total partition function we now need to know the trace over the cluster degrees of freedom.

$$T_\tau Tr_a e^{-\int_0^\beta H_{loc}} \prod_{i=1}^k [c_{a_i'}(\tau_i') c_{a_i}^\dagger(\tau_i)] = \mathcal{Z}_{loc} < T_\tau c_{a_1'}(\tau_1') c_{a_1}^\dagger(\tau_1) \cdots c_{a_k'}(\tau_k') c_{a_k}^\dagger(\tau_k) > \tag{3.32}$$

Finally, we obtain the following equation for the total partition function

$$\begin{aligned}\mathcal{Z} =&\mathcal{Z}_b \mathcal{Z}_{loc} \sum_k \frac{1}{k!} \int_0^\beta \prod_{i=1}^k d\tau_i \int_0^\beta \prod_{i=1}^k d\tau_i' \sum_{aa'} \langle T_\tau c_{a_1'}(\tau_1') c_{a_1}^\dagger(\tau_1) \cdots c_{a_k'}(\tau_k') c_{a_k}^\dagger(\tau_k) \rangle \\ &\times \frac{1}{k!} Det \begin{pmatrix} \Delta_{a_1 a_1'}(\tau_1, \tau_1') & \Delta_{a_1 a_2'}(\tau_1, \tau_2') & \cdots & \Delta_{a_1 a_k'}(\tau_1, \tau_k') \\ \Delta_{a_2 a_1'}(\tau_2, \tau_1') & \Delta_{a_2 a_2'}(\tau_2, \tau_2') & \cdots & \Delta_{a_2 a_k'}(\tau_2, \tau_k') \\ \vdots & \vdots & \cdots & \vdots \\ \Delta_{a_k a_1'}(\tau_k, \tau_1') & \Delta_{a_k a_2'}(\tau_k, \tau_2') & \cdots & \Delta_{a_k a_k'}(\tau_k, \tau_k') \end{pmatrix}\end{aligned} \tag{3.33}$$

Here, $\mathcal{Z}_{loc} = Tr_a e^{-\int_0^\beta H_{loc}}$. The evaluation of the trace over the local variables is exactly same as we discussed in the introduction of this thesis. One has to know all the eigenvalues and eigenstates of the local Hamiltonian. The operator c and $c^\dagger$ will be expressed as matrix under the eigenstate basis. The evaluation of trace becomes the determination the diagonal elements of the total matrix production which we will discuss more detail later on.

For the current problem, we have N flavors, which could be site, band and spin. Let's take flavor as site index now. The local Hamiltonian is given as

$$H_{loc} = -t \sum_{<i,j>=1}^{N} \sum_{\sigma} (c_{i\sigma}^\dagger c_{j\sigma} + h.c.) + U \sum_{i=1}^{N} n_{i\uparrow} n_{i\downarrow} - \mu \sum_{i=1}^{N} n_i \tag{3.34}$$

The self-consistent condition for such a many-impurity problem dependents on the specific DMFT methods we are going to use. But no matter which method we choose, the resulting hybridization function will be a $N \times N$ matrix. One simplification happens if we can actually diagonalize the hybridization matrix which in the end results in the multi-band implementation presented in the work of P. Werner [Werner and Millis (2006)].

3.3.2 Multi-Band Implementation

Suppose we can find a uniform transformation $\mathcal{U}$ which does not depend on frequency and it can actually diagonalize the hybridization function, then it can also diagonalize the hopping matrix in the local Hamiltonian, since they have the same property. At the same time, we also need to apply this transformation on the interaction part. $\tilde{H}_{loc} = \mathcal{U} H_{loc} \mathcal{U}^\dagger$. Note that such diagonalization is different from the full diagonalization of the total Hamiltonian, from which we can determine all the eigenvalues and eigenstates. Here the diagonalization is only for the one particle part in the local Hamiltonian, since we are going to make the hybridization function diagonal. Normally, such transformation will lead to a more complicated interaction form in the end. It might be the spin-spin interaction or the pair-pair interaction which are difficult dealt with in the other methods, for example Hirsch Fye QMC. But it does not bring in too much computational burden in the strong-coupling CTQMC since we keep the local Hamiltonian unchanged during the expansion. And such diagonalization of the hybridization function introduces a great simplification for simulation.

Before discussing the advantage of such transformation, we give a simple example – the two sites Hubbard model. It is local Hamiltonian is obtained easily by taking $N = 2$ in Eq. (3.34)

$$H_{loc} = -t \sum_{\sigma} (c_{1\sigma}^\dagger c_{2\sigma} + c_{2\sigma}^\dagger c_{1\sigma}) + U n_{1\uparrow} n_{1\downarrow} + U n_{2\uparrow} n_{2\downarrow} - \mu (n_1 + n_2) \tag{3.35}$$

Taking the uniform transformation as $\mathcal{U} = \frac{1}{\sqrt{2}} \begin{pmatrix} 1 & 1 \\ -1 & 1 \end{pmatrix}$. The above local Hamilto-

nian will be transformed to be

$$\tilde{H}_{loc} = -(\mu+t)n_a - (\mu-t)n_b + \frac{U}{2}[\sum_{i}^{a,b} n_{i\uparrow}n_{i\downarrow} + \sum_{i\neq j}^{a,b} n_{i\uparrow}n_{j\downarrow} - (a_\uparrow^\dagger a_\downarrow^\dagger b_\uparrow b_\downarrow + a_\downarrow^\dagger b_\uparrow^\dagger b_\downarrow a_\uparrow + h.c.)] \tag{3.36}$$

Here $a_\sigma = \frac{1}{\sqrt{2}}(c_{1\sigma} + c_{2\sigma})$, $b_\sigma = \frac{1}{\sqrt{2}}(c_{2\sigma} - c_{1\sigma})$. Now, the one particle part has been diagonalized. It is equivalent to the single site two-band model. Each band has a hybridization function which is not coupled to any other band. We can take each band as a flavor, then all elements in each hybridization function matrix in Eq. (3.33) must come from the same flavor. In this case, Eq. (3.33) can be written as

$$\begin{aligned}\mathcal{Z} =& \mathcal{Z}_b\mathcal{Z}_{loc}\sum_k \frac{1}{k!}\int_0^\beta \prod_{i=1}^k d\tau_i \int_0^\beta \prod_{i=1}^k d\tau_i' \langle T_\tau \prod_a c_a(\tau_1')c_a^\dagger(\tau_1)\cdots c_a(\tau_k')c_a^\dagger(\tau_k)\rangle \\ &\times \prod_a \frac{1}{k_a!} Det \begin{pmatrix} \Delta_a(\tau_1,\tau_1') & \Delta_a(\tau_1,\tau_2') & \cdots & \Delta_a(\tau_1,\tau_k') \\ \Delta_a(\tau_2,\tau_1') & \Delta_a(\tau_2,\tau_2') & \cdots & \Delta_a(\tau_2,\tau_k') \\ \vdots & \vdots & \cdots & \vdots \\ \Delta_a(\tau_k,\tau_1') & \Delta_a(\tau_k,\tau_2') & \cdots & \Delta_a(\tau_k,\tau_k') \end{pmatrix}\end{aligned} \tag{3.37}$$

Note that the total determinant of the hybridization matrix now becomes the product of it in each flavor a. During the simulation, one only needs to calculate the new determinant in one specific flavor in stead of working for all the flavors. The total perturbation order (half of the total number of the operators in the trace) is given as the sum of the perturbation order for each flavor. $k = \sum_a k_a$.

Single Band – Graphical Representation

If there is only one band in Eq. (3.37), we can further simplify it as

$$\begin{aligned}\mathcal{Z} =& \mathcal{Z}_b\mathcal{Z}_{loc}\sum_k \frac{1}{k!}\int_0^\beta \prod_{i=1}^k d\tau_i \int_0^\beta \prod_{i=1}^k d\tau_i' \langle T_\tau c(\tau_1')c^\dagger(\tau_1)\cdots c(\tau_k')c^\dagger(\tau_k)\rangle \\ &\times \frac{1}{k!} Det \begin{pmatrix} \Delta(\tau_1,\tau_1') & \Delta(\tau_1,\tau_2') & \cdots & \Delta(\tau_1,\tau_k') \\ \Delta(\tau_2,\tau_1') & \Delta(\tau_2,\tau_2') & \cdots & \Delta(\tau_2,\tau_k') \\ \vdots & \vdots & \cdots & \vdots \\ \Delta(\tau_k,\tau_1') & \Delta(\tau_k,\tau_2') & \cdots & \Delta(\tau_k,\tau_k') \end{pmatrix}\end{aligned} \tag{3.38}$$

The simulation of this partition function turns to be very simple in the segment picture, where the determinant and the trace can be efficiently evaluated if there is only density-density interaction present in the impurity Hamiltonian. This originates from the fact that ψ and $\psi^\dagger$ appear alternatively in the trace after the time ordering operation[4].

Let us take the third order expansion term as example. In the segment representation, any order term can be represented as a collection of segments in $[0, \beta)$. The segment is the representation of the occupied state. Corresponding to the third order term, the general configuration is illustrated in Fig. 3.3. Both the trace value and the determinant can be calculated from this diagram. The empty circle and

[4]One can easily prove that $\psi\psi = \psi^\dagger\psi^\dagger = 0$ if there only has density-density interaction in the Hamiltonian.

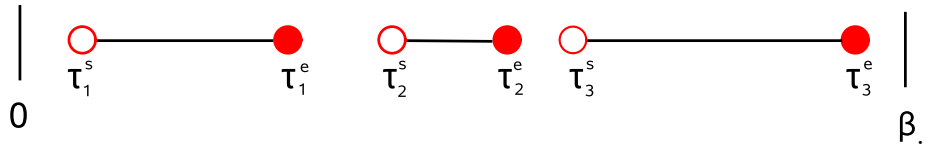

Figure 3.3: *General configuration of a collection of segments. Here $k = 3$ terms is taken for example.*

solid dot are the creation and annihilation operators respectively. Any connection between one creation and annihilation operator represents a propagator from the creation time τ^s to annihilation time τ^e. The sum of all the possible connections consists of the determinant of this order. We can illustrate this diagram form in the following way. The determinant of the third order term takes the form

$$\begin{vmatrix} \Delta(\tau_1^e - \tau_1^s) & \Delta(\tau_1^e - \tau_2^s) & \Delta(\tau_1^e - \tau_3^s) \\ \Delta(\tau_2^e - \tau_1^s) & \Delta(\tau_2^e - \tau_2^s) & \Delta(\tau_2^e - \tau_3^s) \\ \Delta(\tau_3^e - \tau_1^s) & \Delta(\tau_3^e - \tau_2^s) & \Delta(\tau_3^e - \tau_3^s) \end{vmatrix} \tag{3.39}$$

Every term in this determinant can be represented by the corresponding diagram in Fig. 3.4, and the whole determinant is represented by the configuration diagram 3.3. In this graph, one should note that the last diagram in this graph has negative weight. In fact, all the diagrams which have an odd number of crossing dashed lines have negative weight. Therefore, any sampling which only considers part of the diagrams in this segment representation will run into a sign problem. One should seriously take into account all the diagrams in each order.

To know the optimal value of perturbation order k, we performed Monte Carlo random walk in the space of perturbation order as we did in the weak-coupling method. This is realized in the segment representation by two types of update. One for segment, the other is for anti-segment which is the part between two segments and it represents an empty state or a hole. For each type of update, one can consider to insert or remove segment/anti-segment operation. For example, one can insert a segment in any empty part(or on an anti-segment) which finally increases the perturbation order by one. One also can remove any existing segment to decrease the perturbation order. It is similar for the operation of anti-segment. The detailed update procedure and calculation of the determinant ratio can be found in the Appendix A.

In Monte Carlo simulation, the random walk in fact is not really random. It is controlled by the weight function which eventually relates with the so-called detailed balance condition. Naive random sampling of the whole configuration space does not work. The solution to this problem has been known for long time. One has to use the important sampling technique which is designed to draw the configurations according to their Boltzmann weight $P[\{\sigma_i\}]$. A simpler sufficient and more frequently used condition for a Markov chain is the detailed balance:

$$p[\{\sigma_i\}]W(\{\sigma_i\} \longrightarrow \{\sigma_i'\}) = p[\{\sigma_i'\}]W(\{\sigma_i'\} \longrightarrow \{\sigma_i\}) \tag{3.40}$$

In order to illustrate this condition in both weak and strong coupling CTQMC, we

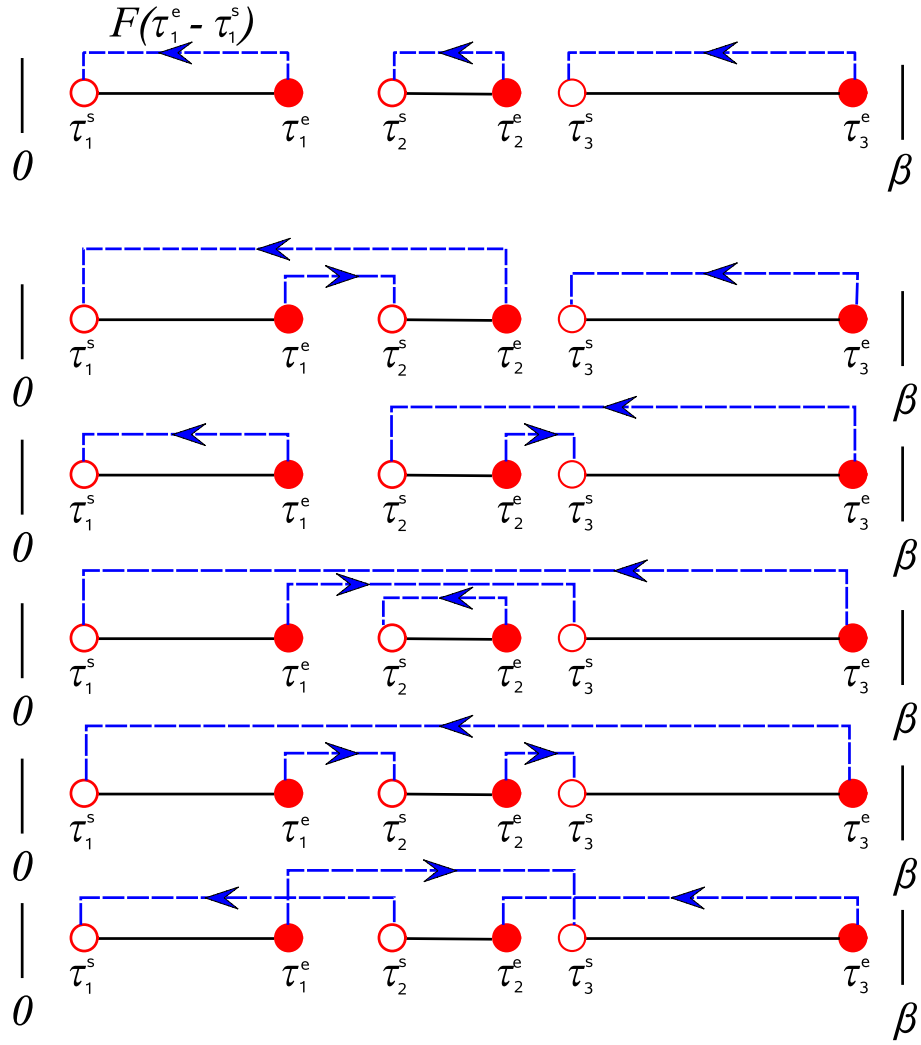

Figure 3.4: *Graphical representation of the determinant of the third order term in the perturbation expansion.*

start with a k dimensional M-matrix[5] and want to increase the dimension of this matrix[6] by one. From the above general formula of Monte Carlo important sampling, we can see that

$$\frac{p_{k\to k+1}}{p_{k+1\to k}} = \frac{W_{k+1\to k}}{W_{k\to k+1}} \tag{3.41}$$

This fraction can be easily written as the ratio of the integrand of partition function. It's easy to prove that all the conditions are fulfilled by this kind of choice. The detailed balance for the weak-coupling and the strong-coupling method are in fact

[5]In strong-coupling CTQMC, it means that we have a collection of segments

$$s_k = (\tau_1^s, \tau_1^e; \tau_2^s, \tau_2^e, \cdots; \tau_k^s, \tau_k^e)$$

.

[6]In the weak-coupling method, it means moving k to $k+1$, and both the new row and column will locate at $k+1$-th row and $k+1$-th column in this M-matrix. In the strong-coupling method, it means inserting a new segment/anti-segment in this collection of segments.

the same. In order to show this, we use the following general formula to express the perturbation expansion of the partition function. One can write it in a more explicit way with respect to different expansion method.

$$\mathcal{Z} = \mathcal{Z}_0 \sum_{k=0}^{\infty} \mathcal{Z}_k \tag{3.42}$$

here, $\mathcal{Z}_0$ is the partition function for the action which is not expanded[7]. $\mathcal{Z}_k$ is the k-th order expansion term of the partition function.

$$\mathcal{Z}_k = \int dr_1 \int dr'_1 \cdots \int dr_{2k} \int dr'_{2k} P_\alpha \det(M_k^{-1}) \tag{3.43}$$

The pre-factor P_α represents the product of the other terms in this expansion except for the determinant and the integral over r is a combination of integral over imaginary time and summation of spin direction. In the weak-coupling method, this pre-factor is a constant, see below. In the strong-coupling method it also includes the influence from the local part of the partition function.[8] In this notation, the detailed balance condition has a form like

$$\frac{p_{k\to k+1}}{p_{k+1\to k}} = \frac{W_{k+1\to k}}{W_{k\to k+1}} = \frac{P_{k+1}\det(M_{k+1}^{-1})d^4r}{P_k \det(M_k^{-1})} \tag{3.44}$$

The integral between k-th order and $(k+1)$-the order are different by d^4r, which represents dr_{2k+1}, dr'_{2k+1},dr_{2k+2},dr'_{2k+2}. The determinant ratio is obtained in the fast-update algorithm shown in Appendix A. In the weak-coupling method, we randomly choose an imaginary time in the range of $[0, \beta)$, the probability of this choice is proportional to β. Note that in each expansion order, we have a factor $(-U)^k/k!$. Thus basically $P_k \propto (-\beta U)^k/k!$.

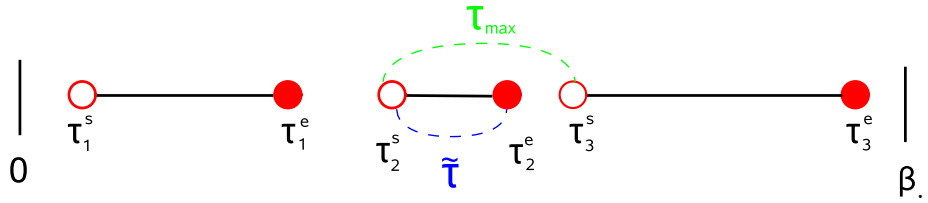

Figure 3.5: *Graphical representation of inserting a new segment in the collection of three segments.*

In the strong-coupling method, the pre-factor P_k contains two part: $1/k!$ and the trace over the local degree of freedom. The trace can also be calculated in the segment representation. Here, we only take insertion as example. Suppose the number of existing segments is k. The new segment (τ^s_{new} and τ^e_{new}) does not randomly

[7] It is the non-interacting part of full partition function in the weak-coupling method but the local part (normally, the local interaction U and chemical potential in the Hubbard model.) in the strong-coupling method.

[8] Explicitly to say, it is the trace over the local degrees of freedom.

locate in the range $[0, \beta)$ since there are k segments existing. Note in the single site DMFT with only density-density type interaction, the creation and annihilation operator can only occur in an alternative way. This means the new inserted segment can only be accepted if it locates at empty part in this collection. Practically, we first randomly choose a starting point in the range $[0, \beta)$, it is accepted when this point is not occupied by any existing segment, otherwise this insertion is rejected. The end point is determined by this starting point position and also the other k existing segments. The possible range for the end point of this new segment is τ_{max}, see Fig. 3.5. In this figure, suppose there are two segments existing before insertion, let us say τ_1^s, τ_1^e and τ_3^s, τ_3^e. Now we are going to insert the second segment. We first randomly select the starting point τ_2^s (In Fig. 3.5, it is a acceptable position.), the position for the end point can be anywhere in the range $(\tau_2^s, \tau_2^s + \tau_{max})$. Once τ_2^e is decided, the length of this segment $\tilde{\tau}$ is given as $\tau_2^e - \tau_2^s$. Then the ratio of this insertion is given as

$$ratio^W_{k\to k+1} = \frac{\beta\tau_{max}}{k+1} \times \left|\frac{\det(M_{k+1}^{-1})}{\det(M_k^{-1})}\right| \times e^{(\tilde{\tau}\mu - U\tau_{overlap})} \tag{3.45}$$

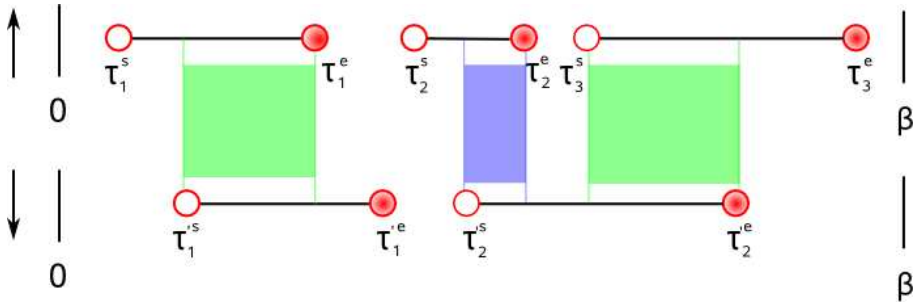

Figure 3.6: *In the interacting case, the overlap between the spin-up and spin-down segment represents the on-site Coulomb interaction.*

It is easily understood that the probability for the new start and end point are proportional to β and τ_{max}, respectively. The exponential function comes from the trace ratio between the new and old configuration, this can be calculated by the normal matrix production as we showed in the first chapter. The introduction of the segment representation now greatly simplifies this calculation by only considering τ_{max} and $\tilde{\tau}$. For the non-interacting Hubbard model, it only contains the chemical potential term. For the interacting case, one needs to consider two collections of segments, one for spin-up and one for spin-down. Since segment represents the occupied state, the overlap between these two collections just means that this part of state is occupied by spin-up and spin-down particles at the same time. In Hubbard model, it will give us the interaction U between them. This overlap is graphically shown as Fig. 3.6. The update ratio depends on the overlap change with respect to the new inserted segment. In our example, it is given as the blue part in Fig. 3.6.

The result for the removal segment and anti-segment move can be obtained in the same way. Tabular (3.1) shows the update ratio for the strong-coupling method in the interacting case. In the high temperature and strong coupling regime,

insert segment	$\frac{\mathcal{Z}_{k+1}}{\mathcal{Z}_k}\frac{\beta\tau_{max}}{k+1}e^{\tilde{\tau}\mu-U\tau_{overlap}}$
remove segment	$\frac{\mathcal{Z}_{k-1}}{\mathcal{Z}_k}\frac{k}{\beta\tau_{max}}e^{-\tilde{\tau}\mu+U\tau_{overlap}}$
insert anti-segment	$\frac{\mathcal{Z}_{k+1}}{\mathcal{Z}_k}\frac{\beta\tau_{max}}{k+1}e^{-\tilde{\tau}\mu+U\tau_{overlap}}$
remove anti-segment	$\frac{\mathcal{Z}_{k-1}}{\mathcal{Z}_k}\frac{k}{\beta\tau_{max}}e^{\tilde{\tau}\mu-U\tau_{overlap}}$

Table 3.1: *Detailed balance condition of strong coupling method in graphical representation.*

especially for the insulating state, one need to include the move of full and empty line since in these cases, the optimal perturbation order is relatively small and the zero dimensional M-matrix makes a great contribution to the sampling.

As for comparison, in the traditional Hirsch-Fye method, the configuration matrix has a dimension proportional to $5\beta U$, but $0.5\beta U$ in the weak-coupling method. In this strong-coupling method, it is lower than both of the above two methods. In figure 3.8, one can see that for the parameter $\beta t = 50$, $U/t = 3$, the optimal order is 32 in this strong-coupling method, but nearly 150 in Rubtsov's method and 1500 in Hirsch-Fye method. And with the increase of the interaction strength, the average perturbation order in the strong-coupling method becomes smaller. This means that the strong-coupling method is more suitable than the other methods for studying the strong interaction region. With respect to the temperature dependence, the strong-coupling method is the same as the weak-coupling method in the sense that with the decrease of temperature the average perturbation order k becomes larger, see Fig. 3.7.

3.3.3 Multi-Site Implementation

In most cases, the hybridization function cannot be diagonalized. One has to work with the matrix form of it. Eq. (3.33) is the equation we always use during the simulation. There are three basic Monte Carlo update steps:

1. Insertion of a pair of operators c_a and $c^\dagger_{a'}$ at random time τ_{new} and τ'_{new}. These two operators are randomly selected from N flavors. The two random time τ_{new} and τ'_{new} locate in the range $[0, \beta)$, therefore the update ratio for the operation of inserting a pair of time is

$$P_{k\to k+1} = \left(\frac{\beta N}{k+1}\right)^2 \frac{Tr_{new}}{Tr_{old}}\frac{D_{new}}{D_{old}} \tag{3.46}$$

2. Removal of a pair which is randomly selected from the existing k creation operators and k eliminating operators. The update ratio is

$$P_{k\to k-1} = \left(\frac{k}{\beta N}\right)^2 \frac{Tr_{old}}{Tr_{new}}\frac{D_{old}}{D_{new}} \tag{3.47}$$

3. At high temperature and strong interaction regime, the average perturbation order is very small. In this case it is hard to insert or remove one pair. The

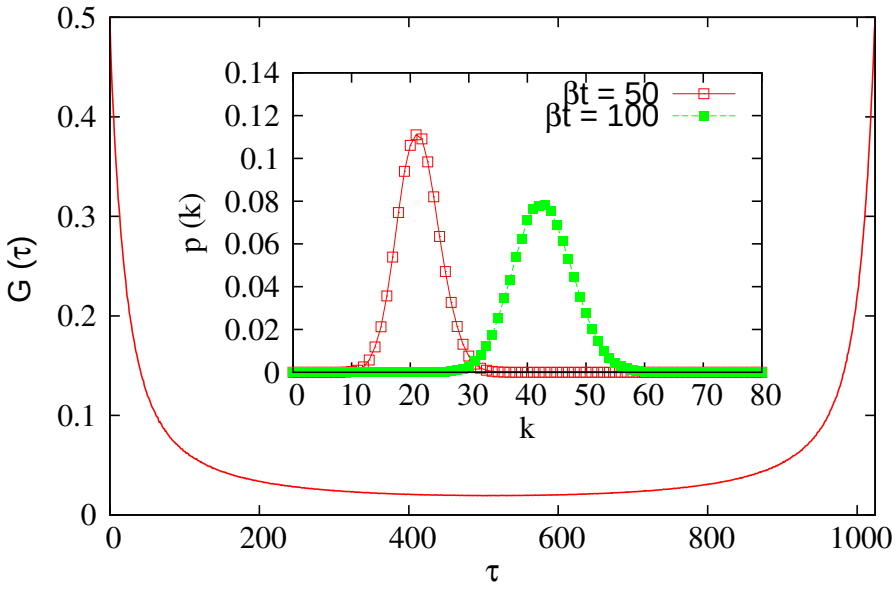

Figure 3.7: *Green's function in the non-interacting case, and the perturbation order is proportional to the inverse of temperature.*

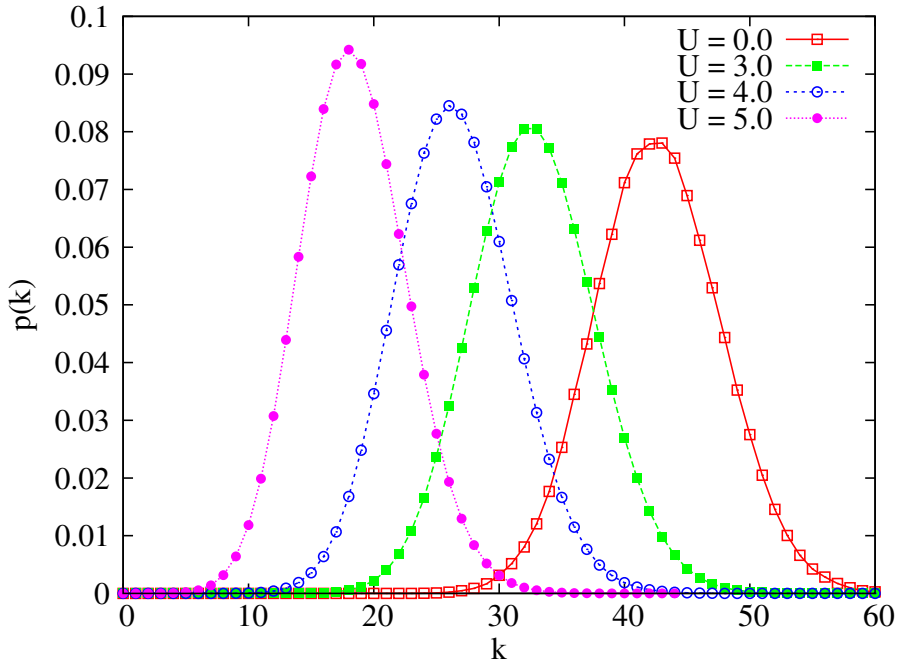

Figure 3.8: *Perturbation order of expansion at $\beta t = 50$ for different interaction strength, and the critical order decreases with the interaction.*

above two operations are quite inefficient. The alternative operation is to shift the end point of a selected pair. From the existing k annihilation operators, randomly select one and try to change the value of τ'. This new changed time will randomly locate at one of the N flavors at $[0, \beta)$. The resulting configuration has the same perturbation order k, but different determinant and trace. The update ratio for shifting the end point is

$$P_{shift} = \frac{Tr_{new}}{Tr_{old}} \frac{D_{new}}{D_{old}} \tag{3.48}$$

Here D_{new}/D_{old} is the ratio of the new and old determinant for the hybridization matrix. Tr_{new}/Tr_{old} is the ratio of the trace for the new and old configuration. In contrast, in the multi-Band implementation, we have a different update ratio. Take the insertion as example, since each flavor is decoupled we can only select the new creation and annihilation operator in the same flavor, so the update ratio is given as

$$P_{k\to k+1} = \left(\frac{\beta}{k_a+1}\right)^2 \frac{Tr_{new}}{Tr_{old}} \frac{D^a_{new}}{D^a_{old}} \tag{3.49}$$

Note this ratio only relates with the perturbation order in the specific flavor since the other flavor does not change during the current operation. For the same reason, the ratio of the total determinant reduces to that in this flavor, as well.

One can easily see that there are two kind of values which need to be evaluated in order to determine the update ratio. One is the for the trace, the other one is for the determinant. Let us first discuss the trace evaluation.

$$Trace = < T_\tau c_{a'_1}(\tau'_1) c^\dagger_{a_1}(\tau_1) \cdots c_{a'_k}(\tau'_k) c^\dagger_{a_k}(\tau_k) > \tag{3.50}$$

Time ordering operator moves the smallest time to the far right, in the end after the time ordering, the above equation might become

$$Trace = \frac{1}{\mathcal{Z}_{loc}} \int \mathcal{D}[c, c^\dagger] e^{-\int_0^\beta H_{loc}} [c_{a_{n_1}}(\tau'_{n_1}) c^\dagger_{a_{n_2}}(\tau_{n_2}) \cdots c_{a_{n_{2k-1}}}(\tau'_{a_{n_{2k-1}}}) c_{a_{n_{2k}}}(\tau_{n_{2k}})] \tag{3.51}$$

Here $\tau'_{n_1} > \tau_{n_2} > \cdots > \tau'_{n_{2k-1}} > \tau_{n_{2k}}$. Note this is only one possible configuration, the creation and annihilation operator do not necessary appear alternatively. Suppose we know all the eigenvalues and eigenstates of the local Hamiltonian[9]. We now use the eigenstates as basis to rewrite the above equation. $e^{-\int_0^\beta H_{loc}}$ becomes a diagonal matrix with the element $e^{-\beta E_m}$ where $m = 1, \cdots, N_m$[10]. Each operator $\mathcal{O}(\tau)$ has the form of $\sum_{m_1,m_2} e^{E_{m_1}\tau} \bar{\mathcal{O}} e^{-E_{m_2}\tau}$ in Heisenberg picture, here operator $\mathcal{O}$ has been rewritten as matrix $\bar{\mathcal{O}}$ in the eigenbasis. Then the evaluation of the trace can be done by multiplying all the matrix one by one.

$$Trace = \sum_{\{m\}} e^{-(\beta-\tau_{n_1})E_{m_1}} \left(c_{a_{n_1}}\right)_{m_1 m_2} e^{-(\tau_{n_1}-\tau_{n_2})E_{m_2}} \cdots \left(c_{a_{n_{2k-1}}}\right)_{m_{2k-1} m_{2k}} e^{-\tau_{n_{2k}} E_{m_{2k}}} \tag{3.52}$$

[9] This is straightforward but tedious calculation, especially for the larger cluster, one can use a simple ED code to do this job.

[10] N_m is the total number of eigenvalues, which is given as 4^N.

Normally, the above matrix production is quite time consuming since each matrix has dimension $N_m \times N_m$. N_m greatly increases with the increase of site numbers in the cluster. Therefore the greatly increased Hilbert space stops the investigation of larger cluster in this method. One has to simplify the above implementation, which is possible sometime. Here we list three possible ways:

eigenValues and eigenStates			
$N=0, S=0$	$S_z=0$	$\|0,0\rangle$	0
$N=1, S=\frac{1}{2}$	$S_z=\frac{1}{2}$	$\frac{1}{\sqrt{2}}(\|\uparrow,0\rangle+\|0,\uparrow\rangle)$	$-\mu-t$
		$\frac{1}{\sqrt{2}}(\|\uparrow,0\rangle-\|0,\uparrow\rangle)$	$-\mu+t$
	$S_z=-\frac{1}{2}$	$\frac{1}{\sqrt{2}}(\|\downarrow,0\rangle+\|0,\downarrow\rangle)$	$-\mu-t$
		$\frac{1}{\sqrt{2}}(\|\downarrow,0\rangle-\|0,\downarrow\rangle)$	$-\mu+t$
$N=2, S=1$	$S_z=1$	$\|\uparrow,\uparrow\rangle$	-2μ
	$S_z=0$	$-\frac{1}{\sqrt{2}}(\|\uparrow,\downarrow\rangle-\|\downarrow,\uparrow\rangle)$	-2μ
		$-\frac{1}{\sqrt{2}}(\|\uparrow\downarrow,0\rangle-\|0,\uparrow\downarrow\rangle)$	$-2\mu+U$
		$\frac{1}{c_1'}[(\|\uparrow,\downarrow\rangle+\|\downarrow,\uparrow\rangle)-c_1(\|\uparrow\downarrow,0\rangle+\|0,\uparrow\downarrow\rangle)]$	$\frac{U-4\mu+\sqrt{U^2+16t^2}}{2}$
		$\frac{1}{c_2'}[(\|\uparrow,\downarrow\rangle+\|\downarrow,\uparrow\rangle)-c_2(\|\uparrow\downarrow,0\rangle+\|0,\uparrow\downarrow\rangle)]$	$\frac{U-4\mu-\sqrt{U^2+16t^2}}{2}$
	$S_z=-1$	$\|\downarrow,\downarrow\rangle$	-2μ
$N=3, S=\frac{1}{2}$	$S_z=\frac{1}{2}$	$\frac{1}{\sqrt{2}}(\|\uparrow\downarrow,\uparrow\rangle+\|\uparrow,\uparrow\downarrow\rangle)$	$U-3\mu-t$
		$\frac{1}{\sqrt{2}}(\|\uparrow\downarrow,\uparrow\rangle-\|\uparrow,\uparrow\downarrow\rangle)$	$U-\mu+t$
	$S_z=-\frac{1}{2}$	$\frac{1}{\sqrt{2}}(\|\uparrow\downarrow,\downarrow\rangle+\|\downarrow,\uparrow\downarrow\rangle)$	$U-3\mu-t$
		$\frac{1}{\sqrt{2}}(\|\uparrow\downarrow,\downarrow\rangle-\|\downarrow,\uparrow\downarrow\rangle)$	$U-3\mu+t$
$N=4, S=0$	$S_z=0$	$\|\uparrow\downarrow,\uparrow\downarrow\rangle$	$2U-4\mu$

Table 3.2: *The eigenstates and eigenvalues of the local Hamiltonian for a two site Hubbard cluster.*

---

1. Sparse matrix operation. Since most of the elements in the operator matrix are zero, much computational time are spent on the multiplication with zero in the matrix production. The full matrix production can be replaced by the sparse matrix production, where we only store the nonzero elements and its corresponding position in the full matrix.

2. Work with the good quantum number. For the Hubbard model we are studying, the total number of particles N_f, the total spin S and its z-component S_z which are normally the good quantum numbers. The resulting Hilbert space of the local Hamiltonian can be grouped by these quantum numbers. The Hilbert space is block diagonal, each block can be identically labeled by those quantum numbers.

3. Storing the time evolution. In each update step, we have to calculate the trace for each new configuration, no matter whether it is accepted by the Monte Carlo random walk or not. And normally most of the attempts are

rejected. Therefore it is very economical to save the time evolution matrix at each accepted update from both the left and right sides.

The analysis of good quantum numbers in the Hilbert space brings some inconvenience in the sense that each operator only can change the eigenstate from one block to another, which is known to us. For example,

$$c_a^\dagger |N_f, S, S_z\rangle = |N_f + 1, S \pm \frac{1}{2}, S_z + \sigma\rangle \tag{3.53}$$

Then in the matrix production, we can ignore the eigenvalue matrix first.By tracing each nonzero element in the first operator matrix we can know which one finally survives in the matrix production[11]. During this process, one has to remember its trajectory in each operator matrix. Once we find the surviving element(or elements), the corresponding eigenvalues at each stop on the trajectory should be multiplied which finally gives the matrix product results.

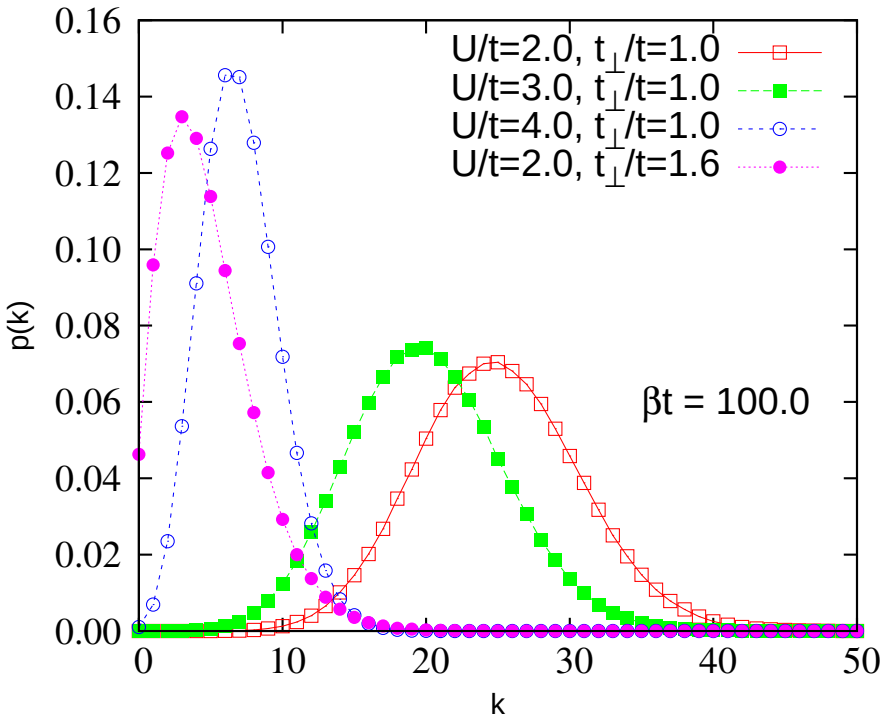

Figure 3.9: *Histogram of the two Bethe-plane Hubbard model at temperature* $\beta t = 100$ *and various interaction.*

Let us take a two site cluster as example in order to illustrate the implementation of the above idea. Table (3.2) shows the eigenvalues and eigenstates of the local Hamiltonian. Where $c_1 = -(U + \sqrt{U^2 + 16t^2})/4t$, $c_2 = -(U - \sqrt{U^2 + 16t^2})/4t$, and $c_1' = \sqrt{2 + 2c_1^2}$, $c_2' = \sqrt{2 + 2c_2^2}$. There are eight different operators $c_{1\uparrow}^\dagger$, $c_{1\uparrow}$, $c_{1\downarrow}^\dagger$,

[11] This process is accelerated by considering the good quantum numbers as we discussed

$c_{1\downarrow}$, $c^{\dagger}_{2\uparrow}$, $c_{2\uparrow}$, $c^{\dagger}_{2\downarrow}$, $c_{2\downarrow}$. Let us suppose that we are going to calculate the trace for perturbation order $k = 2$ with the configuration: $c^{\dagger}_{1\uparrow}(\tau_1)c_{2\downarrow}(\tau_2)c_{1\uparrow}(\tau_3)c^{\dagger}_{2\downarrow}(\tau_4)$. This example is a possible and acceptable configuration for the two site cluster problem. Imaginary time has been ordered, $\tau_1 > \tau_2 > \tau_3 > \tau_4$. By using the above looking-up method between different block states, we can finally know that the following block states contribute to the trace.

$$|N = 1, S = \frac{1}{2}, S_z = \frac{1}{2}\rangle, \qquad |N = 2, S = 1, S_z = 1\rangle$$
$$|N = 2, S = 1, S_z = 0\rangle, \qquad |N = 3, S = \frac{1}{2}, S_z = \frac{1}{2}\rangle$$

The trace calculation only need to be performed during these states instead of the whole Hilbert spaces, which greatly reduces the computational burden.

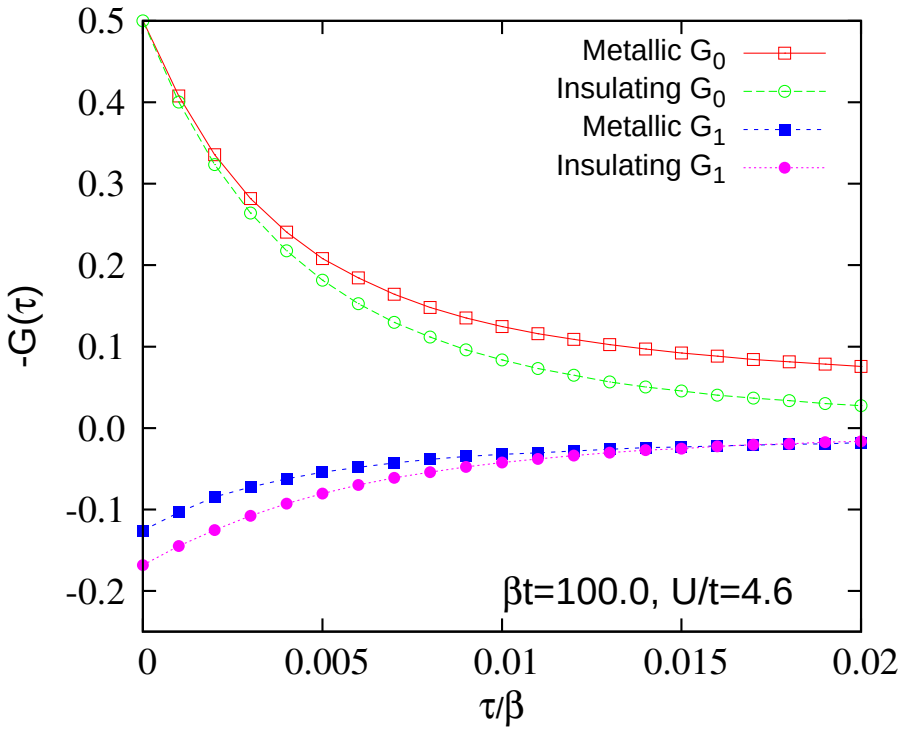

Figure 3.10: *The on-site Green's function and the Green's function for the propagation between two planes.*

Now, we present some results from the calculation of a two Bethe-plane Hubbard model, whose local Hamiltonian has a similar form as the two-site Hubbard cluster. One only need to replace t with $t_{\perp}$, which is the inter-plane hopping amplitude and the intra-plane hopping is still given as t. In this example, we used the Multi-Band implementation, some results are listed below.

Fig. 3.9 shows the distribution of the perturbation order as a function of on-site interaction and the inter-plane coupling. The first three curves show that for the same inter-plane coupling, with the increasing of on-site Coulomb interaction,

the average perturbation order k becomes smaller. The same thing happens to the inter-plane coupling. With the increasing of the inter-plane coupling, the average perturbation order becomes smaller. Fig. 3.10 shows the intra-plane Green's function G_0 which is just the on-site one in this model[12], and the inter-plane Green's function G_1. The parameters are $\beta t = 100$ and $U/t = 4.6$. For this parameter, the system is in the coexistence region of the Metal-Insulator transition. Thus we have two coexisting solutions for G_0 and G_1. Here, we only plot a narrow range for $\tau/\beta \in [0, 0.02]$. G_0 drops from 0.5 to 0 rapidly, which is difficult to examine in the Hirsch-Fye method since a large number of time slices are needed. CTQMC does not introduce any time discretization, therefore the quick dropping behavior is easily obtained in CTQMC. In the Hirsch-Fye method, $L = 256$ is a large time slice number for current PC. Even with this number, in the range of [0, 0.02], there are only 5 points existing which are not sufficient for smoothly describing the quick dropping behavior of G_0.

[12]Each plane has been mapped to an impurity.

Chapter 4

Dual fermion approach – long range correlation

Although various cluster extensions of dynamical mean field method are constructed from different physics considerations, they are all the natural generations of single site DMFT. Cellular DMFT is the cluster formulation of DMFT; Dynamical Cluster Approximation is the momentum cluster extention. Variational Cluster Approximation uses the variational principle to determine the real system grand potential from a reference cluster calculation based on the self-energy functional theory. The limitation of these methods is easy to see, only finite sites cluster are accessible under the restriction of computational burden. Within the finite size cluster, on the one hand it is not easy to reproduce all the symmetry of the original lattice, on the other hand it misses the long range correlation.

Recently, some efforts have been made to take the spatial fluctuations into account in different ways [Toschi *et al.* (2007); Rubtsov *et al.* (2008); Kusunose (2007); Tokar and Monnier (2007); Slezak *et al.* (2006)]. These methods construct the non-local contribution of DMFT from the local two-particle vertex. In the self energy function, only certain diagrams are included, which makes them only approximately include the non-local corrections. Various cluster extentions of DMFT try to exactly incorporate the non-locality within a small size reference system. References 13-17 considered the momentum dependence in the self energy and vertex function in an approximate way. In contrast to the cluster DMFT, the long range information is naturally included in these methods from the. Our calculations show that the such approximate momentum dependent self energy and vertex function are normally sufficient to generate reliable results compared to numerically expensive calculations.

In this chapter, we will discuss two of these methods, the dual fermion method (DF) and the dynamical vertex approximation (DΓA). The one particle Green's function and the two particle susceptibility are calculated to study the non-local corrections to the single site DMFT. The discussion of the difference between these two methods is also given.

4.1 Decoupling and dual fermion

Here, We use the general one-band Hubbard model as example

$$H = \sum_{k,\sigma} \epsilon_{k,\sigma} c^{\dagger}_{k\sigma} c_{k\sigma} + U \sum_{i} n_{i\uparrow} n_{i\downarrow} \tag{4.1}$$

$c^{\dagger}_{k\sigma}(c_{k\sigma})$ creates(annihilates) an electron with spin-σ and momentum k. The dispersion relation is given as $\epsilon_k = -2t(\cos k_x + \cos k_y)$. The corresponding action is:

$$S[c*, c] = \sum_{\nu,k,\sigma} (\epsilon_k - \mu - i\nu) c^{*}_{k\nu\sigma} c_{k\nu\sigma} - U \sum_{i} \int_0^{\beta} d\tau n_{i\uparrow}(\tau) n_{i\downarrow}(\tau) \tag{4.2}$$

Single site DMFT simplifies such lattice action into an effective action which only has one interacting site while the others serve as non-interacting bath. Cluster DMFT consider a few interacting sites and takes the remaining lattice degrees of freedom as bath. The non-interacting remaining degree of freedom can be integrated out exactly, which yields an effective action of the impurity which couples to the bath described by an effective hybridization function. Let's take the single site DMFT action as example.

$$S_{imp} = \sum_{\nu,\sigma} (\Delta_\nu - \mu - i\nu) c^{*}_{k\nu\sigma} c_{k\nu\sigma} - U \int_0^{\beta} d\tau n_{\uparrow}(\tau) n_{\downarrow}(\tau) \tag{4.3}$$

We can relate the lattice action with the DMFT action by adding and subtracting a hybridization function.

$$S[c^*, c] = \sum_{i} S^{i}_{imp} - \sum_{\nu,k,\sigma} (\Delta_\nu - \epsilon_k) c^{*}_{k\nu\sigma} c_{k\nu\sigma} \tag{4.4}$$

The first term describes a collection of lattice sites which are independent of the others. Therefore they can be viewed as impurities. It naturally contains the local information of the system! The last term describes the correlation between different lattice sites which are non-local. The general idea of the dual fermion method is to change this term to the coupling to an auxiliary field $f(f^{\dagger})$. By applying the Gaussian identity to this bilinear term, the lattice action becomes

$$S[c^*, c; f^*, f] = \sum_{i} S^{i}_{imp} + \sum_{k,\nu,\sigma} [g_\nu^{-1} (c^{*}_{k\nu\sigma} f_{k\nu\sigma} + h.c.) + g_\nu^{-2} (\Delta_\nu - \epsilon_k)^{-1} f^{*}_{k\nu\sigma} f_{k\nu\sigma}] \tag{4.5}$$

The partition function of lattice fermion now can be written as

$$\mathcal{Z} = \mathcal{Z}_f \int e^{-S[c,c^*;f,f^*]} \mathcal{D}[c, c^*; f, f^*] \tag{4.6}$$

where $\mathcal{Z}_f = \prod_{k\nu} g_\nu^2 (\Delta_\nu - \epsilon_k)$. We obtained Eq. (4.5) from the original lattice action Eq. (4.4) by using the Gaussian identity, which means there's on any approximation introduced. The equivalence of Eq. (4.4) and Eq. (4.5) allows us to setup an exact

relation between the DF Green's function and the lattice Green'f function. By differentiating these two actions over the kinetic term, we have

$$\begin{aligned}\frac{\partial}{\partial\epsilon_k}\mathcal{Z}[c,c^*] &= \frac{\partial}{\partial\epsilon_k}\mathcal{Z}[c,c^*;f,f^*] \\ &= (\frac{\partial}{\partial\epsilon_k}\mathcal{Z}_f)\int e^{-S[c,c^*;f,f^*]}\mathcal{D}[c,c^*;f,f^*] \\ &\quad -\mathcal{Z}_f\int e^{-S[c,c^*;f,f^*]}\frac{\partial}{\partial\epsilon_k}S[c,c^*;f,f^*]\mathcal{D}[c,c^*;f,f^*] \end{aligned} \tag{4.7}$$

The derivative of the original action over ϵ_k is nothing but the lattice Green's function

$$\frac{\partial}{\partial_{\epsilon_k}}\mathcal{Z}[c,c^*] = -\int \mathcal{D}[c,c^*]e^{-S[c,c^*]}c^*_{k\nu\sigma}c_{k\nu\sigma} = -\mathcal{Z}[c,c^*]G_{\nu,k} \tag{4.8}$$

Similarly, the derivative of the new action can be obtained as

$$-\mathcal{Z}[c,c^*;f,f^*](\Delta_\nu-\epsilon_k)^{-1} - \mathcal{Z}_f\int \mathcal{D}[c,c^*;f,f^*]e^{-S[c,c^*;f,f^*]}g_\nu^{-2}(\Delta_\nu-\epsilon_k)^{-2}f^*_{k\nu\sigma}f_{k\nu\sigma} \tag{4.9}$$

The second term defines the dual fermion Green's function $G^d_{\nu,k} = -\langle f_{\nu,k}f^\dagger_{\nu,k}\rangle$. The above two equations form an exact relation between the Green's function of lattice electrons and dual fermions.

$$G_{\nu,k} = g_\nu^{-2}(\Delta_\nu-\epsilon_k)^{-2}G^d_{\nu,k} + (\Delta_\nu-\epsilon_k)^{-1} \tag{4.10}$$

The exact relation of the lattice fermion $G_{\nu,k}$ and the dual fermion $G^d_{\nu,k}$ allows us to determine the lattice Green's function from the latter. Hence the solving of an interacting many body problem now turns to be the determination of the dual propagator $G^d_{\nu,k}$.

The dual fermion Green's function $G^d_{\nu,k}$ is determined by integrating Eq. (4.5) over c^*, c which yields a Taylor expansion series in terms of f^* and f. The Grassmann integral makes sure that f^* and f only appear in pairs, associated with the lattice fermion n-particle vertex obtained from the single site DMFT calculation. The action corresponding to site ' i ' is

$$S_{site}[c_i,c_i^*,f_i,f_i^*] = S_{imp}[c_i,c_i^*] + \sum_\nu g_\nu^{-1}(c^*_{i\nu}f_{i\nu} + f^*_{i\nu}f_{i\nu}) \tag{4.11}$$

The summation is only over fermionic frequency since each lattice sites has been decoupled now. Expanding the last term $S^i_{coup} = \sum_\nu(c^*_{i\nu}f_{i\nu} + f^*_{i\nu}c_{i\nu})$, we obtain a Taylors series

$$\int e^{-S_{site}}\mathcal{D}[c,c^*] = \int e^{-S_{imp}}\mathcal{D}[c,c^*][1 - S_{coup} + \frac{1}{2!}S^2_{coup} + \cdots] \tag{4.12}$$

In the integral over $[c,c^*]$, only pairs of c and c^* survives. The first two corrections come from the second and the fourth order term which have the following form

$$\begin{aligned}\int e_{-S_{site}}\mathcal{D}[c_i,c_i^*] &= \int e^{-S_{imp}}[1 + \sum_\nu g_\nu^{-2}c_ic_i^*f_i^*f_i + \sum_{1234} g_\nu^{-4}c_1c_2^*c_3c_4^*f_1^*f_2f_3^*f_4 + \cdots] \\ &= \mathcal{Z}_{imp}[1 + \sum_\nu g_\nu^{-1}f_i^*f_i + g_\nu^{-4}G_{1234}f_1^*f_2f_3^*f_4 + \cdots] \\ &= \mathcal{Z}_{imp}e^{\sum_\nu g_\nu^{-1}f_\nu^*f_\nu - V[f_i,f_i^*]} \end{aligned} \tag{4.13}$$

V is the effective interaction of dual fermion. Now the total action of the dual fermion can be written as the following form

$$\mathcal{Z} = \mathcal{Z}_{imp} \int \mathcal{D}[f, f^*] e^{-\sum_{k\nu\sigma} f^*_{k\nu\sigma}[g_\nu^{-2}(\Delta_\nu - \epsilon_k)^{-1} + g_\nu^{-1}] f_{k\nu\sigma} + V[f, f^*]} \tag{4.14}$$

The bare dual Green's function is then read out from the one particle part of this action as

$$G_0^{d,-1} = -g_\nu^{-1}[(\Delta_\nu - \epsilon_k)^{-1} + g_\nu] g_\nu^{-1} \tag{4.15}$$

Up to now, all the above derivations do not rely on any approximation! To calculate the dual fermion self-energy, we are facing two problems: (1). The determination of the effective interaction V. As we can see from the above equation, V contains all the vertex correction terms up to infinite order. It also contains all sorts of combinations of different order vertices. Normally, it is impossible to be determined precisely. (2). Determination of the dual fermion self energy from the effective interaction. Since the dual fermion interacts with each other through V, this many-body interacting problem is as difficult as the original lattice problem. It seems we didn't simplify our original problem but introduced an even more complicated interacting problem. The advantage of all the above transformations is not easy to see until now. All the secrets of the transformation is that we have tranformed an strongly interacting problem to an effectively weak-coupling problem, which will become clear later on.

Let us now focus on the solution of the dual fermion Green's function in the simplest way. Concerning the first problem listed above, in the dual fermion method we only determine the effective interaction in the simplest way. The first term in the effective interaction is the two particle DMFT vertex. Let us only consider its contribution and suppose that the contribution from all the higher vertex terms are small. Then the effective interaction is given as $-1/4\gamma^4 f_1^* f_2 f_3^* f_4$ where γ^4 is the two particle vertex from the DMFT calculation. Even if we only consider the two particle vertex, the problem is still not easy to solve since there are still lots of feynman diagrams in the expansion over the two particle vertex. The expansion includes all the combinations of this two particle vertex with the one particle propagator. This is the difficulty stated in the second problem. Here we further adapt another approximation, we only consider the first two order diagrams in the expansion over the two particle vertex. One can see, here we introduced two approximations. Firstly, we only consider the two particle vertex contribution in the effective potential. Secondly, in the expansion of the effective interaction, we only consider the first order diagrams. This is obviously the simplest approximation.

Rubtsov [Rubtsov *et al.* (2008)] calculated 2-dimensional Hubbard model in the dual fermion method, the above approximation gave enough good results compared with the direct lattice monte carlo calculation. The higher order expansion terms only improved the resolution. Although there is no direct proof that the expansion of the dual fermion field is an effectively weak coupling theory, from the numerical calculation we can believe that only the first two expansion terms which only depend on the two particle DMFT vertex function are sufficient. In the following context, we will focus on the non-local correction from the second order term.

4.2 Perturbation theory of dual fermion Green's function

The exact relation between the Green's function of lattice fermion and dual fermion gives us another way to determine the lattice properties. This problem now becomes looking for the Green's function of dual fermion. This can be achieved by the normal perturbation method, the only difference with the usual diagram expansion is that the expansion is in the dual fermion space. Here my calculation is totally based on the book [Abrikosov *et al.* (1963)] by using a fully symmetric interaction.

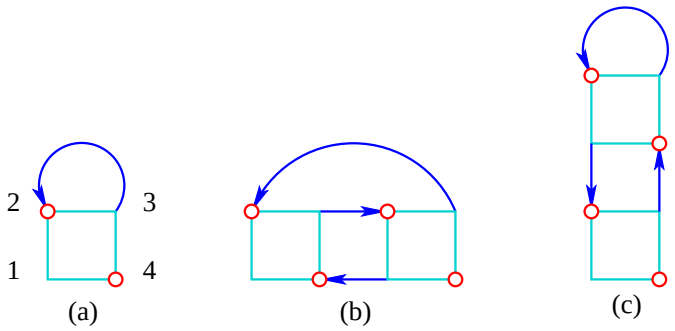

Figure 4.1: *(a). first order self energy constructed by local two-particle vertex function* $\gamma(i\nu_1, i\nu_2; i\nu_3, i\nu_4)$*. In the following part, such vertex will be written as a function of independent two fermionic* ν*,* ν' *and one bosonic frequency* ω*. (b) and (c) are the connected diagram in the second order and the contribution from (c) is zero in DMFT. Here, the blue line is the dual fermion one particle propagator* G_0^f *here. The box represents the two particle vertex.*

Known from the Luttinger-Ward functional [Georges *et al.* (1996)] at infinite dimension, (c) diagram in Fig. 4.1 contributes nothing to the self energy. Although (a) diagram survives in large coordinate limit, its contributes nothing, either. The reason is that this diagram exactly corresponds to the self consistency condition in DMFT. This can be shown as

$$\sum_k G_0^d(k) = 0 \tag{4.16}$$

To prove this relation, it's better to start from the self consistency condition $g_\nu = \sum_k \frac{1}{g_\nu^{-1} + \Delta_\nu - \epsilon_k}$. This equation can be easily changed to the following form which is zero

$$\sum_k \frac{1}{g_\nu + (\Delta_\nu - \epsilon_k)^{-1}} = 0 \tag{4.17}$$

This is the same as Eq. (4.16). DMFT self consistency condition ensures that the first self energy diagram contributes nothing. Note we actually consider this diagram in the full self-consistent calculation, since starting from the second loop this diagram has non-zero contribution.

The first non-local contribution is from the (b) diagram in Fig. 4.1. In the work of Rubtsov [Rubtsov *et al.* (2008)] and Hafermann [Hafermann *et al.* (2007)], they took this diagram as the main contribution to non-locality of DMFT. It was shown that the calculation with the first two order diagrams generated results which is in good agreement with the higher order diagrams calculation. After explicitly writing down the momentum and frequency indices, the self energy diagram based on the two particle vertex looks like

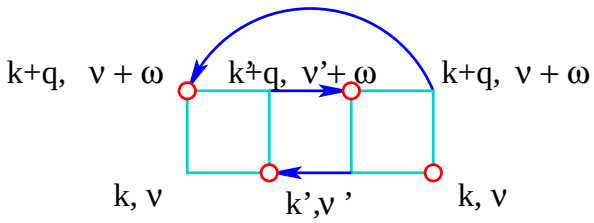

Figure 4.2: *The first non-local contribution to the dual fermion self energy. For each vertex, the momentum and frequency conservation law are satisfied.*

The corresponding self-energy is

$$\Sigma^{(2)}_{\sigma_1}(k) = -\frac{1}{2}\frac{T^2}{(N^d)^2}\sum_{\sigma_2\sigma_3\sigma_4}\sum_{k',q} G^d_{\sigma_2}(k+q)G^d_{\sigma_3}(k')G^d_{\sigma_4}(k'+q) \\ \gamma(\nu,\nu+\omega;\nu'+\omega,\nu')\gamma(\nu+\omega,\nu;\nu',\nu'+\omega) \tag{4.18}$$

Here space-time notation is used, $k = (\vec{k},\nu)$, $q = (\vec{q},\omega)$. Fermion Matsubara frequency $\nu_n = (2n+1)\pi/\beta$ and ω is the bosonic frequency, given as $\omega_m = 2m\pi/\beta$. The above equation has included the conservation law of momentum, frequency. Take into account all possible spin configurations, the sum over spin index can be expanded to the following equation

$$\Sigma^{(2)}_{\uparrow}(k) = -\frac{1}{2}\frac{T^2}{(N^d)^2}\sum_{k',q} G^d(k+q)G^d(k')G^d(k'+q)\times \\ [\gamma^{\uparrow\uparrow\uparrow\uparrow}_{\omega}(\nu,\nu')\gamma^{\uparrow\uparrow\uparrow\uparrow}_{\omega}(\nu',\nu) + \gamma^{\uparrow\uparrow\downarrow\downarrow}_{\omega}(\nu,\nu')\gamma^{\downarrow\downarrow\uparrow\uparrow}_{\omega}(\nu',\nu) + \gamma^{\uparrow\downarrow\downarrow\uparrow}_{\omega}(\nu,\nu')\gamma^{\uparrow\downarrow\downarrow\uparrow}_{\omega}(\nu',\nu)] \tag{4.19}$$

Here the paramagnetic property $G_\uparrow = G_\downarrow$ has been used in the last step.

Similarly the expression for diagram (a) in Fig. (4.1) is given as

$$\Sigma^{(1)}_{\sigma}(k) = -\frac{T}{N^d}\sum_{\sigma',k'} G^d_{\sigma'}(k')\gamma_{\sigma\sigma'}(\nu,\nu';\nu',\nu') \tag{4.20}$$

As we discussed, this diagram has no contribution in the sense that the sum over momentum for G^f_0 is zero. But in a full self-consistent calculation, the dressed dual fermion Green's function G^f does not satisfied this condition. Hence from the second iteration, this diagram gives non-zero contribution.

Together with the bare dual fermion Green's function $G_0^d(k) = -g_\nu^2/[(\Delta_\nu - \epsilon_k)^{-1} + g_\nu]$, the new Green's function can be derived from the Dyson equation

$$[G^d(k)]^{-1} = [G_0^d(k)]^{-1} - \Sigma^d(k) \tag{4.21}$$

where $\Sigma = \Sigma^{(1)} + \Sigma^{(2)}$. The dressed dual Green's function will be put into the self-energy calculation again to yield a stationary point with respect to the current vertex function $\gamma^{(4)}$ and DMFT Green's function $g(\nu)$ which are not changed. To find the global converged solution within the current method, one has to perform a calculation where the DMFT Green's function and vertex function are also determined self-consistently. Therefore, after the convergence of the dual fermion Green's function calculation, we also need to recalculate the DMFT vertex and Green's function.

In order to perform the new DMFT loop, we need to know the new hybridization function. It is simply done by setting the local full dual Green's function to be zero, together with the condition that the old hybridization function makes the bare local dual fermion to be zero, we obtain a set of equations

$$\frac{1}{N}\sum_k [G_{\nu,k} - (\Delta_\nu - \epsilon_k)^{-1}] g_\nu^2 (\Delta_\nu^{New} - \epsilon_k)^2 = 0 \tag{4.22a}$$

$$\frac{1}{N}\sum_k [G^0_{\nu,k} - (\Delta_\nu - \epsilon_k)^{-1}] g_\nu^2 (\Delta_\nu^{Old} - \epsilon_k)^2 = 0 \tag{4.22b}$$

Which are equivalent to

$$\Delta_\nu^{New} - \Delta_\nu^{Old} \approx \frac{1}{N}\sum_k (G_{\nu,k} - G^0_{\nu,k})(\Delta_\nu^{Old} - \epsilon_k)^2 \tag{4.23}$$

This equation gives us the relation between the new and old hybridization function.

$$\Delta_\nu^{New} = \Delta_\nu^{Old} + g_\nu^2 G^d_{loc} \tag{4.24}$$

4.2.1 One particle properties

The floating chart of the whole calculation is

1. Initially set Δ_ν, prepare for DMFT calculation.
2. Determine the converged single-site DMFT Green's function g_ν from the hybridization function Δ_ν. The self-consistency condition makes sure that the first diagram of dual fermion self-energy is very small.
3. Run the DMFT program one loop again to calculate the two-particle Green's function and corresponding γ-function. The method for determining the γ-function is implemented for both strong and weak-coupling CT-QMC in the next section of this paper.
4. Start an inner loop calculation to determine the dual fermion Green's function, in the end the lattice Green's function.

(a) From Eq. (4.18) and Eq. (4.20), together with the Dyson equation (4.21) to calculate the self-energy of dual fermions.

(b) Repeating Eq. (4.18) to Eq. (4.21) until one obtains the converged dual fermion Green's function.

(c) The lattice Green's function is given by Eq. (4.10) from dual fermion Green's function.

5. Fourier transform the momentum lattice Green's function into real space, and from the on-site component G_{ii} to determine a new hybridization function Δ_ν.

6. Go back to the Step 3. and iteratively perform the outer loop until the hybridization Δ_ν does not change again.

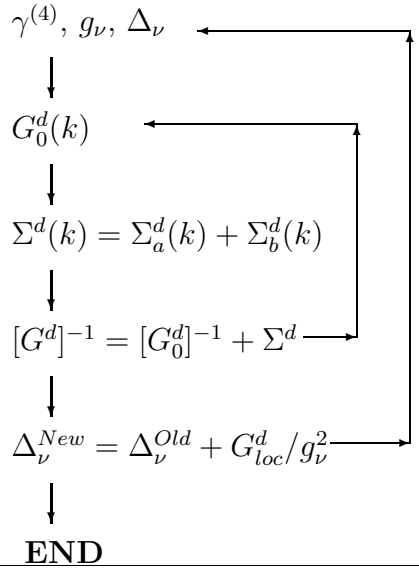

Figure 4.3: *The sketch of the DF loop. The most time consuming part is the outer loop execution. The inner loop normally is easy to get converged.*

The most time consuming part of this method is the DMFT calculation of the two particle Green's function, the dual fermion perturbation calculation easily converges. The two particle Green's function is a fully antisymmetric function. One does not need to calculate the two particle Green's function on all the frequency points within the cutoff in Matsubara space. Only on a few special points the two particle Green's function needs to be measured and the value on the other points are given by the values on those special points through the antisymmetric operation. Another useful hints is the momentum sum technique. In the dual fermion self energy calculation, we always have the convolution type of momentum summation which is very easy to be calculated by FFT (fast Fourier transform).

Fig. 4.4 shows the imaginary part of the one particle local Green's function calculated from the DMFT and DF method for various temperature at $U/t = 4.0$ (upper four) and $U/t = 8.0$ (lower four) on a 2D square lattice. For $U/t = 4.0$, DMFT and DF method generated the qualitatively same results. With the lowering of temperature, the correction from the non-local effect becomes bigger. At $U/t = 8.0$ case, the DF method generate very obvious corrections to the DMFT results. The behavior of the local Green's function is completely changed by the non-local correction, where DMFT result shows the metallic behavior while the DF results

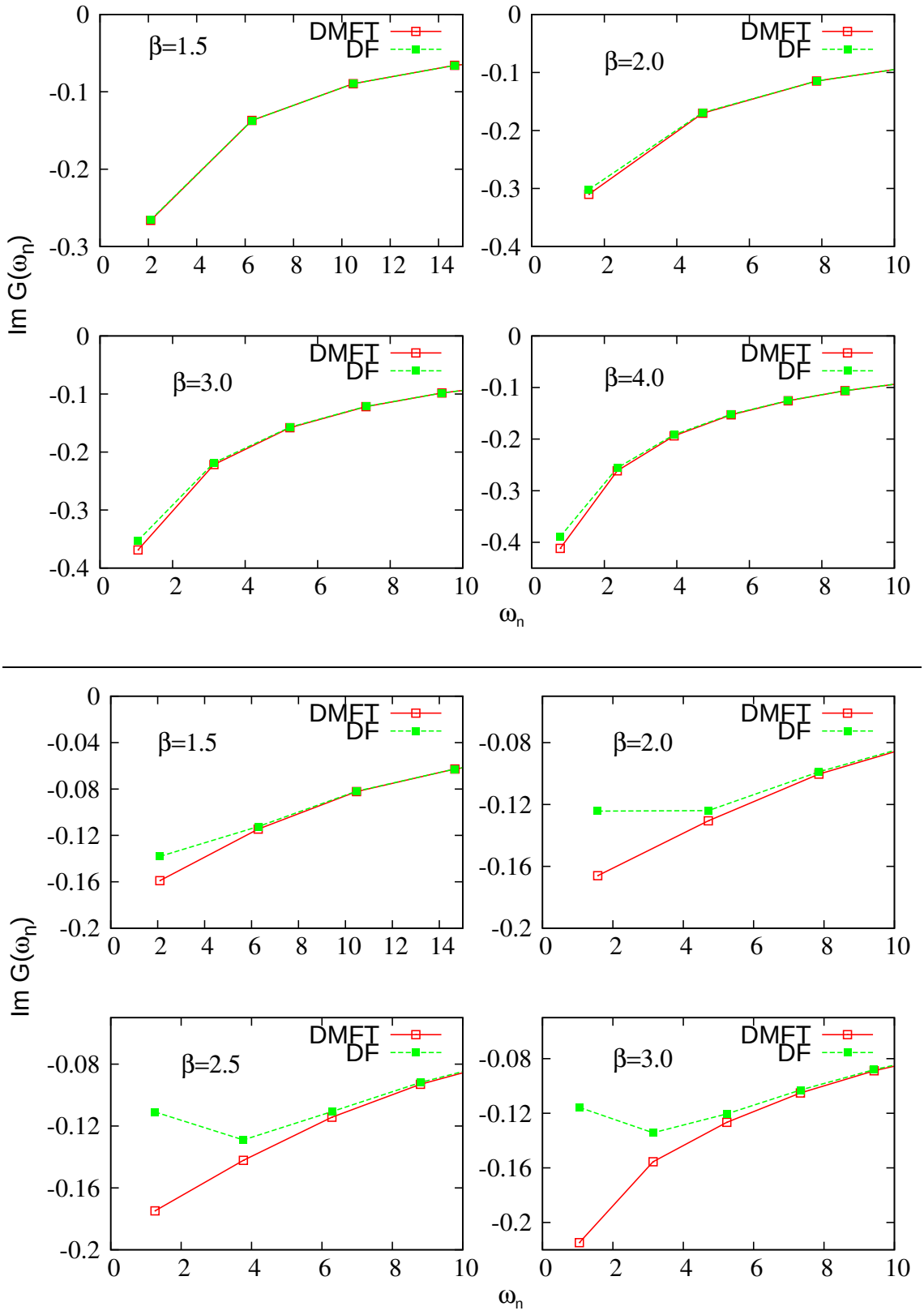

Figure 4.4: *The one particle Green's function from DMFT and DF calculations for the Hubbard Model on a 2D square lattice.* $U/t = 4.0$ *(the upper four figures) and* 8.0 *(the lower four figures) are fixed in each diagram.*

show the more insulating behavior. This correction opens the pseudogap in the density of states, which is supposed to come from the non-local spin fluctuation (also see the spin susceptibility results in the next section) effect. For the smaller

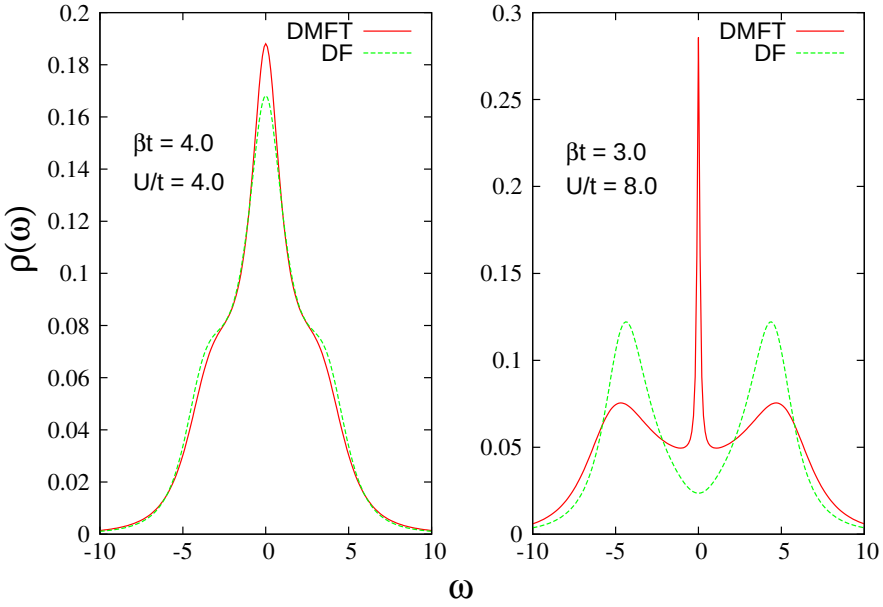

Figure 4.5: *Comparison of the DMFT and DF one particle density of state for the Hubbard model on a 2D square lattice. The left panel is for* $\beta t = 4.0$ *and* $U/t = 4.0$*. The right panel is for parameter* $\beta t = 3.0$ *and* $U/t = 8.0$*.*

interaction case, the DF density of state is compressed compared to that of DMFT but the pseudogap does not open. When the interaction is comparable with the bandwidth ($U = W = 8$), by including the non-local fluctuation the DF generated a density of state which shows the pseudogap behavior, while the DMFT result is still metallic.

4.3 Calculating susceptibility within dual approach

Note that diagram (a) in Fig. 4.1 gives only the local contribution. The first non-local correction in the DF method is from diagram (b). Momentum dependence comes into this theory through the bubble-like diagram between the two vertices which yields the momentum dependence of the DF vertex. The natural way to renormalize vertex is through the Bethe-Salpeter equation. Since the DMFT vertex is only a function of Matsubara frequency, the integral over internal momentum ensures that the full vertex only depends on the center of mass momentum q or $k' - k$. The Bethe-Salpeter equation in the particle-hole channel [Abrikosov *et al.* (1963); Nozieres (1964)] are shown in Fig. 4.6.

From the construction of the DF method, we know the interaction of the DF is coming from the two particle vertex of lattice fermion which is obtained through

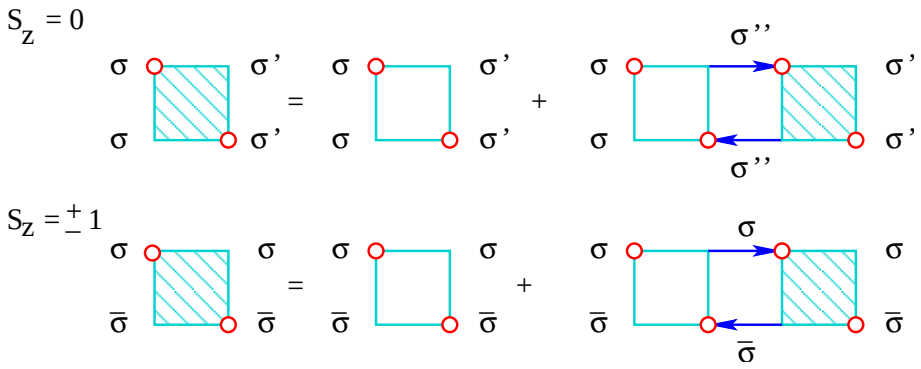

Figure 4.6: *$S_z = 0$ (ph0) and $S_z = \pm 1$ (ph1) particle-hole channels of the DF vertex, between vertices there are two full DF Green's function. The $S_z = \pm 1$ component is the triplet channel, while that for $S_z = 0$ can be either singlet or triplet.*

DMFT calculation. In the Bethe-Salpeter equation, it plays the role as the building-block. The corresponding Bethe-Saltpeter equation for these two channels are

$$\Gamma_q^{ph0,\sigma\sigma'}(k,k') = \gamma_q^{\sigma\sigma'}(k,k') - \frac{T}{N}\sum_{k''\sigma''} \gamma_q^{\sigma\sigma''}(k,k'')G^d(k'')G^d(k''+q)\Gamma_q^{ph0,\sigma''\sigma'}(k'',k') \tag{4.25a}$$

$$\Gamma_{k'-k}^{ph1,\sigma\bar{\sigma}}(k,k+q) = \gamma_{k'-k}^{\sigma\bar{\sigma}}(k,k+q) - \frac{T}{N}\sum_{q'} \gamma_{k'-k}^{\sigma\bar{\sigma}}(k,k+q') G^d(k+q')G^d(k'+q')\Gamma_{k'-k}^{ph1,\sigma\bar{\sigma}}(k+q',k+q) \tag{4.25b}$$

Here, the short hand notation of spin configuration is used. $\gamma^{\sigma\sigma'}$ represents $\gamma^{\sigma\sigma\sigma'\sigma'}$, while $\gamma^{\sigma\bar{\sigma}\bar{\sigma}\sigma}$ is denoted by $\gamma^{\sigma\bar{\sigma}}$ where $\bar{\sigma} = -\sigma$. $\Gamma^{ph0(ph1)}$ are the full vertices in the $S_z = 0$ and $S_z = \pm 1$ channel, respectively. G^d is the full DF Green's function obtained from the last section, which is kept unchanged in the calculation of the Bethe-Salpeter Equation. We solve the above equations directly in momentum space with the advantage that in this way we can calculate the susceptibility for any specific center of mass momentum q and it is convenient to use FFT for investigating a larger lattice. In the above Bethe-Salpeter equations, we used the general form of the vertex function γ which is the function of frequency and momentum, but in the DF method, γ is only a function of frequency, for example $\gamma_q^{\sigma\sigma'}(k,k') = \gamma_\omega^{\sigma\sigma'}(\nu,\nu')$. This leads to the fact that the full vertex calculated through the Bethe-Salpeter equation is a function of a single transfer momentum. The center of mass momentum in the $S_z = 0$ and $S_z = \pm 1$ channels are q and $k' - k$, respectively.

In Eq. (4.25) one has to sum up the internal spin in the $S_z = 0$ channel which is not present in $S_z = \pm 1$ channel. One can decouple the $S_z = 0$ channel into the charge and spin channels $\gamma_{c(s)} = \gamma^{\sigma\sigma} \pm \gamma^{\sigma\bar{\sigma}}$ which can be solved separately, and it turns out that the spin channel vertex function is exactly same as the that in $S_z = \pm 1$ channel, see e.g. P. Nozieres [Nozieres (1964)]. Such relation is true for the DMFT vertex, and was also verified for the momentum dependent vertex in the DF method [Brener *et al.* (2008)]. In our calculation, we solved the $S_z = 0$ channel by

decoupling it to the charge and spin components, while the $ph1$ channel is not used.

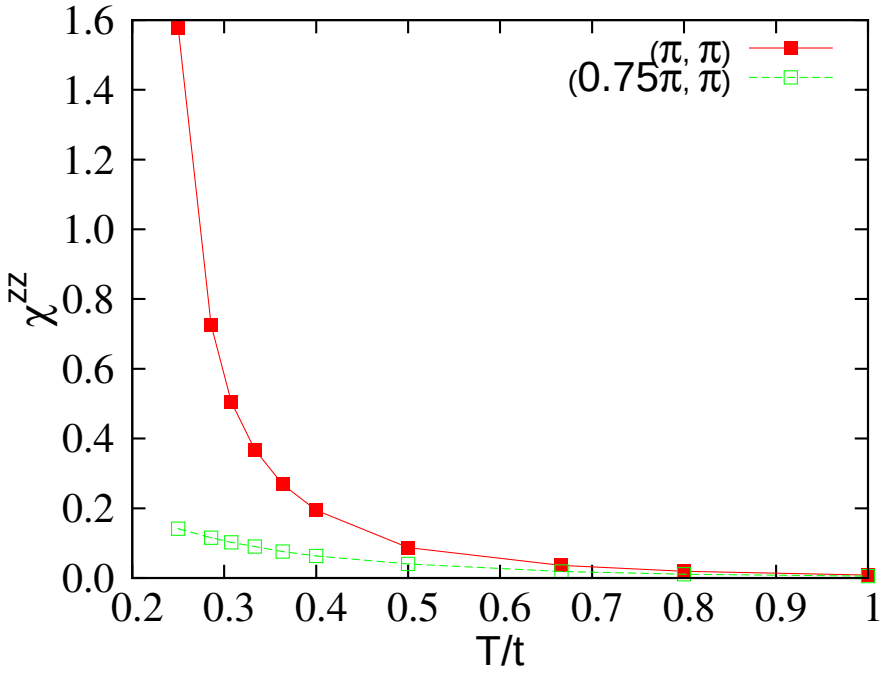

Figure 4.7: *Nontrivial part of z-component of dual spin susceptibility defined as* $\tilde{\chi}^{zz} = \chi^{zz} - \chi_0^{zz}$. *The interaction* U/t *is fixed as* 4. *With the increasing of inverse temperature, the susceptibility grows up dramatically. And divergence at the wave vector* (π, π).

Once the converged momentum dependent DF vertex is obtained, one can determine the corresponding DF susceptibility in the standard way by attaching four Green's functions to the DF vertex.

$$\chi_d^{\sigma\sigma'}(q) = \chi_d^0(q) + \frac{T^2}{N^2} \sum_{k,k'} G_\sigma^d(k) G_\sigma^d(k+q) \times \Gamma^{\sigma\sigma'}(q) G_{\sigma'}^d(k') G_{\sigma'}^d(k'+q) \qquad (4.26)$$

The momentum sum over $\mathbf{k}$ and $\mathbf{k}'$ can be performed independently by FFT because the DF vertex $\Gamma^{\sigma\sigma'}(q)$ only depends on the center of mass momentum q.

Now the z-component DF spin susceptibility $\langle S^z \cdot S^z \rangle = 2(\chi_d^{\uparrow\uparrow} - \chi_d^{\uparrow\downarrow})$ can be determined from the spin channel component calculated above. In Fig. 4.8, $\tilde{\chi}^{zz} = \chi^{zz} - \chi_0^{zz}$ is shown for $U/t = 4$ at temperatures $\beta t = 4.0$ (left panel) and $\beta t = 1.0$ (right panel). The momentum $\mathbf{q}_x$ and $\mathbf{q}_y$ run from 0 to 2π. The susceptibility is strongly peaks at the wave vector (π, π) and the peak value becomes larger with the decrease of temperature. The magnetic instability of the DF system is indicated by the enhancement of the DF susceptibility. The effect of momentum dependence in the vertex is clearly visible in this diagram. The bare vertex which is only a function of frequency becomes momentum dependent through the Bethe-Salpeter equation.

Later on we will see that such a momentum dependent vertex plays a very important role in the calculation of the lattice fermion susceptibility.

From this diagram, we also can see that the divergence at (π, π) is the most important one. Such divergence is more clear to see in the momentum distribution of $\tilde{\chi}^{zz}$. In Fig. 4.8, $\tilde{\chi}^{zz}(Q)$ as a function of Q is plotted for $U/t = 4$ and two different inverse temperatures $\beta t = 1.0$, and 4.0. Most of the weights gather at wave vector (π, π) at the lower temperature case and the peak value becomes higher and higher. The effect of momentum dependence of the vertex is clearly shown in this diagram. The bare vertex which is only a function of frequency becomes momentum dependent through the Bethe-Salpeter equation. Later on, we will see that such momentum dependent vertex plays a very important role in the calculation of real fermion susceptibility.

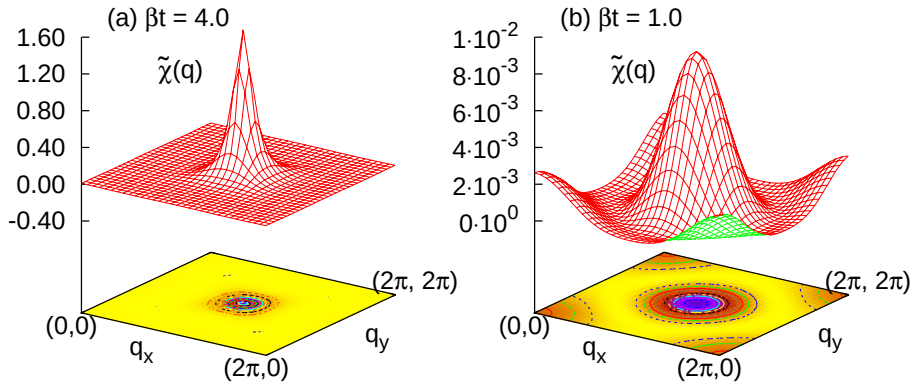

Figure 4.8: *Momentum distribution of nontrivial part of dual spin susceptibility.*

4.3.1 Lattice susceptibility in the DF method

The strong anti-ferromagnetic fluctuation in the 2D system is indicated by the enhancement of the DF susceptibility at the wave vector (π, π) shown in Fig. 4.8. This is the consequence of the deep relation between the the Green's function of the lattice and the DF, see Eq. (4.10). In order to observe the magnetic instability of the lattice fermion directly, we calculated the lattice susceptibility based on the DF method. By differentiating the partition function in Eqns. (4.4, 4.5) twice over the kinetic term, we obtain an exact relation between the susceptibility of the DF and lattice fermions. After some simplifications [Brener *et al.* (2008)], it is given by

$$\chi_f^{\sigma\sigma'}(q) = \chi_f^0(q) + \frac{T^2}{N^2} \sum_{k,k'} G'_\sigma(k) G'_\sigma(k+q) \Gamma^{\sigma\sigma'}(q) G'_{\sigma'}(k') G'_{\sigma'}(k'+q) \tag{4.27}$$

Here G' cannot be interpreted as a particle propagator, it is defined as:

$$G'_\sigma(k) = \frac{G^d_\sigma(k)}{g_\nu[\Delta_\nu - \epsilon(k)]} \tag{4.28}$$

Again, the sum is performed over internal momentum and frequency k, k' by FFT and the rough summing up a few Matsubara points. As in Eq. (4.10), this equation established a connection between the lattice susceptibility and the DF susceptibility. From this point of view, it is easy to understand that the instability of DF will lead to the instability of the lattice fermions.

One can also find relations for the higher order Green's function of the DF and the lattice fermions in the same way. This emphasizes the similar nature of the DF and lattice fermions except that DF possess only non-local information, since the DMFT self-consistency ensures that the local DF Green's function is exactly zero.

In this paper, we used two different ways to calculate the lattice susceptibility $\chi_m(q) = 2(\chi_f^{\uparrow\uparrow} - \chi_f^{\uparrow\downarrow})$. First we used the bare vertex $\gamma_\omega^{(4)}(\nu, \nu')$ which is obtained from the DMFT calculation. In contrast, the second calculation was performed using the full DF vertex in the spin channel $\Gamma_{s,q}(\nu, \nu')$. In both of calculations, the full one particle DF Green's function was used. The momentum dependent DF vertex is obtained through the calculation of the Bethe-Salpeter equation. By comparing these two calculations, we can understand the effect of momentum dependence in the DF vertex. The lattice susceptibility is expected to be improved if we use the momentum dependent DF vertex.

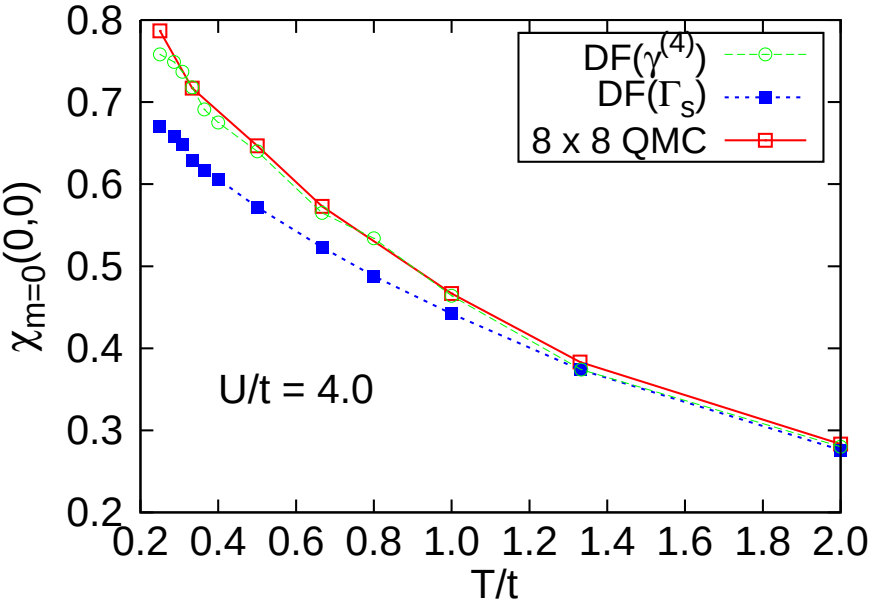

Figure 4.9: *The uniform spin susceptibility of the DF using the bare vertex and the full vertex for half filled 2D Hubbard model at $U/t = 4.0$ and various temperatures. These results reproduce the similar solution in comparison with the calculation of finite size QMC.*

In Fig. 4.9 we plotted the results for the uniform susceptibility $\chi_{m=0}(0, 0)$ by using both the bare and full DF vertex. The lattice QMC result [Moreo (1993)] is shown for comparison. The calculation is done for $U/t = 4.0$ and several values of

temperature. The momentum sum is approximated over 32×32 points here. Both of these calculations reproduce the well known Curie-Weiss law behavior. Surprisingly enough, the results for the bare vertex fit the QMC results better than that for the momentum dependent vertex. We attribute it to the finite size effect of QMC [Moreo (1993)]. A. Moreo showed that χ becomes smaller when increasing the cluster size N. The 4×4 cluster calculation result at the same temperature are larger than the results from a 8×8 cluster calculation. Therefore the results obtained from the full vertex is expected to be more reasonable.

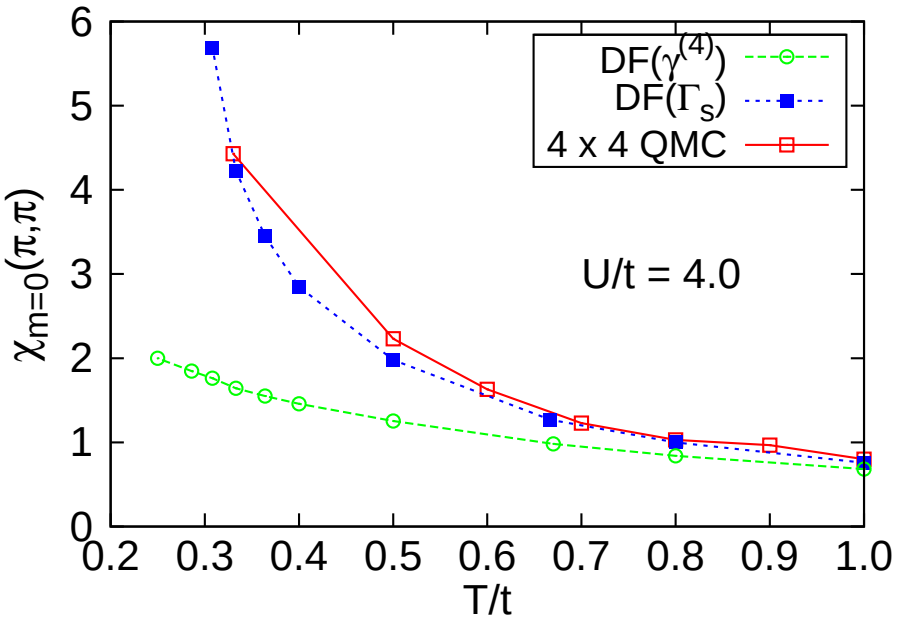

Figure 4.10: *Uniform spin susceptibility at the wave vector (π, π). The QMC results are obtained from Ref. [Bickers and White (1991)].*

The importance of the momentum dependence in the DF vertex is more clearly observed in the calculation of $\chi_m(\pi, \pi)$ shown in Fig. 4.10. Again, in this diagram QMC results [Bickers and White (1991)] are shown for comparison. The same parameters are used as in Fig. 4.9. The result from the DF with bare vertex does not produce the same results compared to the QMC solution. Even more interesting, with decreasing temperature the deviation becomes larger. On the other hand, the calculation with the momentum dependent vertex gives a satisfactory answer. This shows the importance of the momentum dependence in the DF vertex function.

Fig. 4.11 shows the evolution of χ against q for fixed transfer frequency $\omega_m = 0$. The path in momentum space is shown in the inset. From this diagram we can see that $\chi_m(\mathbf{q})$ reaches its maximum value at wave vector $\mathbf{q} = (\pi, \pi)$. Fig. 4.12 shows the momentum evolution of the lattice susceptibility for $U/t = 4.0$ and inverse temperatures $\beta t = 1.0, 4.0$. The increasing value at wave vector $\mathbf{q} = (\pi, \pi)$ shows the formation of the anti-ferromagnetic order with the decrease of temperature.

Compared to the DF susceptibility shown in Fig. 4.9, we can see that although the DF is not a real particle, it has similar nature as the lattice fermion. The magnetic instability appeared in both DF and lattice fermion. The difference of the DF and the lattice fermion lies the absence of local property in the DF.

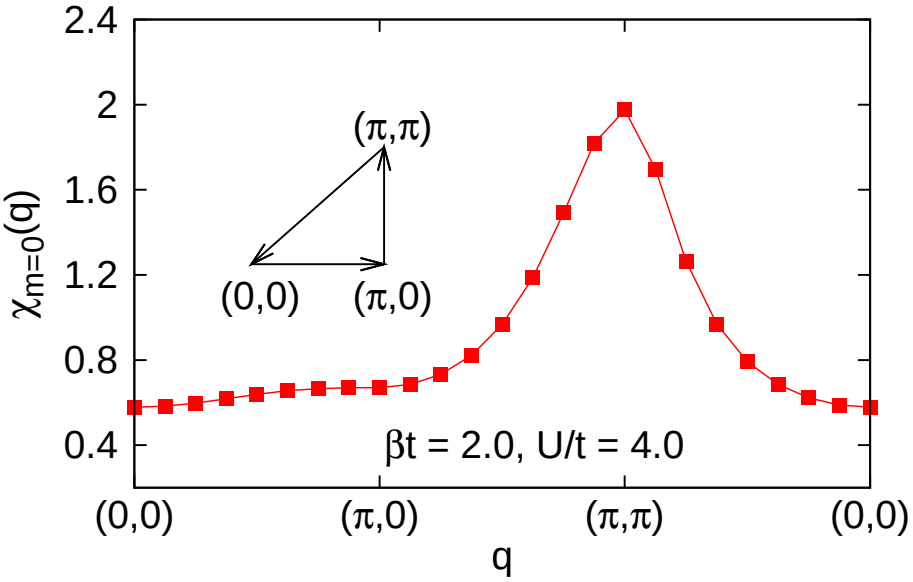

Figure 4.11: *$\chi(q)$ vs q at $\beta t = 2.0$, $U/t = 4.0$ for various q which is along the trajectory shown in the inset.*

In summary, the comparison between the DF and QMC results shows the good performance of the DF method. Our calculation could be done within four hours for each value of the temperature on average. In this sense, this method is cheap and reliable compared with the more computationally intensive lattice QMC calculation. Although we did self-consistent calculations in this paper under the current construction of the DF method, it is still possible to improve the above results. The full DF Green's function is calculated from the first two self energy diagrams shown in Fig. 4.1 and kept unchanged in the calculation of the Bethe-Salpeter equations. This is not self consistent in the sense that the momentum dependence of the full vertex(calculated from the Bethe-Salpeter equation) does not completely come into the calculation of the full DF Green's function, in the end the determination of the full vertex is not fully self consistent. The better way is to consider the ladder approximation of the DF which can determine the DF Green's function and the full vertex on equal footing. In this method, called ladder dual fermion approximation(LDFA), the DF Green's function is determined from the full vertex and used to calculate the new full vertex in the next iteration, this loop is executed until the full DF Green's function and vertex are not changed anymore. This approximation will improve the calculation of both the DF Green's function and the full vertex, especially for the 1D Hubbard model where the single site DMFT + DF calculation does not gave satisfactory results [Hafermann *et al.* (2007)]. It is supposed to be the

best approximation or the non-local correction of DMFT based on the two particle vertex $\gamma^{(4)}$. More details and corresponding results will be presented elsewhere.

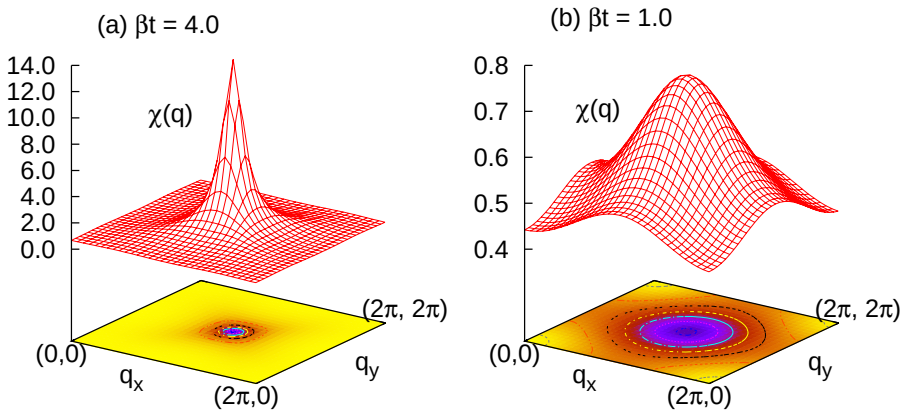

Figure 4.12: *The lattice susceptibility for $U/t = 4.0$ at two different temperatures $\beta t = 4.0$ and $\beta t = 1.0$ as a function of momentum calculated on 32×32 lattice.*

4.3.2 Lattice susceptibility in DΓA

Similar as the DF method, Dynamical Vertex Approximation (DΓA) [Toschi *et al.* (2007)] also bases on the two particle local vertex. It deals with the lattice fermion directly, without introducing any auxiliary field. The perturbative nature of this method ensures its validity at weak-coupling regime. Unlike in the DF method, DΓA takes the irreducible two particle local vertex as building blocks.

$$\gamma^{-1}_{c(s)}(\nu,\nu';\omega) = \gamma^{-1}_{c(s),ir}(\nu,\nu';\omega) - \chi_0(\nu;\omega)\delta_{\nu,\nu'}\Gamma^{-1}_{c(s)}(\nu,\nu';q) = \gamma^{-1}_{c(s),ir}(\nu,\nu';\omega) - \chi_0(\nu;q)\delta_{\nu,\nu'} \tag{4.29a}$$

The spin and charge vertices are defined as $\gamma_{c(s)} = \gamma^{\uparrow\uparrow} \pm \gamma^{\uparrow\downarrow}$. Note that we used a different definition of the spin and charge channels which is opposite to that in reference [Toschi *et al.* (2007)]. We will follow the work of A. Toschi et al. to determine the non-local self energy function and then to calculate the lattice susceptibility.

The bare susceptibility is defined as

$$\chi_0(\nu;\omega) = -TG_{loc}(\nu)G_{loc}(\nu+\omega) \tag{4.30a}$$

$$\chi_0(\nu,q) = -\frac{T}{N}\sum_{\mathbf{k}} G^0(k)G^0(k+q) \tag{4.30b}$$

And the self-energy is calculated through the standard Schwinger-Dyson equation

$$\Sigma(k) = -U\frac{T^2}{N^2}\sum_{k',q}\Gamma_f(k,k';q)G^0(k')G^0(k'+q)G^0(k+q) \tag{4.31}$$

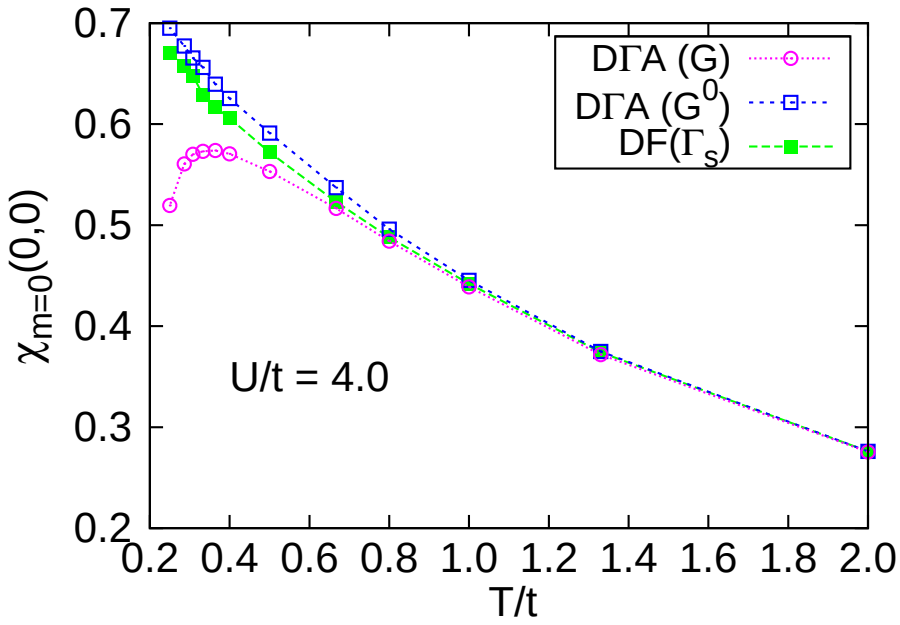

Figure 4.13: *Comparison with the DΓA susceptibility $\chi(0,0)$ which obtained from both the DMFT lattice Green's function (DΓA (G^0)) and the full Green's function (DΓA (G)), see context for more details.*

Here, the full vertex $\Gamma_f(k,k';q)$ is obtained by summing all the channel dependent vertices and subtracting the double counted diagrams.

$$\Gamma_f(k,k';q) = \frac{1}{2}\Big\{[3\Gamma_c(\nu,\nu';q) - \Gamma_s(\nu,\nu';q)] - [\Gamma_c(\nu,\nu';\omega) - \Gamma_s(\nu,\nu';\omega)]\Big\} \quad (4.32)$$

which depends only on one momentum argument $\mathbf{q}$. The one particle propagator is given by the DMFT lattice Green's function where the self energy is purely local $G^0(k) = 1/[i\nu - \epsilon(k) - \Sigma(\nu)]$, the local Green's function is $G_{loc}(\nu) = 1/[i\nu - \Delta(\nu) - \Sigma(\nu)]$. Then the Dyson equation gives the lattice Green's function from the self-energy function $G^{-1} = G_0^{-1} - \Sigma$. The lattice spin susceptibility within the DΓA method is obtained by attaching four Green's functions on the vertex obtained in Eq. (4.29).

$$\chi(q) = \chi_0(q) + \sum_{\nu,\nu'} \chi_0(\nu,q)\Gamma_s(\nu,\nu';q)\chi_0(\nu',q) \quad (4.33)$$

There are two possible choices of the lattice Green's function to construct the bare susceptibility $\chi_0(q)$ and $\chi_0(\nu,q)$. One is the DMFT lattice Green's function G^0. The other one is the Green's function G constructed by the non-local self-energy from the Dyson equation. In fact, the former is the way to determine the lattice susceptibility from DMFT, which is not related with DΓA equation (4.32).

Before presenting the numerical results of the lattice susceptibility in DΓA, we

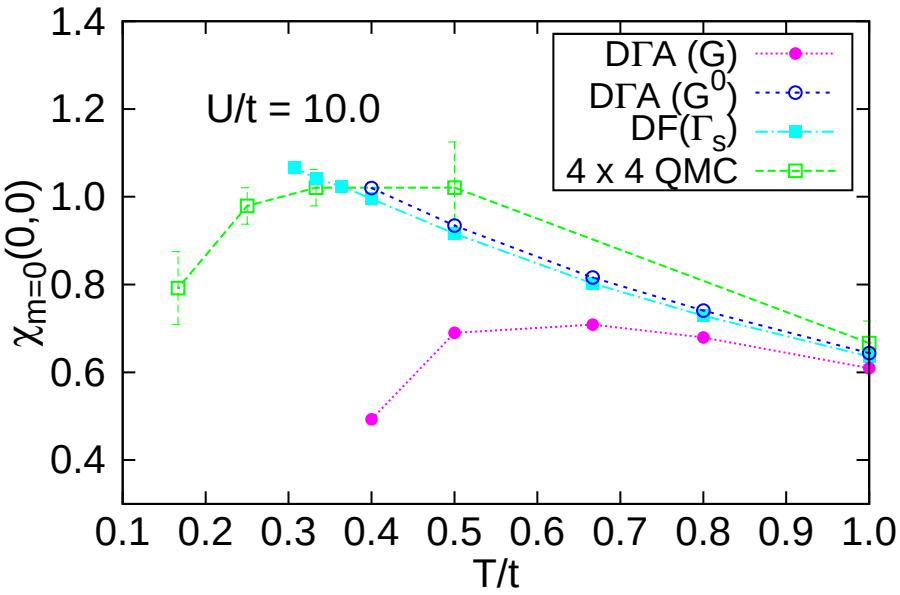

Figure 4.14: *The comparison of the DF results and that of QMC for the uniform susceptibility at $U/t = 10$. 4×4 QMC results [Moreo (1993)] also shows the error bars.*

---

take a deeper look at the analysis of Eq. (4.29),

$$\Gamma^{-1}_{c(s)}(\nu,\nu';q) = \gamma^{-1}_{c(s)}(\nu,\nu';\omega) - [\chi_0(\nu;q) - \chi_0(\nu,\omega)]\delta_{\nu,\nu'} \tag{4.34}$$

The second term in the brackets on R.H.S. removes the local term from the bare susceptibility. The whole term in the brackets then represents only the non-local bare susceptibility. In order to compare with the DF method, we take the inverse form of Eq. (4.25)

$$\Gamma^{-1}_{d,cs}(\nu,\nu';q) = \gamma^{-1}_{c(s)}(\nu,\nu',\omega) + \frac{T}{N}\sum_{\mathbf{k}} G^d(k)G^d(k+q) \tag{4.35}$$

The above two equations are the same except for the last term. Since the local DF Green's function G^d_{loc} is zero, the bare DF susceptibility is purely non-local which coincides with the analysis of DΓA Bethe-Salpeter equation. Therefore, it will not be surprising if these two methods generate similar results. It is not easy to perform a term to term comparison between the DF method and DΓA although the bare susceptibility has no local term in both of these methods, because the one particle Green's functions have different meanings in these two methods.

In Fig. 4.13 and 4.15, we presented the DΓA lattice susceptibility calculated from both the DMFT lattice Green's function labeled as DΓA(G^0) and the full Green's function labeled as DΓA(G). The DF result from the calculation with the full DF vertex is re-plotted for comparison. In Fig. 4.13, the DΓA susceptibility calculated from the DMFT Green's function (DΓA(G^0)) is basically the same as

the DF susceptibility with only small deviations. The results for $T/t > 1.0$ which are not shown here nicely repeat the DF and QMC results, the deviation between the DΓA and the DF method becomes smaller with the increase of temperature. The DΓA susceptibility calculated from the full Green's function (DΓA(G)) shows a different behavior at the low temperature regime which reaches its maximum value at $T/t \approx 0.36$. As we know, the Hubbard Model in the strong coupling regime can be mapped to the Heisenberg model, χ reasches a maximum at $T \approx J$ where J is the effective spin coupling constant given as $4t^2/U$. The calculation uses the parameter $U/t = 4.0$ which is in the intermediate coupling regime. In order to investigate the behavior of $\chi(0,0)$ in the strong coupling region, we further calculated the lattice susceptibility at $U/t = 10.0$ which are shown in Fig. 4.14.

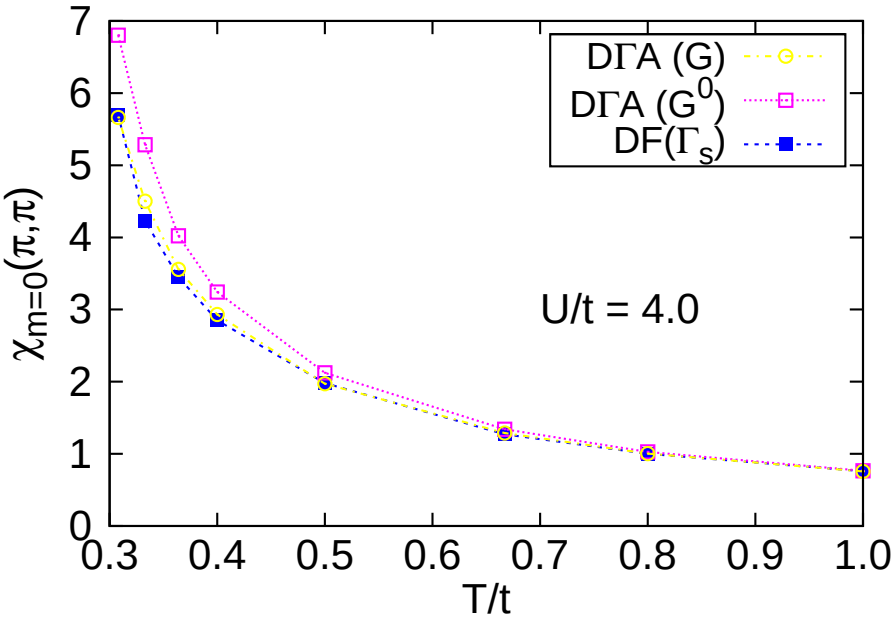

Figure 4.15: *DΓA susceptibilities $\chi(\pi,\pi)$ at $U/t = 4.0$. The susceptibility is determined from both of the DMFT and full lattice Green's function together with the vertex obtained from Eq. (4.32)*

.

When the temperature is greater than 0.4, the DF method and DΓA (DΓA(G^0)) generate similar results to the QMC calculation. Reducing the temperature further, the QMC susceptibility greatly drops and peaks at around 0.4 which coincides with the behavior of the Heisenberg model. The DF femion and DΓA(G^0) susceptibility continuously grow with the decrease in temperature. Although the DΓA with the full Green's function (DΓA(G)) shows a peak, it locates at $T/t = 0.6667$ which is larger than the peak position of the QMC. And DΓA(G) generated a large deviation from that of QMC. In this diagram, we only show the results of the DF approach for $T/t > 0.3$ and the DΓA results for $T/t > 0.4$. The Bethe-Salpeter equation of the

DΓA have an eigenvalue approaching one with the decrease of temperature, which makes the access of lower temperature region impossible.

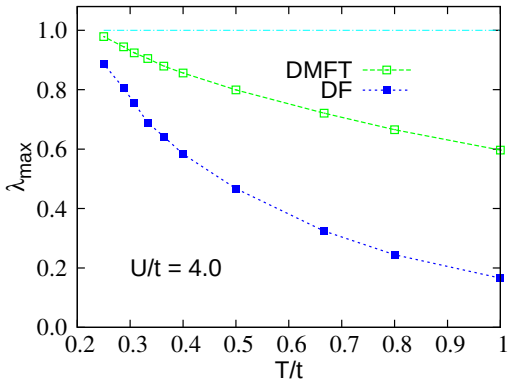

Figure 4.16: *The comparison of the maximum eigenvalue in spin channel in the DF and DMFT for different temperature.*

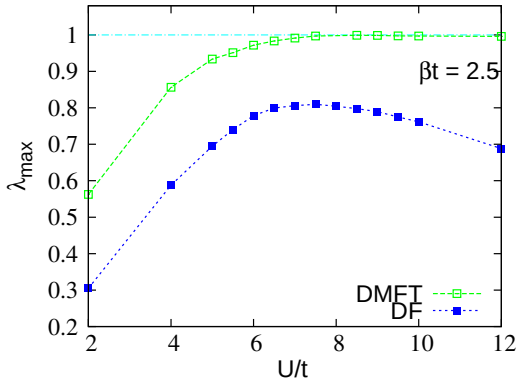

Figure 4.17: *λ_{max} in the DF and DMFT at $\beta t = 2.5$ for different interaction U/t.*

Fig. 4.15 shows the results of DΓA susceptibility at wave vector (π, π). In contrast to the comparison for $\chi(0,0)$ results, the DΓA susceptibility calculated from the full Green's function DΓA(G) yields better results than that from the calculation with the DMFT Green's function DΓA (G^0). DΓA (G) results are almost on top of the DF results, the results with DMFT Green's function DΓA(G^0) is large than the DF results. The deviation becomes larger at lower temperature. Summarizing, the DΓA calculation using the full Green's function generated the same result as the DF method for $\chi(\pi, \pi)$ while it failed to produce $\chi(0,0)$ correctly. In contrast, the calculation with the DMFT Green's function in DΓA nicely produced the results calculated with the DF method for $\chi(0,0)$ while generating larger deviation for $\chi(\pi, \pi)$ at the lower temperature regime. Together with Fig. 4.9 and 4.10, we can see that the DF fermion calculation with the full DF vertex generated basically the same results for both $\chi(0,0)$ and $\chi(\pi, \pi)$ compared to the results of QMC.

The strange behavior of the DΓA lattice susceptibility calculated from the full Green's function (DΓA(G)) at $\mathbf{q} = (0,0)$ can be partially attributed to the non self-consistency introduced in this method. The full vertex is calculated through the Bethe-Salpeter equation (4.29) with the DMFT lattice Green's function G^0. While the four Green's functions which attach on the vertex are the full Green's function. The better way is to determine the full vertex self-consistently from the corresponding full Green's function. Such nonself-consistent calculation might be one reason responsible for the unreasonable results at the low temperature region. The introduction of a Moriyaesque λ correction [Held *et al.* (2008); Katanin *et al.* (2008)] to DΓA will further improve the performance of this method.

In both the DF method and the DΓA, the operation of inverting large matrices is required for solving the Bethe-Salpeter equation. Fig. 4.16 shows the leading eigenvalue of Eqns. (4.25) and (4.29). As expected, the leading eigenvalue approaches one with decreasing temperature which directly indicates the magnetic instability

of 2D system. The eigenvalues corresponding to the DF fermion method always lie below those from DΓA calculation, which indicates the better convergence of the DF method. When the leading eigenvalues are closed to one, the matrix inversion in Eqns. (4.25) and (4.29) are ill defined, which prevents the investigation at very low temperature. The smaller values of the DF leading eigenvalues also indicate that compared to the lattice fermion, the DF are weakly coupled to each other. This is more clearly seen in Fig. 4.17. Globally the curve corresponding to the DF lies below that of the DMFT which again indicates the better convergence of the DF method. Furthermore, we observed that in larger interaction regime, the leading eigenvalue in the DF drops down with the increasing of interaction strength which indicates the weak-coupling nature of the dual fermion. The weak-coupling nature ensures the validity of the perturbative solution of the dual fermion self energy. In contrast, the DMFT leading eigenvalue becomes one when $U/t > 6.0$.

4.3.3 Away half filling

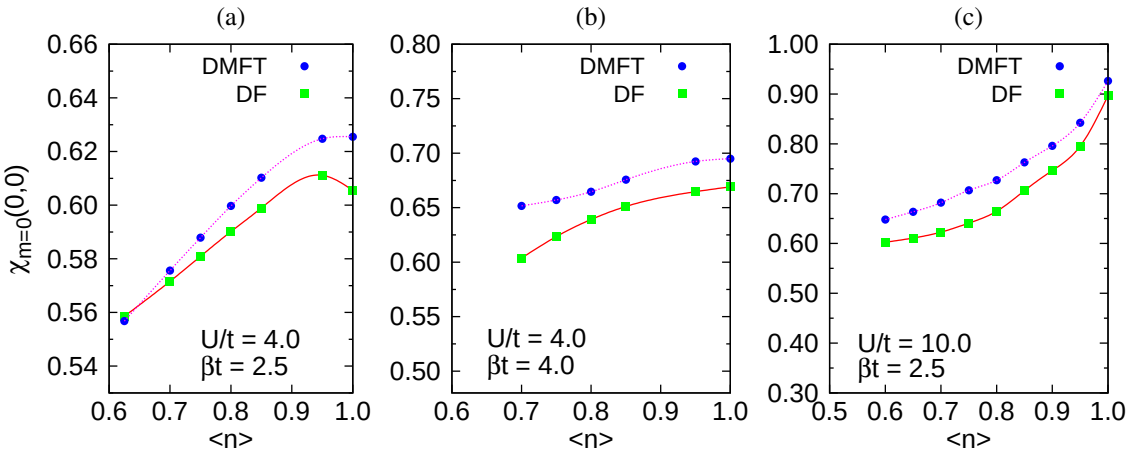

Figure 4.18: *Uniform magnetic susceptibility is plotted as a function of doping at* $\beta t = 2.5$ *and* $U/t = 4.0, 10.0$.

We also calculated the uniform susceptibility at away half-filling. In the strong-coupling limit, the Hubbard model is equivalent to the Heisenberg model with coupling constant $J = 4t^2/U$. The consequence of doping is to effectively decrease the coupling J, which yields the increasing behavior of χ with doping. The finite size QMC calculation [Moreo (1993); Chen and Tremblay (1993)] observed a slightly increasing χ with very small doping at strong interaction or in the low temperature region. Here, we did a similar calculation at $\beta t = 2.5$ and $U/t = 4, 10$. Since the DF method and the DΓA do not suffer from the finite size problem, we would expect to observe results similar to those of QMC [Moreo (1993); Chen and Tremblay (1993)]. In ΓA the susceptibility is calculated from the DMFT Green's function G^0 and the vertex obtained from Eq. (4.32). As shown in Fig. 4.18 at $U/t = 4.0$, the susceptibility χ slightly increases in the weak doping region where δ is around 0.05, DF

fermion results clearly showed such behavior, DΓA also gave a signal of it. Further doping the system, both the DΓA and the DF method reproduce the decrease with doping as already seen in the QMC. With the increasing of interaction, we would expect to see the enhancement of this effect, however our calculations indicate that such increasing-decreasing behaviors dissappear. Both the DΓA and the DF method give the same decreasing curve which contradict QMC results [Moreo (1993)].

Fig. 4.19 shows the comparison of the DMFT, DF and DΓA spin susceptibility for 2D square lattice. The parameter is set as $U/t = 4.0$ and $n = 0.875$. Here the QMC(BWS) results are also given as comparison.

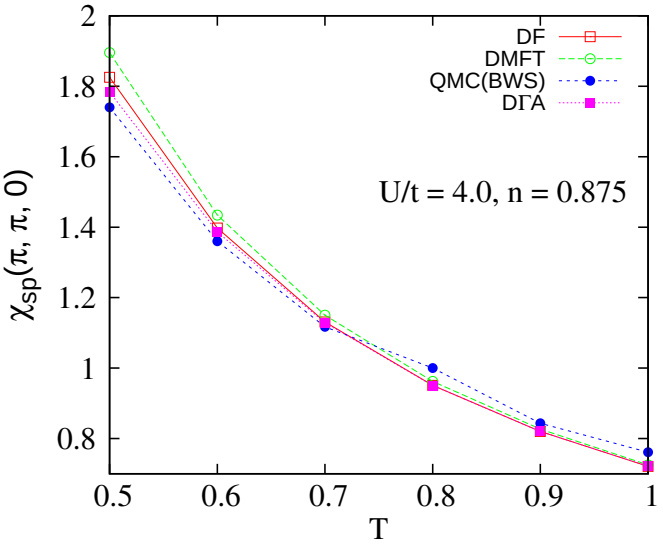

Figure 4.19: *Temperature dependence of spin susceptibility at wave vector $q = (\pi, \pi)$ and $\Omega_m = 0$. Coulomb interaction is set as $U/t = 4.0$ and hole doping is $\delta = 0.125$. QMC(BWS) results are obtained from reference [Vilk and Tremblay (1997)]*

At a temperature higher than 0.7, the DF, DΓA results are same as DMFT susceptibility which have only small deviations from the QMC(BWS) results. Lowering the temperature, the corrections to DMFT susceptibility from the DF and DΓA method become obvious. When the temperature is lower than 0.7, DF, DΓA and DMFT susceptibility become larger than that of QMC(BWS). And the deviation becomes larger with the decrease of temperature. The DF and DΓA generated reasonable corrections to DMFT results compared to QMC(BWS) susceptibility, especially at the lower temperature regime.

Figure 4.20 shows the comparison of the spin susceptibility between the DF calculations and the DCA calculations obtained from a recent work [Honchkeppel *et al.* (2008)]. q_x and q_y are from 0 to 2π. The upper diagram is obtained form the dca extension [Honchkeppel *et al.* (2008)]. Basically, the DF result is in good agreement with that of the extension of DCA [Honchkeppel *et al.* (2008)] calculation. Here in the DF calculation 24×24 momentum grids are used. The above calculations were done within 4 hours on a single PC. In the DCA calculation, 8×8 cluster was used, which is already the maximum cluster site number which can be considered with respect to the calculation of susceptibility. In this sense, the DF method has a very good momentum resolution and introduces less computational burden.

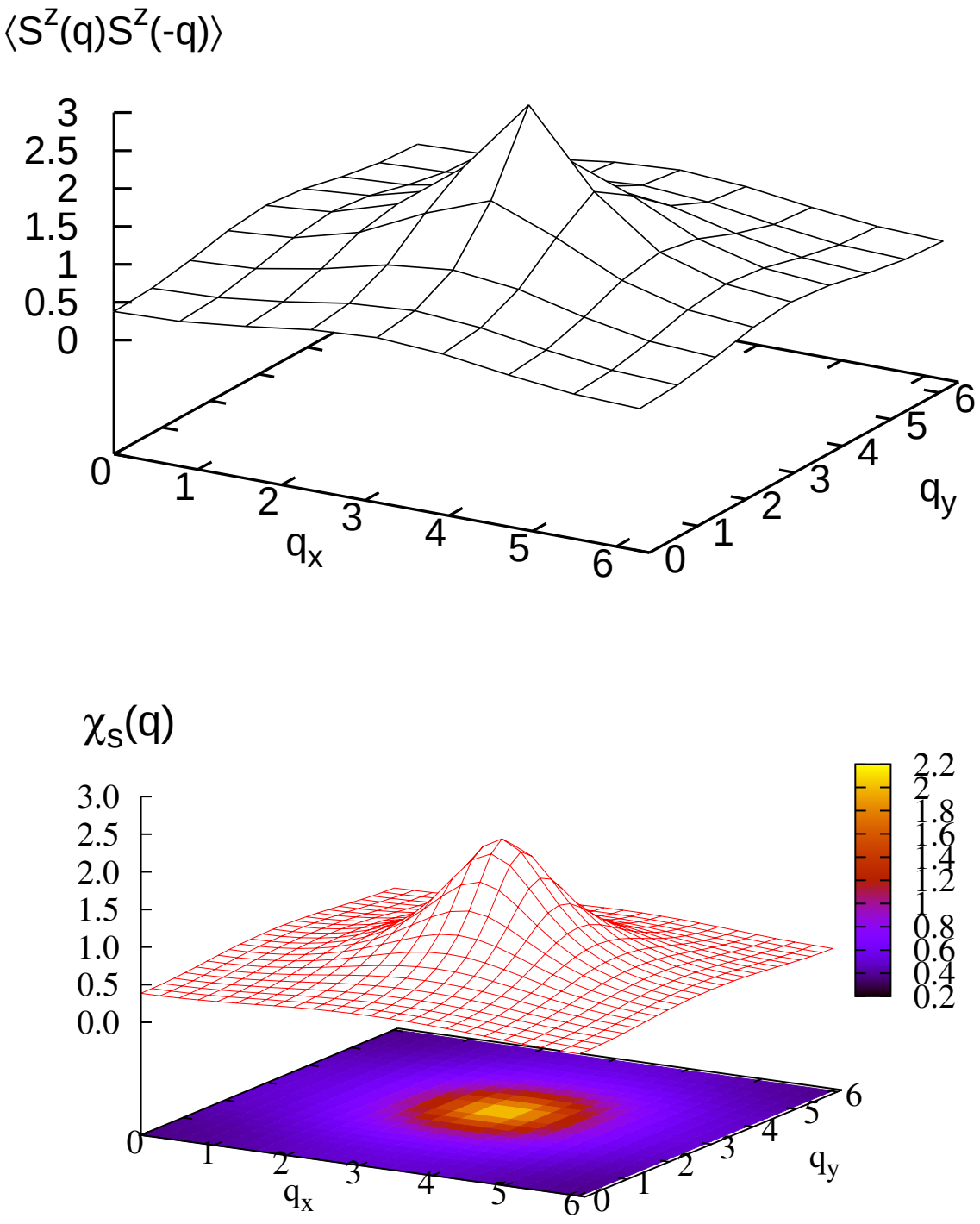

Figure 4.20: *Comparison of DF and the extension of DCA for the spin susceptibility at $\beta t = 3$, $U/t = 8$ and $n = 0.85$.*

Chapter 5

Hubbard Model on the Triangular and Bilayer lattice

5.1 Triangular lattice – Frustration effect

In the second chapter, we gave an example of the cluster DMFT implementation on the square lattice. Where we observed that the perfect nested Fermi surface is distorted by the introducing of the next nearest neighbor hopping t'. The Fermi surface cannot be connected by the wave vector $Q = (\pi, \pi)$. Finite value of t' in the end suppressed the anti-ferromagnetic order. The interplay between the geometrical frustration and the strong electronic correlations leads to the emergence of unconventional phases. Recently a number of materials have been discovered where we can actually investigate such interplay, such as the organic charge transfer materials κ-(BEDT-TTF)$_2$Cu$_2$(CN)$_3$ [Shimizu *et al.* (2003); Tamura and Kato (2002); Coldea *et al.* (2003)]. Fig. 5.1 shows the single layer geometry structure of κ-(BEDT-TTF)$_2$Cu$_2$(CN)$_3$.

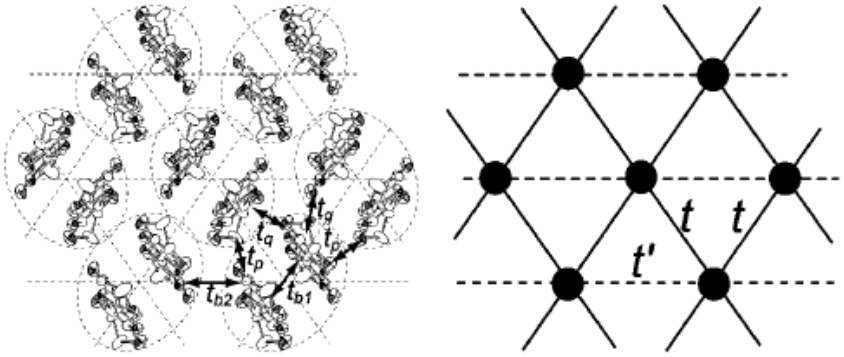

Figure 5.1: *κ-(BEDT-TTF)$_2$Cu$_2$(CN)$_3$ structure and corresponding triangular lattice representation. Figure is obtained from Ref. [Shimizu* et al. *(2003)].*

The effective structure of κ-(BEDT-TTF)$_2$Cu$_2$(CN)$_3$ can be represented by a triangular lattice. Compared to the square lattice, the triangular lattice has quite different properties. At 2D square lattice, the ground state of the Hubbard model is

an anti-ferromagnetic insulator due to the perfect nested Fermi surface. The absence of the nested Fermi surface in the triangular lattice allows the existence of the paramagnetic metal. Thus a Metal-Insulator transition is expected to exist in a triangular lattice. A lot of theoretical attempts have proven this assumption [Ohashi *et al.* (2008); Aryanpour *et al.* (2006); Imai and Kawakami (2002)], the first order Metal-Insulator transition was observed. At strong coupling regime, the ground state was suggested as a magnetically ordered state in which neighboring spins are rotated by 120 degrees relative to one another [Bernu *et al.* (1994); Capriotti *et al.* (1999); Huse and Elser (1988)].

Due to the frustration, the short range correlation is supposed to be dominant in the triangular lattice. DMFT is then a good approximation in this case. In this chapter, we will present the calculation of Cellular DMFT, DCA and the DF method on the triangular lattice. The Metal-Insulator transition is identified as first order from the jump of the double occupancy. The formation of the magnetic state is studied by the calculation of the uniform spin susceptibility.

Let us consider the single-band Hubbard model on the triangular lattice which is given as on right hand of figure in Fig. 5.1. The corresponding Brillouin Zone is shown in Fig. 5.2.

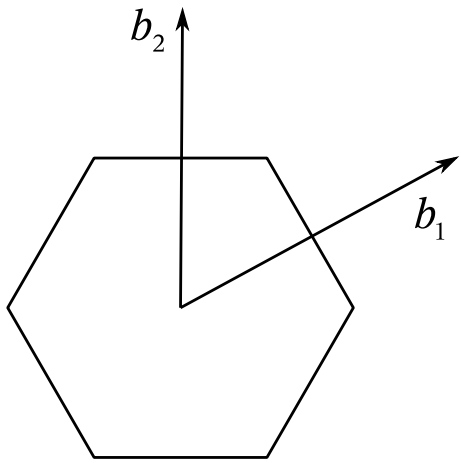

Figure 5.2: *The first Brillouin Zone of the triangular lattice. The unit vectors b_1 and b_2 are $b_1 = (2\pi, \frac{2\pi}{\sqrt{3}}), b_2 = (0, \frac{4\pi}{\sqrt{3}})$. The corresponding real space unit vectors are $a_1 = (1, 0), a_2 = (-\frac{1}{2}, \frac{\sqrt{3}}{2})$*

The dispersion relation is given as

$$\epsilon_k = -2t' \cos(k_x) - 4t \cos(\frac{\sqrt{3}}{2} k_y) \cos(\frac{k_x}{2}) - \mu \tag{5.1}$$

The non-interacting density of state for different t' is shown in Fig. 5.3. For $t'/t = 1$, there is a single peak which splits to two peaks when $t'/t = 0.8$. Note, the density of state for $t'/t = 1$ is similar to that for the square lattice with the next neighboring hopping term, see Fig. 2.8. When $t'/t = 0$ it reduces to a lattice without frustration whose density of state is exactly same as that of the square lattice. The triangular lattice and the frustrated square lattice are topologically equivalent. Later on for the interacting case we will use the square lattice geometry instead of the triangular lattice (see later section for more details).

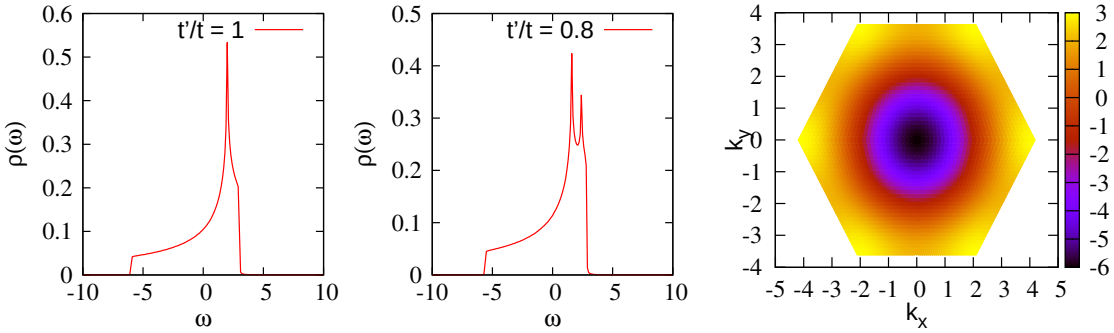

Figure 5.3: *Density of state $\rho(\omega)$ of the triangular lattice for two different t'/t. The dispersion relation for $t'/t = 1$ is plotted.*

5.1.1 Metal-Insulator Transition

In this section, we will first present the single site DMFT calculation result to get insight of the Metal-Insulator transition on the triangular lattice. C-DMFT and DCA results will also be presented in order to see the non-local fluctuation effect on the transition.

The application of single site DMFT on triangular lattice has been done by Merino and Aryanpour [Merino *et al.* (2006); Aryanpour *et al.* (2006)]. ED and Fluctuation exchange approximation (FLEX) were used as cluster solver and the finite size determinant QMC (DQMC) was also performed as comparison. The Meal-Insulator transition was observed at $U/t \approx 12$. Here, we used CTQMC to solve the DMFT equations which is much more accurate than FLEX. For convenience, from now on we would like to use the anisotropic square lattice instead of the triangular lattice. The bare density of state for the anisotropic square lattice is same as the triangular lattice with the advantage of a simpler first Brillouin Zone. The C-DMFT and DCA equations are also formulated for this geometry.

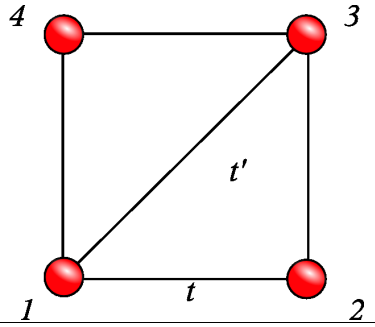

Figure 5.4: *Anisotropic square lattice which has the same non-interacting density of state as the triangular lattice.*

In single site DMFT, the dispersion relation for the anisotropic square lattice with $t' = t$ is given as

$$\epsilon(k) = -2t(\cos(k_x) + \cos(k_y)) - 2t\cos(k_x + k_y) \tag{5.2}$$

k_x and k_y are in the first Brillouin zone $[0, 2\pi]$. Fig. 5.5 shows the density of states for different temperatures and interactions. The similar diagrams can be found

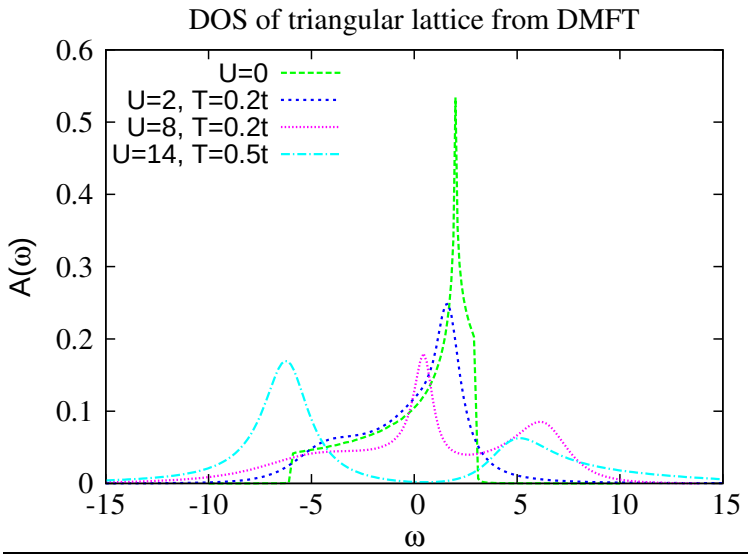

Figure 5.5: *The density of state of the anisotropic square lattice for various interactions and temperatures.*

in reference [Aryanpour *et al.* (2006)]. The analytical continuation is done by a simple Päde approximation which is not normally numerically stable. Here our high resolution Green's function data from the CTQMC ensures the good quality of the density of states. The Metal-Insulator transition is clearly seen for the formation of the Mott gap at the large interaction case. The distance of the upper and lower band is approximately 14 which is the same as the interaction strength in the last curve.

One Particle Property

As widely known, FLEX is a good approximation in the high temperature and small interaction regime, it overestimates the spin fluctuation which opens the psecudogap before it actually does. In the work of Aryanpour [Aryanpour *et al.* (2006)], the determinant QMC results were shown as a comparison for $U/t = 4$ and $U/t = 8$, which are smaller than the total band width $9|t|$ of the triangular lattice. And

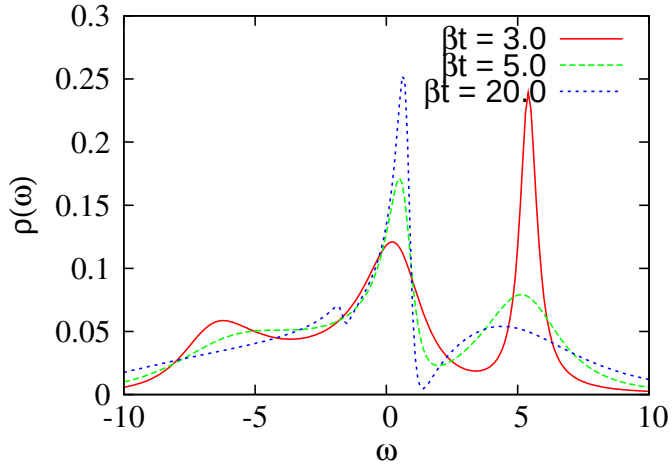

Figure 5.6: *The evolution of the total density of state with the temperature shows the enhancement of the coherent peak for $U/t = 8.0$.*

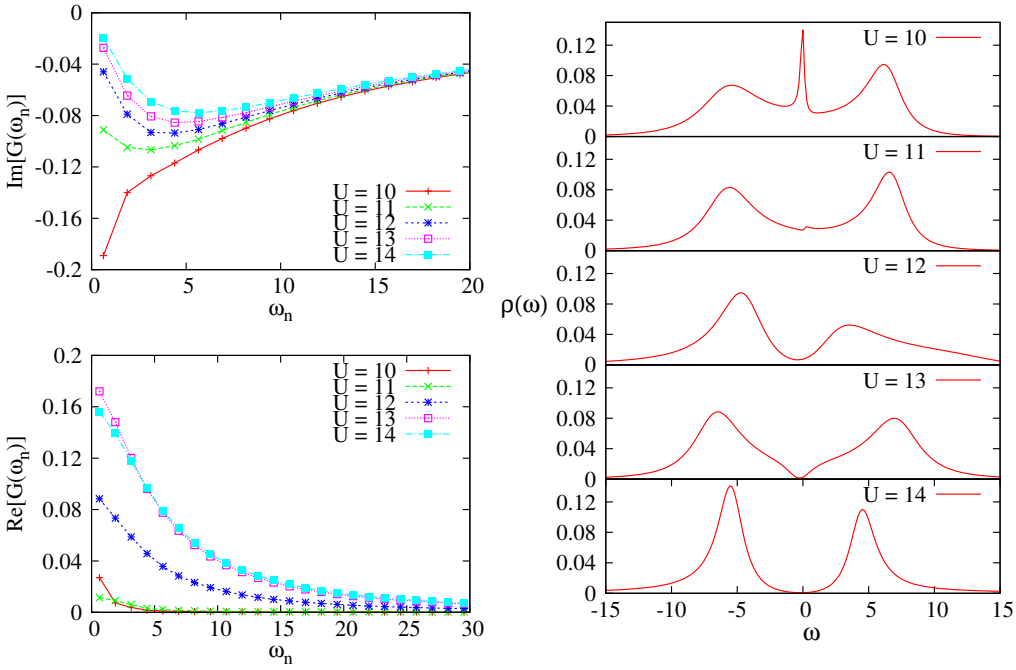

Figure 5.7: *The imaginary and real part of the local Green's function at $\beta t = 5.0$ for different interaction strength. The right panel shows the corresponding density of state. The Mott gap is open when $U \geq 13.0$.*

with the increase of interaction strength, the deviation between DQMC and FLEX becomes larger, especially in the low temperature regime. FLEX predicted the Mott gap was open at $U \approx 12$, which was smaller than the ED solution. This difference could originate with the two following reasons: (1) Spin fluctuation is overestimated in FLEX, which opens the Mott gap at a smaller interaction region (2) temperature might play a role here, since being as weak-coupling method, FLEX is only reliable in the higher temperature regime. While ED is a zero temperature technique. To understand the difference between FLEX and ED results, we employ the CTQMC, which is a numerically exact method to solve DMFT equations. If the temperature really plays a role, the critical interaction U_c should become larger. First, we calculated the density of state for $U/t = 8.0$ which is within the metal region. If the above argument is true, we should be able to see the enhancement of the coherent peak at $\omega = 0$ with the lowering of temperature since in the lower temperature case $U/t = 8.0$ is deeper in the metallic regime than in the higher temperature case. From Fig. 5.6 we can see that this is true. With the lowering of temperature, the quasiparticle peak becomes sharper at $\omega = 0$.

Fig. 5.7 shows the density of states at $\beta t = 5$ for different interactions. The Mott gap is completely open at $U/t \approx 13.0$, which is within the range of U_c^{HT}/t and U_c^{LT}/t. Further decreasing the temperature, the critical interaction U_c will become larger. The right panel of Fig. 5.7 shows the imaginary and real part of the local Green's function. Due to non-zero values of the real part, we cannot identify the transition from the jump of the $Im[G(i\omega_1)]$.

As a conclusion, the single site DMFT shows the metal-insulator transition in the interaction range $U/t \approx 12$ to 15 at different temperatures. With the lowering of temperature, the critical interaction becomes larger. From the difference in the phase diagram from single and cluster DMFT calculations, one can further understand the role of the non-locality in the triangular system. The complete phase diagram of the triangular lattice from single site DMFT will be carefully examined in the future.

Double Occupancy

The frustration in the triangular lattice ensures the applicability of DMFT in this 2D system. Still the non-local fluctuation effect cannot be omitted here. Thus we adopt the C-DMFT and DCA methods to explicitly examine the short-range correlation effect on the triangular lattice. The double occupancy was examined by these two cluster DMFT methods, the first order Metal-Insulator transition was observed from the discontinuity of the double occupancy. Here, C-DMFT and DCA

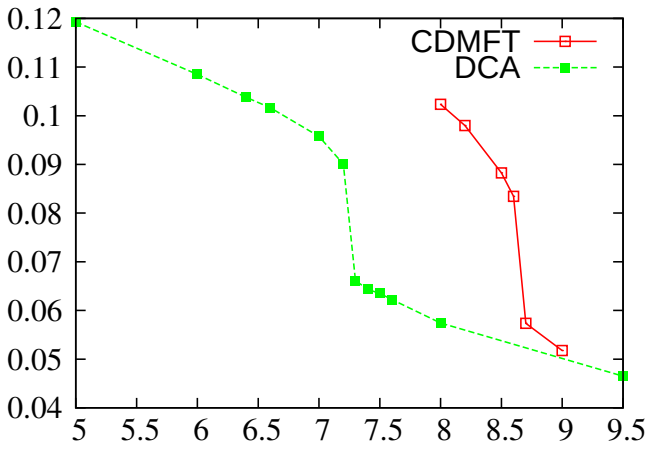

Figure 5.8: *The double occupancy $< n_\uparrow n_\downarrow >$ calculated from DCA and C-DMFT for the anisotropic square lattice at $\beta t = 20$.*

generated different critical interaction U_c. It is around 8.7 in C-DMFT and 7.2 in DCA. The difference originates from the different boundary conditions adapted in these two cluster DMFT methods. In C-DMFT the open boundary condition is used, the hopping is in the scope of the supper-lattice. In DCA, the periodic boundary condition is used, electrons hop in the original lattice but the wave vector is in the Reduced Brillouin Zone. Despite the different boundary condition, these two methods are supposed to give the same results when the cluster size becomes large enough. For smaller size cluster, it is reasonable that there is a difference in the results from C-DMFT and DCA. If the physics in the triangular lattice is dominated by the local or short range correlations, the single site DMFT or the small size cluster DMFT should be sufficient to generate the same results. But here, we observed that C-DMFT and DCA basically gave a quantitatively different critical interaction which indicates the non-local nature of this problem. Although the frustration is supposed to suppress the non-local fluctuation and favor the formation of local moments, the 2×2 cluster is still not big enough to include most of the correlations in the triangular lattice.

After including the short range correlation effect, the critical interaction U_c becomes smaller compared to single site DMFT results which means the non-local fluctuation cannot be omitted here. To go beyond the local and short range correlation, we are going to use the DF method introduced in the previous chapter.

5.1.2 Magnetic Properties

After observing the Metal-Insulator transition, the next nontrivial problem is to understand why there is a Metal-Insulator transition in this system, or to know which states dominate this system when the Mott gap is open.

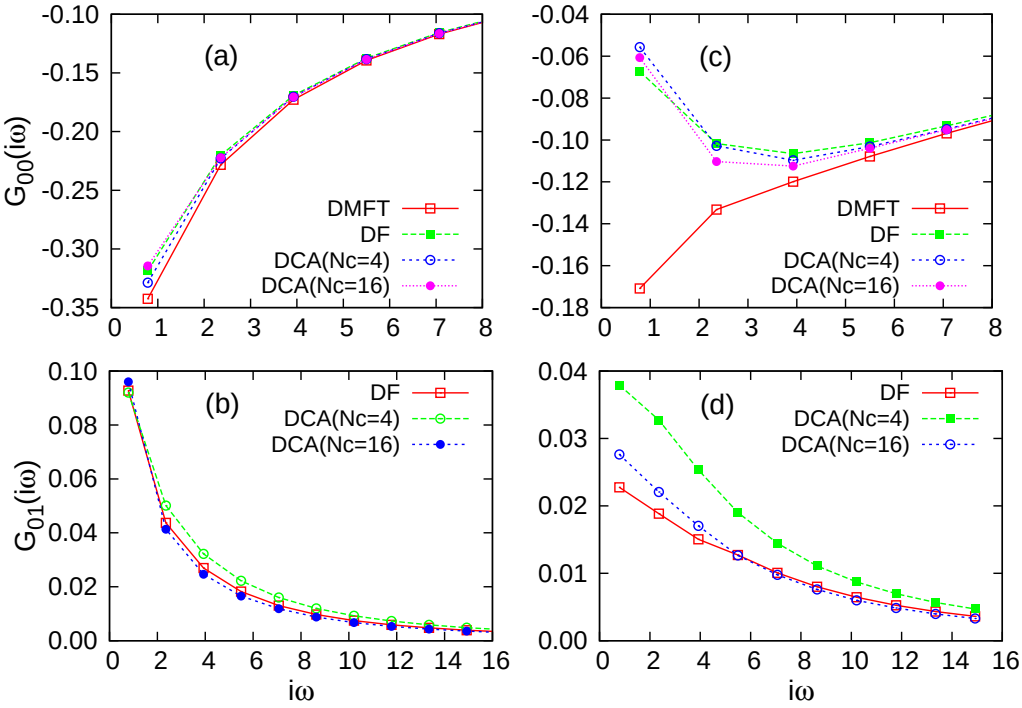

Figure 5.9: *The non-local correction from the DCA and DF method to the single site DMFT results for $\beta t = 4$, $U/t = 6$ ((a) and (b) diagrams) and $U/t = 10$ ((c) and (d) diagrams).*

In the square lattice, DMFT predicts that the Mott transition occurs at around $U/t = 12.0$ in the paramagnetic states. After including the anti-ferromagnetic symmetry breaking, the 2D square lattice is always insulating in the lower temperature regime due to the perfect nested Fermi surface. As noted, the frustration in the triangular lattice destroyed the nested Fermi surface, which allows the existence of the metallic states. This can also be true even if we take the anti-ferromagnetic symmetry breaking field into account. Then the Metal-Insulator transition occurs at finite interaction region.

Long Range Correction

As we discussed above, the different boundary conditions in C-DMFT and DCA indicates that 2×2 cluster is not big enough. Here we used the DF method to calculate the non-local corrections to the single site DMFT results. As noted, this method basically has taken both the short and long range correlation effects into account in an approximate way. This method does not suffer the finite size problem.

In Fig. 5.9 we showed the comparison of the one particle Green's function calculated by DMFT, DCA and DF method. A different cluster size was used in order to see the effect of the long range correlation. In this figure we showed the imaginary part of the local Green's function G_0 (the upper two diagrams) and the real part of the nearest neighboring Green's function G_1 (the lower two diagrams).

These three methods generated quite similar results at smaller interaction case $U/t = 6$. The non-local effect is not obvious, the corrections from DCA and DF are small. We can see that the DF method results are closer to the $Nc = 16$ cluster DCA results, which is reasonable since the DF method basically included the long range correlations. This effect can be seen much clearer at stronger interaction case $U/t = 10$. Again the DF method generated a result closer to those from $N_c = 16$ than $N_c = 4$. Single site DMFT overestimates the critical interaction U_c due to the lack of the non-local fluctuation effect. At $U/t = 10$ case, DMFT shows the metallic behavior while the DF and DCA reasonably gave the insulating results.

The 120-degree State

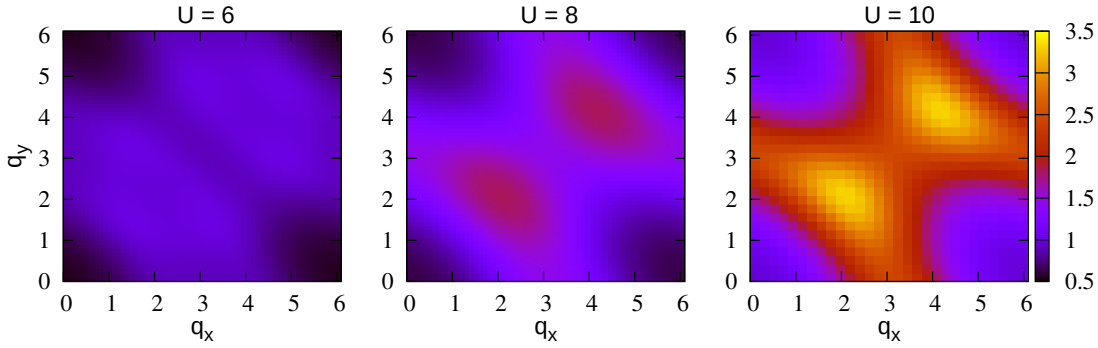

Figure 5.10: *The evolution of the spin susceptibility with the interaction strength at $\beta t = 2.5$. With the increasing of interaction, the spin susceptibility diverges at $(2\pi/3, 2\pi/3)$.*

In the square lattice, when the anti-ferromagnetic symmetry breaking field is included, the system is insulating for any interaction strength in the lower temperature regime. The spin is anti-parallel to the neighbors. The whole square lattice can be divided into two subi-lattices which relates with each other through the wave vector $Q = (\pi, \pi)$. For example $\epsilon_A(k) = \epsilon_B(k + \pi)$, here A and B are the indices of the two sub-lattice. Consequently the spin susceptibility peaks at $Q = (\pi, \pi)$. The formation of the spin susceptibility peak indicates that, on the one hand the magnetic

state forms and dominates the system, on the other hand the spin configuration for two neighboring electrons is anti-parallel.

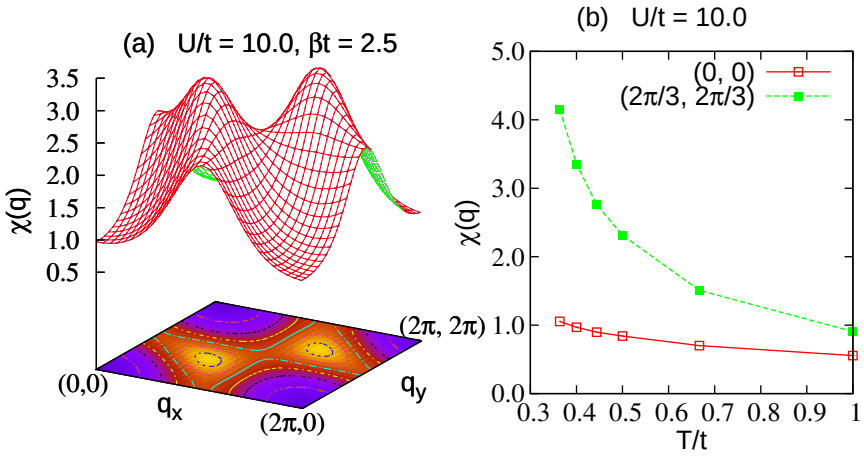

Figure 5.11: *The spin susceptibility at $U/t = 10.0$ and $\beta t = 2.5$, the formation of the magnetic order is indicated by the enhancement of peak value at $Q = (2\pi/3, 2\pi/3)$.*

In order to know the dominating state in the insulating phase of the triangular lattice, we also calculated the spin susceptibility from the DF method. Fig. 5.10 shows the spin susceptibility at $\beta t = 2.5$ for different interactions. With the increase of interaction strength, the spin susceptibility gradually peaks at wave vector $(2\pi/3, 2\pi/3)$. This means the state which is characterized by the wave vector $2\pi/3$ dominates the system when the Mott gap is open. This state is the 120-degree state. As for the square lattice, we write the dispersion relation Eq. (5.1) as two parts $\epsilon_k = \delta_k + \delta_k^*$ for $t'/t = 1$, where

$$\delta_k = -t(e^{ik_x} + 2e^{-ik_x/2}\cos(\sqrt{3}k_y/2)) \tag{5.3}$$

After simple derivation, we can see that

$$\delta_{k+Q} = \delta_k e^{i2\pi/3} \tag{5.4}$$

with $Q = (2\pi/3, 2\pi/\sqrt{3})$ [Srivastava and Singh (2005)]. Therefore each spin points to each other with 120 degree. The more natural way is to calculate a three site cluster where we can explicitly write down the 120-degree state. By measuring the probability of each state of this three site cluster, we can see which one dominates when the short range order forms. This project is in progress now. Fig. 5.11 shows the 3D plot of the uniform spin susceptibility. The right panel shows the comparison of the spin susceptibility at two different wave vector $(2\pi/3, 2\pi/3)$ and $(0, 0)$. The enhancement of spin susceptibility at $(2\pi/3, 2\pi/3)$ is clearly seen from this diagram.

Compared to the square lattice spin susceptibility whose magnetic state is dominated by the (π, π) antiferromagnetism, here the frustration effect favors the 120-degree state. Thus the transition from (π, π) state to the 120-degree state is expected to exist in the system. In Fig. 5.12 the comparison of the uniform susceptibility for

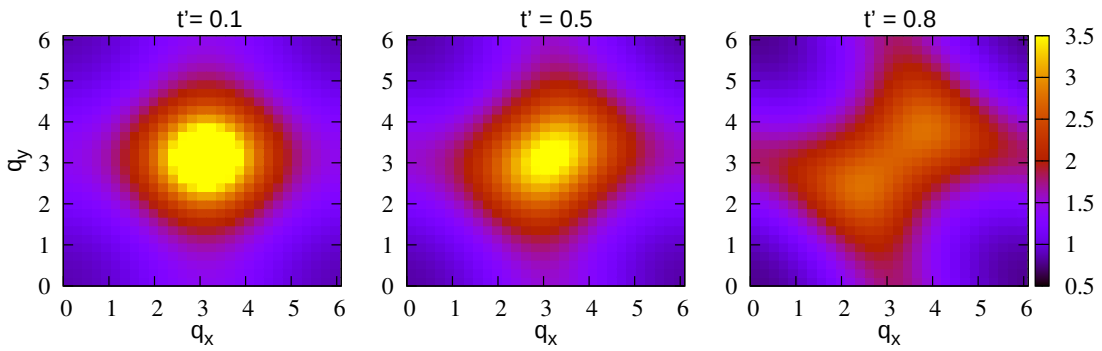

Figure 5.12: *The spin susceptibility for different frustration strength displays the transition from a (π, π) state to a 120-degree state. See context for details of the parameters.*

$\beta t = 2.5$, $U/t = 10$ and three different t'. From right to the left with the decrease of the frustration strength, the peak of the spin susceptibility gradually moves from $(2\pi/3, 2\pi/3)$ to (π, π). It clearly shows the transition from a (π, π) magnetic state to the 120-degree state. Whether it is a clear phase transition or just a crossover is still an open question and needs to be studied carefully. From this diagram, we can observe that the 120-degree state only dominates the system when $t'/t \approx 1$. In our case, $t'/t = 0.8$, the spin susceptibility at (π, π) and $(2\pi/3, 2\pi/3)$ has almost similar values. Thus if it is clear phase transition, the phase boundary between the 120-degree state and (π, π) state must be closer to $t'/t \approx 1$ in the t'/t - U phase diagram.

As a summary, in this chapter we investigated the triangular lattice by using DMFT, C-DMFT, DCA and DF method. The Metal-Insulator transition was observed at different critical interactions in DMFT and the other methods. Frustration destroys the perfect nested Fermi surface of the 2D system which favors the metallic states. But this system is not sufficiently described by a small size cluster, for example here 2×2 cluster was used. The short range order is most probably dominated by the formation of the 120-degree states which needs more careful investigation.

5.2 Bilayer Hubbard Model – Band to Mott Insulator transition

The Hubbard Model on a bilayer has been extensively studied as a toy model of the Hight-Tc superconductor. DMFT and cluster DMFT are also applied to this simple but interesting system. Here is the summary of some conclusions from DMFT calculation.

1. Single site DMFT observes the first-order Metal-Insulator transition.

2. There is coexistence region with lower and upper critical interaction $U_{low}/t \approx 4.7$ and $U_{up}/t \approx 5.5$.

3. Metal to Band insulator transition occurs at weak interaction and strong inter-plane coupling region. It is a second order transition.

4. There is a large deviation for the Metal-Band insulator boundary from finite and zero temperature calculations.

5. There is smooth crossover from Band to Mott insulator transition from single site DMFT calculation in infinite dimension.

6. The direct crossover from Band to Mott insulator was observed in a cluster DMFT calculation at 2D bilayer system.

7. The Mott insulating phase is extended to $U/t = 0$ with the lowering of inter-plane coupling when the short-range fluctuation is included.

From conclusion 3 we can see that in single site DMFT the temperature plays a role in the Metal-Band insulator transition. And the phase boundary between Metal and Band insulator is supposed to move to the smaller inter-plane coupling (which is indicated by $t_\perp$) side. And another important feature is that the anti-ferromagnetic field greatly changes the phase diagram where the metallic phase gradually disappear with the decrease of the inter-layer coupling. In this chapter, we are going to clarify these differences by using the more reliable numerical solver – CTQMC. The single site DMFT equation was solved in the infinite dimension at a very low temperature from which we can understand the temperature effect on the Metal-Band insulator transition. The 2D bilayer Hubbard Model was solved by combining the C-DMFT with CTQMC methods. The paramagnetic metal to insulator transition was observed at finite interaction region even at zero inter-plane coupling case (the two layers are decoupled). Conclusion and outlook is given in the last part of this chapter.

5.2.1 Bilayer Bethe lattice – low temperature investigation

On Bethe lattice each site has a infinite number of neighbors where DMFT becomes exact. Within the single site DMFT method, each layer is replaced by an impurity. The coupling between two layers becomes the hopping between these two impurities. The effective Hubbard action on the bilayer lattice is

$$S^{eff} = \sum_\sigma \Psi^\dagger_\sigma \begin{pmatrix} i\omega_n + \mu & t_\perp \\ t_\perp & i\omega_n + \mu \end{pmatrix} \Psi_\sigma + U \sum_{i=1}^{2} n_{i\uparrow} n_{i\downarrow} - t^2 \sum_\sigma \Psi^\dagger_\sigma \begin{pmatrix} G_{00} & G_{01} \\ G_{10} & G_{11} \end{pmatrix} \Psi_\sigma \tag{5.5}$$

where Ψ is given as $\Psi = (c_1, c_2)^T$. Here, we are going to adapt the strong coupling CTQMC method. As noted, the strong-coupling CTQMC has a simpler form if the one particle part of the local Hamiltonian has a diagonal form. This effective action can be simply diagonalized by the canonical transformation

$$U = \frac{1}{\sqrt{2}} \begin{pmatrix} 1 & 1 \\ -1 & 1 \end{pmatrix} \tag{5.6}$$

The corresponding local Hamiltonian in the new representation is

$$\begin{aligned} H_{loc} &= -(\mu + t_\perp)n_a - (\mu - t_\perp)n_b + \frac{U}{2}(n^a_\uparrow n^a_\downarrow + n^b_\uparrow n^b_\downarrow) + \frac{U}{2}(n^a_\uparrow n^b_\downarrow + n^b_\uparrow n^a_\downarrow) \\ &\quad -\frac{U}{2}(a^\dagger_\uparrow a^\dagger_\downarrow b_\uparrow b_\downarrow + a^\dagger_\downarrow b^\dagger_\uparrow b_\downarrow a_\uparrow + h.c.) \end{aligned} \tag{5.7}$$

Its eigenvalues and eigenvectors have already been given in Chapter 3. Here a and b represent the indices of the new decoupled two planes[1]. This is same as the bond and anti-bond notation in the work of A. Fuhrmann [Fuhramann *et al.* (2006)].

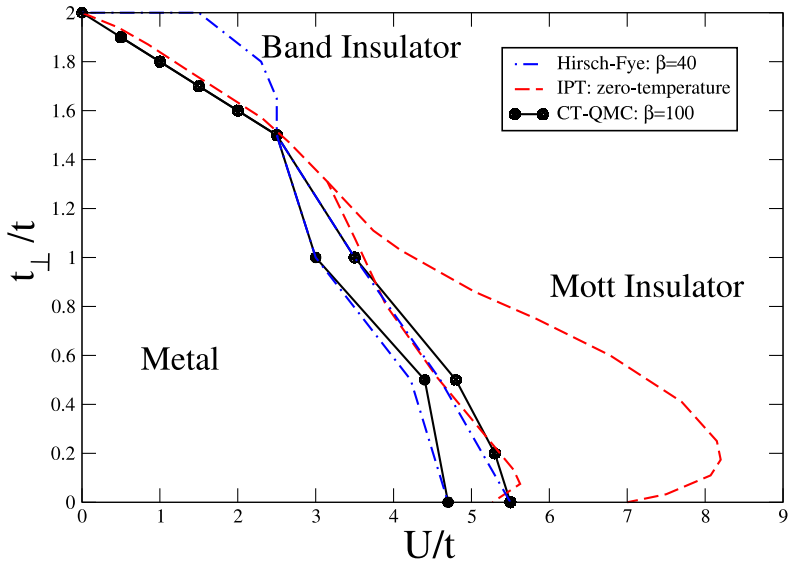

Figure 5.13: *The phase diagram of the bilayer Hubbard model at $\beta t = 100$. The higher temperature and zero temperature phase diagrams are shown as comparison.*

By using both the strong-coupling and weak-coupling CTQMC we solved the above DMFT equation at $\beta t = 100$ for different interaction strengths and inter-plane coupling $t_\perp/t$. This is quite a low temperature compared to the work of A. Fuhrmann [Fuhramann *et al.* (2006)] where $\beta t = 40$ was used. The access of the low temperature region makes the comparison with the zero temperature results more reasonable. As already discussed in the work of A. Fuhrmann, one clear difference between the zero and finite temperature phase diagram is the phase boundary for the Metal to Band Insulator transition. Different positions of the phase boundaries were found. To understand the reason for the difference, the low temperature results will work for this purpose. Fig. 5.13 shows the $t_\perp - U$ phase diagram of the bilayer Hubbard model.

[1]The meaning of "decouple" is that there is no one particle hopping between these two plane, while the density correlation and pairing interaction exist, as one can see from the new Hamiltonian

The blue line was obtained from reference [Fuhramann *et al.* (2006)] and the red line is the zero-temperature results from IPT calculation. The clear Metal to Band and Mott Insulator transition was observed. Our results (black line) are basically similar to the higher temperature Hirsch-Fye results (blue line) except for the smaller interaction and larger $t_\perp$ region where the metal to band insulator transition happened. The boundary of this transition from our calculation is closer to the zero-temperature results. The metal to Mott insulator transition phase boundary also slightly moves to the zero temperature phase boundary, but is not as sensitive to the temperature as that for the metal to band insulator transition.

5.2.2 Bilayer square lattice – CDMFT investigation

The infinite coordination number in each Bethe plane allows us to map each plane with an impurity site exactly. With the lowering of dimensionality, DMFT becomes approximately correct. Some efforts have applied cluster DMFT to the one-dimensional lattice to examine the performance of DMFT. Due to the existence of the exact solution in 1D, it has been taken as benchmark of various cluster methods [Capone *et al.* (2004); Balzer *et al.* (2008)]. Although the single site DMFT fails in the low dimension case, cluster DMFT results are surprisingly in agreement with the Bethe ansatz (BA) solutions. Here, we are going to apply the CDMFT to the bilayer square lattice to study the non-local effect on the phase diagram. We considered a 2×2 cluster in each plane and maped the bilayer system into two coupling CDMFT clusters problem, which can be graphically demonstrated in Fig. 5.14

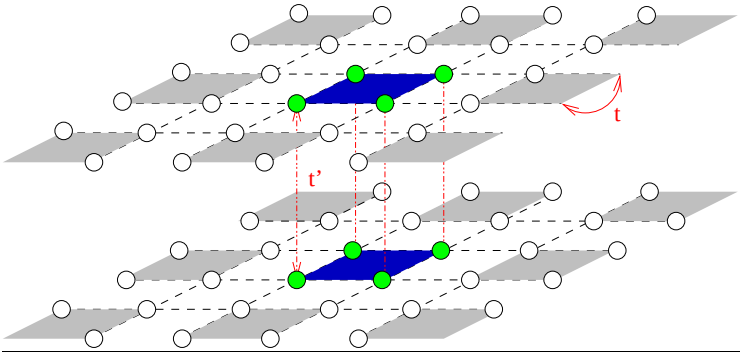

Figure 5.14: *Graphical illustration of the bilayer square lattice with one to one hopping between the two planes. Each layer is viewed as an effective* 2×2 *cluster in CDMFT.*

The inter-plane and intra-plane hopping amplitude are given as t and $t_\perp$. The corresponding hopping matrix for CDMFT is

$$E_k = \begin{pmatrix} -\mu & ty_P & 0 & tx_P & t_\perp & 0 & 0 & 0 \\ ty_N & -\mu & tx_P & 0 & 0 & t_\perp & 0 & 0 \\ 0 & tx_N & -\mu & ty_N & 0 & 0 & t_\perp & 0 \\ tx_N & 0 & ty_P & -\mu & 0 & 0 & 0 & t_\perp \\ t_\perp & 0 & 0 & 0 & -\mu & ty_P & 0 & tx_P \\ 0 & t_\perp & 0 & 0 & ty_N & -\mu & tx_P & 0 \\ 0 & 0 & t_\perp & 0 & 0 & tx_N & -\mu & ty_N \\ 0 & 0 & 0 & t_\perp & tx_N & 0 & ty_P & -\mu \end{pmatrix} \tag{5.8}$$

The short notations $tx_{P/N}$, $ty_{P/N}$ are $-1 - e^{\pm 2ik_x}$, $-1 - e^{\pm 2ik_y}$, respectively. The self

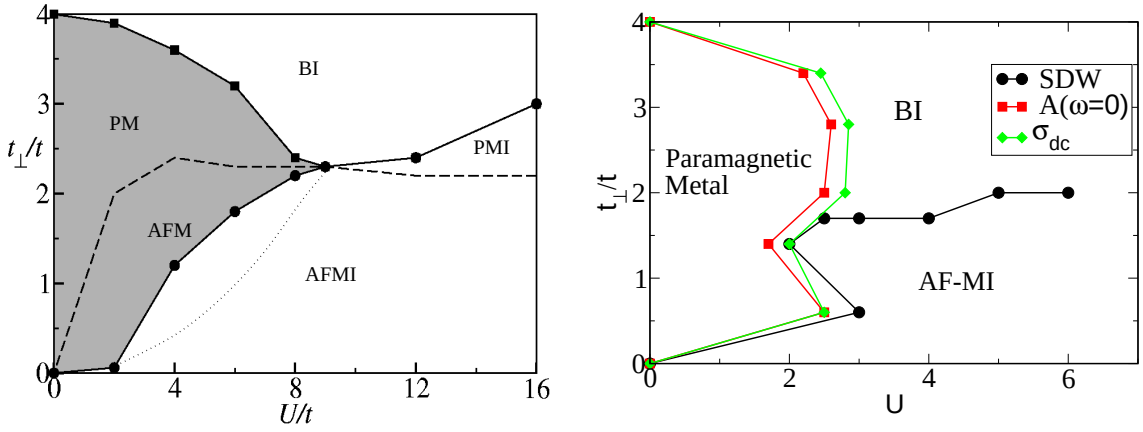

Figure 5.15: *Phase diagrams of the bilayer square lattice from ED-CDMFT (the left panel) and DQMC (right panel).*

---

consistency is done by the following equation together with the Dyson equation.

$$\bar{G}(i\omega_n) = \frac{Lc}{2\pi}\int_{-\frac{\pi}{Lc}}^{\frac{\pi}{Lc}} \frac{dk}{i\omega_n \mathbb{1} - E_k - \bar{\Sigma}(i\omega_n)} \tag{5.9}$$

with $L_c = 2$. Here, the bar on top of the arguments indicates the matrix form. Here in this bilayer model, they are 8×8 matrices which can be understood from the corresponding form of the hopping matrix. Matrix inversion is needed in order to perform the integral of the above equation. Then the Weiss field is obtained by matrix inversion again from the following equation.

$$\bar{\mathcal{G}}_0^{-1}(i\omega) = \bar{\mathcal{G}}^{-1}(i\omega) + \bar{\Sigma}(i\omega) \tag{5.10}$$

Generally, in the whole 8×8 matrix, all the 64 elements go into CT-QMC calculation. Each element should be evaluated independently. The symmetry form of these matrices simplifies our calculation. We do not need to measure all the 64 elements during the simulation, only 6 distinct Green's functions will be measured, three in plane Green's functions and three Green's functions which connect the two layers. Changing from the measurement of 64 elements to 6 elements, the computational burden is greatly reduced. Since all these 6 Green's function have different meaning, they should be accurately measured independently during simulation. For each Green's function, the same number of MC measurement steps is performed. We also can measure all the 64 elements which seems to be tedious at the first glance, while after the simulation we average all the Green's functions which have the same meaning. Therefore, for each different Green's function, we totally sampled $N_{MC} \times f_{symmetry}$ where $f_{symmetry}$ is the symmetry factor of each specific Green's function. For example, in this bilayer model the symmetry factor for the inner-plane nearest neighboring Green's function is 16, for the intra-plane nearest neighboring Green's function it is 8. Both of these two simplification are easily implemented in the simulation. The first method has faster calculating speed and the second one has better accuracy with respect to the same total monte carlo steps. While they are exactly same if we focus on the same sampling number for each Green's function.

The similar C-DMFT equation has been solved in a recent work at zero temperature [Kancharlar and Okamoto (2007)]. A different phase diagram was given, there is no crossover region was found. While with the increase of inter-layer hopping, the interesting 'Mott Insulator - Metal - Band Insulator' transition happens. Further increase the on-site interaction, the metallic phase disappears, the 'Band Insulator - Mott Insulator' transition happens. The determinant QMC (DQMC) also showed a similar phase diagram [Bouadim *et al.* (2008)]. Here we showed the phase diagram obtained from these two works in Fig. 5.15

In the left diagram, the dotted line shows the magnetic phase boundary separating the paramagnetic metal with the anti-ferromagnetic Mott insulator. The shaded portion shows the extent of the metallic region (paramagnetic metal and anti-ferromagnetic metal) in the presence of magnetic order. One significant feature of these phase diagrams is the absence of the metallic phase at smaller inter-layer coupling region, even in the case of no anti-ferromagnetic symmetry breaking field. The paramagnetic metal disappears when $t_\perp/t = 0$. The inclusion of the symmetry breaking field greatly suppresses the metallic phase, as observed in the square lattice. If we focus on the paramagnetic phase, the metallic state is favored. A recent CDMFT study shows that there is phase transition between the paramagnetic Metal to paramagnetic Mott insulator in the square lattice [Park *et al.* (2008)]. This phase diagram is shown in Fig. 5.16.

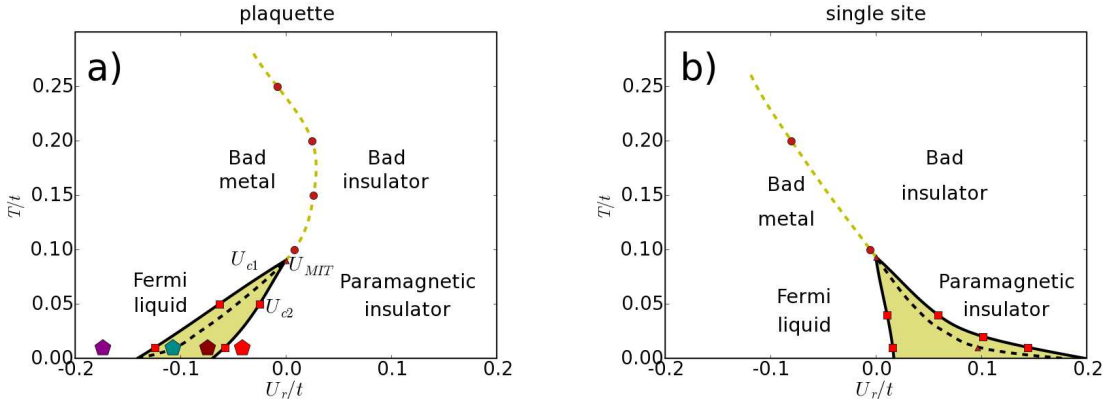

Figure 5.16: *$T-U$ phase diagram of 2D square lattice, the paramagnetic metal to Mott insulator transition happens at both a single site DMFT calculation (b) and a plaquette CDMFT calculation (a). Here $U_r = \frac{U-U_{MIT}}{U_{MIT}}$, with $U_{MIT} = 6.05t$ in cluster case and $U_{MIT} = 9.35t$ in single site case.*

In both the single site and plaquette case, the Metal-Insulator transition was observed in the absence of magnetic order. Therefore it is reasonable to expect that in the bilayer system with the decrease of inter-layer coupling, the paramagnetic metal can exist in finite interaction region in the case of no external symmetry breaking field. And when $t_\perp/t$ becomes zero, the similar critical U_{MIT} should be reproduced since the two layers are completely decoupled. This is the case we observed from our CTQMC-CDMFT calculation. In Fig. 5.17 the sketch of the finite temperature phase diagram is shown. The paramagnetic Metal - Insulator transition occurs at finite interaction region. The phase is determined from the

local Green's function by comparing the values corresponding to the lowest two frequency points. We identified it as insulating phase when $G(i\omega_1)$ becomes same or smaller than $G(i\omega_2)$ (here, ω_1 and ω_2 are the two lowest frequency points). We only have the results at some special parameters shown as empty and solid squares in the figure. But basically the phase boundary can be estimated from these results. Obviously, more carefully calculation and more parameters need to be examined. The initial cluster self-energy was always set to zero which corresponds to start from the metallic region. Therefore the critical U_c given here corresponds to the upper critical U_{c2}. We believe that the coexistence region exist in our calculation, which can be determined by using the insulating initial Weiss field. With the decreasing of $t_\perp/t$, the two layers are gradually decoupled. When $t_\perp/t = 0$, it should generate the same physics as the single layer square lattice.

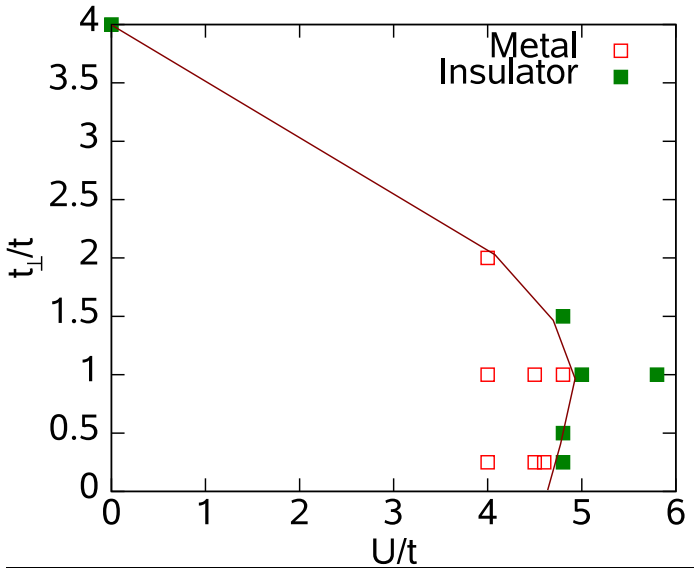

Figure 5.17: *The finite temperature phase diagram obtained from CDMFT. Each layer is viewed as effective* 2 *cluster. The finite critical interaction U_c was observed, even for $t_\perp/t = 0$.*

In Fig. 5.16, there is coexistence region when $\beta t \leq 10$. In our calculation, we set $\beta t = 20$ which is within the coexistence region. Thus the coexistence of the metallic and insulating solutions at smaller $t_\perp/t$ is favorable. The investigation is in progress. From our sketch of the phase diagram, we can see that the critical interaction U_c at $t_\perp/t = 0$ is smaller than the prediction from a plaquette CDMFT calculation (see Fig. 5.16). We believe it is due to the non-local effect. From the comparison of the single site and plaquette calculation, we can see that the inclusion of the short range correlation within a 2×2 cluster reduces the critical U from $9.35t$ to $6.05t$. Here the extra dimensionality in z direction introduce more spatial fluctuation than the single layer, therefore the critical interaction U_c becomes smaller.

In conclusion, in this section we examined the bilayer Hubbard model by using CTQMC with single site DMFT and CDMFT to understand the phase diagram. The low temperature phase diagram generated a large correction to the phase boundary of the Metal - Band insulator transition. The finite temperature CDMFT calculation shows qualitatively similar results compared to the single layer plaquette calculation, where the finite critical interaction was observed. More calculations are being performed to determine the coexistence region and precise phase transition boundary.

Chapter 6

Summary

To characterize the interaction driven nature of the metal - insulator transition in the strongly correlated electron systems, an efficient theory which can equally access the weak and strong coupling region is required. Dynamical mean field theory provides an exact solution of the electron models in the infinite dimension limit. The single impurity nature of this method reduces the full self energy to a function which is independent of momentum. The local fluctuation is fully included in this theory, the non-local spatial correlation is treated as mean field. To study the finite dimension systems, the non-local fluctuation effect should be taken into account.

In this thesis, we mainly studied the contributions of the non-local fluctuation to the single site dynamical mean field theory. Starting from solving the simple atomic Hubbard model, we illustrated the basic properties of the metal - insulator transition. The exact partition function was calculated and used to determine the total energy, local moment and the one particle Green's function. These observables can be used to characterize different phases. The introduction of the dynamical mean field theory started from the cavity construction. The separation of the impurity degrees of freedom with the remaining of the lattice reduced the total action into three parts, corresponding to the impurity, bath and the hybridization term. The Gaussian form of the bath action allows us to integrate out the bath degrees of freedoms explicitly. The expansion over the hybridization term yields a Taylor series. By the dimensionality analysis, we showed that only the second order term was non-zero in the infinite coordination number limit. In the second part of this chapter, we showed the cluster extensions of the dynamical mean field theory. Cellular DMFT and DCA were formulated in real space in order to show the similarity and difference between them. The real space formulation of DCA can be transformed to the widely used momentum space formula by diagonalization of the dispersion relation. Being an example, the fully frustrated 2D square lattice calculation was then implemented in Cellular DMFT and DCA in a 2×2 cluster. The frustration destroyed the perfect nested Fermi surface.

The recently proposed continuous-time Quantum Monte Carlo method was reviewed in detail. Both the weak and strong-coupling CTQMC were discussed. Both the theoretical and technical details were presented. The implementation of CTQMC as impurity solver for single site DMFT and cluster DMFT were both discussed. In the strong-coupling CTQMC, the simulation of the single site multi-band

model with only the density - density interaction term can be greatly accelerated by introducing the segment notation. The performance of CTQMC was illustrated in the example of two plane Hubbard model.

The applicability of the cluster extensions of DMFT suffers two problems: (1) the correlation length is restricted to the finite range ; (2) the computation is expensive for larger cluster calculation. To go beyond the short range corrections of DMFT, we considered the dual fermion method which can equally take the short and long range fluctuation effect into account. The detailed derivation of the dual fermion method was given. The approximation introduced in this method was also discussed. The introducing of the dual fermion allows us to solve a many-body interacting problem in two steps. First to solve the local self energy function from single site DMFT and then to get the non-local information from solving the dual fermion systems. This allows us to access both the short and long range correlation effect on equal footing. The non-local correction to the single particle Green's function was discussed. Then the dual fermion nature was studied by calculating the dual fermion susceptibility. The divergence in the dual fermion susceptibility also happened in the lattice susceptibility, indicating the similarity of the lattice and dual fermions. The lattice susceptibility obtained from the dual fermion method was in good agreement with the lattice QMC solution. Another interesting method, namely dynamical vertex approximation, was also discussed and compared with the dual fermion method. Due to the absence of local information of the dual fermion, it has a better convergence nature than the dynamical vertex approximation. The DF method demonstrated its advantages in solving the weak and very strong interaction systems.

The application of the dual fermion method in the triangular lattice showed the great advantage of this method. The single particle Green's function calculated from the dual fermion method showed the better coincidence with the larger cluster solution. The frustration in the triangular lattice greatly suppressed the anti-ferromagnetic order, which favors the existence of the metallic phase. The first order metal - insulator transition was observed from the jump of the double occupancy. The temperature effect on the critical U in the single site DMFT was analyzed. The magnetic phase transition was observed from the movement of the peak position of the lattice spin susceptibility. With the increase of the lattice frustration, the magnetic phase gradually moved from anti-ferromagnetic state to the 120-degree state. Both of these two states were inside the insulating phase. The paramagnetic metal to paramagnetic insulator transition was also studied in a bilayer Hubbard model. The single site and Cellular DMFT gave similar phase diagrams. The first order metal - insulator transition and the coexistence region were observed. The phase boundary for the metal to band insulator transition was greatly changed by lowering temperature. More calculations are needed to complete the phase diagram in Cellular DMFT calculation.

Appendix A

Fast Update Algorithm for CT-QMC

Normally, in the fast update procedure we only store and manipulate the inverse of D-matrix (Rubtsov *et al.* (2005)) and F-matrix (Werner *et al.* (2005); Werner and Millis (2006)). Here we use G to represent this matrix and M for its inverse matrix. The following procedure can be used to generate a new M-matrix from the old one easily which represents the movement of perturbation order.

Supposed we have one k-dimensional M-matrix. Its inverse matrix is G. They have the following form:

$$G^{(k)} = \begin{pmatrix} G_{1,1} & G_{1,2} & \cdots & G_{1,k} \\ G_{2,1} & G_{2,2} & \cdots & G_{2,k} \\ \cdots & \cdots & \cdots & \cdots \\ G_{k,1} & G_{k,2} & \cdots & G_{k,k} \end{pmatrix} \tag{A.1}$$

and

$$M^{(k)} = \begin{pmatrix} M_{1,1} & M_{1,2} & \cdots & M_{1,k} \\ M_{2,1} & M_{2,2} & \cdots & M_{2,k} \\ \cdots & \cdots & \cdots & \cdots \\ M_{k,1} & M_{k,2} & \cdots & M_{k,k} \end{pmatrix} \tag{A.2}$$

In order to move k to $k+1$, M and G matrices will be inserted in a new column and row. In Rubtsov's method, the new inserted pair locates at the last column and row of G matrix. Except that the $G_{k+1,K+1}$ and $M_{k+1,k+1}$ are one, all the other new elements are zero. Note that these inserted column and row do not change the determinants of the these two matrices. In Werner's method, the operation is different. If one considers inserting a new segment, the index of the new position can be anywhere from 1 to $k+1$ and the new column and row have the same position index. To insert new anti-segment, one needs to be careful with the position of the new row and column. If one insert a new row indexed by n then the new column index will be $n+1$. For generality, I just consider the situation that the new row position is m and new column position is n. Corresponding to Rubsov's method, one just need to take $m = n = k+1$, and to Werner's method, $n = m+1$. Note that in any case, the determinant is not changed. Based on the above considerations,

one can write G and M matrices as:

$$G^{(k)} = \begin{array}{c} \\ m \end{array} \begin{array}{c} \begin{array}{ccccccc} & & & & n & & \end{array} \\ \begin{pmatrix} G'_{1,1} & G'_{1,2} & \cdots & 0 & \cdots & G'_{1,k} \\ G'_{2,1} & G'_{2,2} & \cdots & 0 & \cdots & G'_{2,k} \\ \cdots & \cdots & \cdots & 0 & \cdots & \cdots \\ 0 & 0 & \cdots & 1 & \cdots & 0 \\ \cdots & \cdots & \cdots & 0 & \cdots & \cdots \\ G'_{k+1,1} & G'_{k+1,2} & \cdots & 0 & \cdots & G'_{k+1,k+1} \end{pmatrix} \end{array} \tag{A.3}$$

and

$$M^{(k)} = \begin{array}{c} \\ n \end{array} \begin{array}{c} \begin{array}{ccccccc} & & & & m & & \end{array} \\ \begin{pmatrix} M'_{1,1} & M'_{1,2} & \cdots & 0 & \cdots & M'_{1,k} \\ M'_{2,1} & M'_{2,2} & \cdots & 0 & \cdots & M'_{2,k} \\ \cdots & \cdots & \cdots & 0 & \cdots & \cdots \\ 0 & 0 & \cdots & 1 & \cdots & 0 \\ \cdots & \cdots & \cdots & 0 & \cdots & \cdots \\ M'_{k+1,1} & M'_{k+1,2} & \cdots & 0 & \cdots & M'_{k+1,k+1} \end{pmatrix} \end{array} \tag{A.4}$$

Where, for $i > m$, $G'_{i,j} = G_{i-1,j}$; for $j > n$, $G'_{i,j} = G_{i,j-1}$. And for all the other elements $G'_{i,j} = G_{i,j}$. For the M-matrix, one should notice that the inserted new column is n and new row is m since M-matrix is the inverse matrix of G-matrix. The relation between the elements of the new and old matrix is that: $i > n$, $M'_{i,j} = M_{i-1,j}$; for $j > m$, $M'_{i,j} = M_{i,j-1}$. And for all the other elements $M'_{i,j} = M_{i,j}$.

$$G^{(k+1)} = \begin{array}{c} \\ m \end{array} \begin{array}{c} \begin{array}{ccccccc} & & & & n & & \end{array} \\ \begin{pmatrix} G'_{1,1} & G'_{1,2} & \cdots & G'_{1,n} & \cdots & G'_{1,k} \\ G'_{2,1} & G'_{2,2} & \cdots & G'_{2,n} & \cdots & G'_{2,k} \\ \cdots & \cdots & \cdots & G'_{i,n} & \cdots & \cdots \\ G'_{m,1} & G'_{m,2} & \cdots & G'_{m,n} & \cdots & G'_{m,k+1} \\ \cdots & \cdots & \cdots & G'_{j,n} & \cdots & \cdots \\ G'_{k+1,1} & G'_{k+1,2} & \cdots & G'_{k+1,n} & \cdots & G'_{k+1,k+1} \end{pmatrix} \end{array} \tag{A.5}$$

Here, we use the notation in reference (Rubtsov *et al.* (2005)) to derive the fast update formulas.

$$\Delta = M^{-1}_{(k+1)} - M_{(k)} = G^{(k+1)} - G^{(k)} \tag{A.6}$$

From the above forms of $G^{(k+1)}$ and $G^{(k)}$, one can easily write down that

$$\Delta = \begin{array}{c} \\ m \end{array} \begin{array}{c} \begin{array}{ccccccc} & & & & n & & \end{array} \\ \begin{pmatrix} 0 & 0 & \cdots & G'_{1,n} & \cdots & 0 \\ 0 & 0 & \cdots & G'_{2,n} & \cdots & 0 \\ \cdots & \cdots & \cdots & G'_{i,n} & \cdots & \cdots \\ G'_{m,1} & G'_{m,2} & \cdots & G'_{m,n} - 1 & \cdots & G'_{m,k+1} \\ \cdots & \cdots & \cdots & G'_{j,n} & \cdots & \cdots \\ 0 & 0 & \cdots & G'_{k+1,n} & \cdots & 0 \end{pmatrix} \end{array} \tag{A.7}$$

This is also a $(k+1)\times(k+1)$ matrix and only the m row, n column elements are nonzero. Now, combining the expression of M-matrix, one easily obtains

$$
\begin{aligned}
& 1+\Delta M \\
= \; & 1+\begin{pmatrix} 0 & 0 & \cdots & G'_{1,n} & \cdots & 0 \\ 0 & 0 & \cdots & G'_{2,n} & \cdots & 0 \\ \cdots & \cdots & \cdots & G'_{i,n} & \cdots & \cdots \\ G'_{m,1} & G'_{m,2} & \cdots & G'_{m,n}-1 & \cdots & G'_{m,k+1} \\ \cdots & \cdots & \cdots & G'_{j,n} & \cdots & \cdots \\ 0 & 0 & \cdots & G'_{k+1,n} & \cdots & 0 \end{pmatrix} \times \\
& \begin{pmatrix} M'_{1,1} & M'_{1,2} & \cdots & 0 & \cdots & M'_{1,k} \\ M'_{2,1} & M'_{2,2} & \cdots & 0 & \cdots & M'_{2,k} \\ \cdots & \cdots & \cdots & 0 & \cdots & \cdots \\ 0 & 0 & \cdots & 1 & \cdots & 0 \\ \cdots & \cdots & \cdots & 0 & \cdots & \cdots \\ M'_{k+1,1} & M'_{k+1,2} & \cdots & 0 & \cdots & M'_{k+1,k+1} \end{pmatrix}
\end{aligned}
\tag{A.8}
$$

After the production of these two matrices, one will get a new matrix whose nonzero elements are at m column and m row.

$$
1+\Delta M = \begin{matrix} \\ m \end{matrix}\begin{matrix} \begin{matrix} \quad & \quad & \quad & m & \quad & \quad \end{matrix} \\ \begin{pmatrix} 1 & 0 & \cdots & G'_{1,n} & \cdots & 0 \\ 0 & 1 & \cdots & G'_{2,n} & \cdots & 0 \\ \cdots & \cdots & \cdots & G'_{i,n} & \cdots & \cdots \\ R_{m,1} & R_{m,2} & \cdots & G'_{m,n} & \cdots & R_{m,k+1} \\ \cdots & \cdots & \cdots & G'_{j,n} & \cdots & \cdots \\ 0 & 0 & \cdots & G'_{k+1,n} & \cdots & 1 \end{pmatrix} \end{matrix}
\tag{A.9}
$$

Here, $R_{m,j}=\sum_{i\neq n} G'_{m,i}M'_{i,j}$. One should notice that this is a matrix whose diagonal elements are one except the m-th row and the m-th column element is $G'_{m,n}$. Especially, the n-th column in $G^{(k+1)}$ has been changed to the m-th column in this matrix. $1+\Delta M$ can be very useful to calculate the determinant ratio between $G^{(k+1)}$ and $G^{(k)}$. Since $\Delta = M^{-1}_{(k+1)} - M^{-1}_{(k)}$, one can know that $M_{(k+1)} = M_{(k)}[1+\Delta M_{(k)}]^{-1}$.The determinant ratio can be expressed as:

$$
\frac{\mathcal{Z}_{(k+1)}}{\mathcal{Z}_{(k)}} = \frac{\det G_{(k+1)}}{\det G_{(k)}} = \frac{\det M_{(k)}}{\det M_{(k+1)}} = \det[1+\Delta M_k] = G'_{m,n} - \sum_{i\neq m} R_{m,i}G'_{i,n} \tag{A.10}
$$

Later on, one can know that this determinant ratio is just $1/M^{(k+1)}_{n,m}$. This determinant ratio is important for determining the detailed balance condition, therefore the update ratio. In order the obtain $M^{(k+1)}$, one needs to calculate the inverse of $1+\Delta M$, it looks like that we cannot avoid the inverse operation which is always time consuming for numerical calculation. Fortunately, after the above operation, what we need to inverse is a special matrix which has few nonzero elements. It is significantly easier than the inversion of general matrix. The inverse of $1+\Delta M$ can

be obtained similarly from a 2 × 2 matrix.

$$\begin{pmatrix} 1 & B \\ C & D \end{pmatrix}^{-1} = \begin{pmatrix} (1-BD^{-1}C)^{-1} & -(1-BD^{-1}C)^{-1}BD^{-1} \\ -(D-CB)^{-1}C & (D-CB)^{-1} \end{pmatrix} \qquad \text{(A.11)}$$

The first row can be simplified as:

$$\begin{aligned} (1-BD^{-1}C)^{-1}-1 &= (1-BD^{-1}C)^{-1}\times(1-1+BD^{-1}C) \\ &= (1-BD^{-1}C)^{-1}BD^{-1}C \\ &= [C^{-1}DB^{-1}(1-BD^{-1}C)]^{-1} \\ &= [C^{-1}DB^{-1}-1]^{-1} = B(D-CB)^{-1}C \qquad \text{(A.12)} \end{aligned}$$

$$(1-BD^{-1}C)^{-1}BD^{-1} = [DB^{-1}(1-BD^{-1}C)]^{-1} = (DB^{-1}-C)^{-1} = B(D-CB)^{-1} \qquad \text{(A.13)}$$

Now, replacing these two expressions into the 2 × 2 matrix, one obtains

$$\begin{pmatrix} 1 & B \\ C & D \end{pmatrix}^{-1} = \begin{pmatrix} 1+B(D-CB)^{-1}C & -B(D-CB)^{-1} \\ -(D-CB)^{-1}C & (D-CB)^{-1} \end{pmatrix} \qquad \text{(A.14)}$$

To calculate the inverse matrix of $1+\Delta M$, one only needs to replace C with M, B with G and $D-CB$ with $G'_{m,n}-\sum_{i\neq m} R_{m,i}G'_{i,n} = \lambda = \alpha^{-1}$

$$[1+\Delta M_{(k)}]^{-1} =$$

$$\begin{array}{cc} & \begin{array}{cccccc} \phantom{1+G'_{1,n}\alpha R_{m,1}} & \phantom{1+G'_{2,n}\alpha R_{m,2}} & & m & & \phantom{1+G'_{k+1,n}\alpha R_{m,k+1}} \end{array} \\ m & \left(\begin{array}{cccccc} 1+G'_{1,n}\alpha R_{m,1} & G'_{1,n}\alpha R_{m,2} & \cdots & -G'_{1,n}\alpha & \cdots & G'_{1,n}\alpha R_{m,k+1} \\ G'_{2,n}\alpha R_{m,1} & 1+G'_{2,n}\alpha R_{m,2} & \cdots & -G'_{2,n}\alpha & \cdots & G'_{2,n}\alpha R_{m,k+1} \\ \cdots & \cdots & \cdots & -G'_{i,n}\alpha & \cdots & \cdots \\ -\alpha R_{m,1} & -\alpha R_{m,2} & \cdots & \alpha & \cdots & -\alpha R_{m,k+1} \\ \cdots & \cdots & \cdots & -G'_{j,n}\alpha & \cdots & \cdots \\ G'_{k+1,n}\alpha R_{m,1} & G'_{k+1,n}\alpha R_{m,2} & \cdots & -G'_{k+1,n}\alpha & \cdots & 1+G'_{k+1,n}\alpha R_{m,k+1} \end{array}\right) \end{array} \qquad \text{(A.15)}$$

Note again that except that the m-th column and m-th row elements have different expressions, all the other rows and columns have similar forms. And from the for-

mula $M_{(k+1)} = M_{(k)}[1 + \Delta M_{(k)}]^{-1}$,one can obtain the corresponding $M_{(k+1)}$-matrix.

$$M_{(k+1)} = M_{(k)}[1 + \Delta M_{(k)}]^{-1} = \begin{pmatrix} M'_{1,1} & M'_{1,2} & \cdots & 0 & \cdots & M'_{1,k} \\ M'_{2,1} & M'_{2,2} & \cdots & 0 & \cdots & M'_{2,k} \\ \cdots & \cdots & \cdots & 0 & \cdots & \cdots \\ 0 & 0 & \cdots & 1 & \cdots & 0 \\ \cdots & \cdots & \cdots & 0 & \cdots & \cdots \\ M'_{k+1,1} & M'_{k+1,2} & \cdots & 0 & \cdots & M'_{k+1,k+1} \end{pmatrix} \times$$

$$\begin{pmatrix} 1 + G'_{1,n}\alpha R_{m,1} & G'_{1,n}\alpha R_{m,2} & \cdots & -G'_{1,n}\alpha & \cdots & G'_{1,n}\alpha R_{m,k+1} \\ G'_{2,n}\alpha R_{m,1} & 1 + G'_{2,n}\alpha R_{m,2} & \cdots & -G'_{2,n}\alpha & \cdots & G'_{2,n}\alpha R_{m,k+1} \\ \cdots & \cdots & \cdots & -G'_{i,n}\alpha & \cdots & \cdots \\ -\alpha R_{m,1} & -\alpha R_{m,2} & \cdots & \alpha & \cdots & -\alpha R_{m,k+1} \\ \cdots & \cdots & \cdots & -G'_{j,n}\alpha & \cdots & \cdots \\ G'_{k+1,n}\alpha R_{m,1} & G'_{k+1,n}\alpha R_{m,2} & \cdots & -G'_{k+1,n}\alpha & \cdots & 1 + G'_{k+1,n}\alpha R_{m,k+1} \end{pmatrix}$$

$$= \begin{matrix} \\ n \end{matrix} \begin{pmatrix} & & & \overset{m}{} & & \\ M'_{1,1}+L_{1,n}\alpha R_{m,1} & M'_{1,2}+L_{1,n}\alpha R_{m,2} & \cdots & -L_{1,n}\alpha & \cdots & M'_{1,k+1}+L_{1,n}\alpha R_{m,k+1} \\ M'_{2,1}+L'_{2,n}\alpha R_{m,1} & M'_{2,2}+L'_{2,n}\alpha R_{m,2} & \cdots & -L_{2,n}\alpha & \cdots & M'_{2,k+1}+L_{2,n}\alpha R_{m,k+1} \\ \cdots & \cdots & \cdots & -L_{i,n}\alpha & \cdots & \cdots \\ -\alpha R_{m,1} & -\alpha R_{m,2} & \cdots & \alpha & \cdots & -\alpha R_{m,k+1} \\ \cdots & \cdots & \cdots & -L_{j,n}\alpha & \cdots & \cdots \\ M'_{k+1,1}+L_{k+1,n}\alpha R_{m,1} & M'_{k+1,2}+L_{k+1,n}\alpha R_{m,2} & \cdots & -L_{k+1,n}\alpha & \cdots & M'_{k+1,k+1}+L_{k+1,n}\alpha R_{m,k+1} \end{pmatrix}$$

Except for the n-th row and m-th column, all the other elements have the similar form which can be expressed as

$$M_{i,j}^{(k+1)} = M_{i,j}^{(k)} + L_{i,n}\alpha R_{m,j} \tag{A.16}$$

here,$i, j \in (1, k+1)$, but $i, j \neq m$. And $L_{i,n} = \sum_{j \neq m} M'_{i,j} G'_{j,n}$. From these expressions, one also can know the fast update formula from $k- > k-1$

$$M_{i,j}^{(k+1)} = M_{i,j}^{(k)} + \frac{M_{i,m}^{(k+1)} M_{n,j}^{(k+1)}}{M_{n,m}^{(k+1)}} \tag{A.17}$$

therefore

$$M_{i,j}^{(k-1)} = M_{i,j}^{(k)} - \frac{M_{i,m}^{(k)} M_{n,j}^{(k)}}{M_{n,m}^{(k+1)}} \tag{A.18}$$

And the determinant ratio can be expressed as:

$$\frac{\mathcal{Z}^{(k-1)}}{\mathcal{Z}^{(k)}} = \frac{\det G^{(k-1)}}{\det G^{(k)}} = \frac{\det M^{(k)}}{\det M^{(k-1)}} = M_{n,m}^{(k)} \tag{A.19}$$

Appendix B

Direct CT-QMC measurement in frequency space

The imaginary frequency Green's function can be obtained from the Fourier transform of $G(\tau)$. Both weak and strong coupling methods can measure the Green's function directly in frequency space. Since the value of $G(\tau)$ is measured from the corresponding 'M matrix', it seems that the measurement speed is proportional to the square of 'M matrix' dimension. In fact, it can be done in a more economical way where only linear time is needed.

Take strong-coupling method as example. The imaginary Green's function is calculated as follows:

$$G(i\omega_n) = \frac{1}{\beta} \sum_{i,j} e^{-i\omega_n \tau_i^s} M(i,j) e^{i\omega_n \tau_j^e} \tag{B.1}$$

The sum runs over the row and column index of 'M-matrix', which is not economical when the matrix size is big. In fact, the Fourier transform can be performed in every monte Cairo update procedure instead of in the final measurement part. This means the new Green's function is recalculated only when the update is accepted. Otherwise it takes the old value. And the calculation burden can be reduced further by saving the imaginary frequency Green's function. For every different update procedure, one has different way to implement it. For example, we consider to insert a new pair of kinks, 'M matrix' size is increased by one $k \to k+1$. And suppose that the new inserted row and column are at $(k+1, k+1)$. The new and old Green's function are

$$G^{New}(i\omega_n) = \frac{1}{\beta} \sum_{i,j}^{k+1} e^{-i\omega_n \tau_i^s} M^{New}(i,j) e^{i\omega_n \tau_j^e} \tag{B.2}$$

$$G^{Old}(i\omega_n) = \frac{1}{\beta} \sum_{i,j}^{k} e^{-i\omega_n \tau_i^s} M^{Old}(i,j) e^{i\omega_n \tau_j^e} \tag{B.3}$$

Since only one row and column inserted, one can relate the new 'M matrix' with the old one. Eventually, the imaginary Green's function can be calculated from the old

one. This is the key idea of frequency measurement. The difference of the new and old Green's function is

$$\begin{aligned} G^{New} - G^{Old} &= \frac{1}{\beta}\sum_{i,j}^{k} e^{-i\omega_n \tau_i^s}(M^{New}(i,j) - M^{Old}(i,j))e^{i\omega_n \tau_j^e} \\ &+\frac{1}{\beta}\sum_{j=1}^{k} e^{-i\omega_n \tau_{k+1}^s} M(k+1,j)e^{i\omega_n \tau_j^e} \\ &+\frac{1}{\beta}\sum_{i=1}^{k} e^{-i\omega_n \tau_i^s} M(i,k+1)e^{i\omega_n \tau_{k+1}^e} \\ &+\frac{1}{\beta}e^{-i\omega_n \tau_{k+1}^s} M(k+1,k+1)e^{i\omega_n \tau_{k+1}^e} \end{aligned} \tag{B.4}$$

List of Figures

References

Abrikosov, A., L. Gorkov, and I. Dzyaloshinski, 1963, *Methods of quantum field theory in statistical physics* (Dover, New York, N.Y.). 51, 56

Allen, S., and A.-M. Tremblay, 1995, J. Phys. Chem. Solids (UK) **56**, 1769. 9

Aryanpour, K., W. Pickett, and R. Scalettar, 2006, Phys. Rev. B **74**, 085117. 72, 73, 74

Assaad, F., and T. Lang, 2007, Phys. Rev. B **76**, 035116. 31

Balzer, M., W. Hanke, and M. Potthoff, 2008, Phys. Rev. B **77**, 045133. 83

Bernu, B., P. Lecheminant, C. Lhuillier, and L. Pierre, 1994, Phys. Rev. B **50**, 10048. 72

Bickers, N. E., D. J. Scalapino, and S. R. White, 1989, Phys. Rev. Lett. **62**, 961. 9

Bickers, N. E., and S. R. White, 1991, Phys. Rev. B **43**, 8044. 9, 61, 99

Bouadim, K., G. Batrouni, F. Hebert, and R. Scalettst, 2008. 85

Brener, S., H. Hafermann, A. Rubtsov, M. Katsnelson, and A. Lichtenstein, 2008, Phys. Rev. B **77**, 195105. 57, 59

Capone, M., M. Civelli, S. S. Kancharla, C. Castellani, and G. Kotliar, 2004, Phys. Rev. B **69**, 195105. 83

Capriotti, L., A. E. Trumper, and S. Sorella, 1999, Phys. Rev. B **82**, 3899. 72

Chen, L., and A.-M. S. Tremblay, 1993, Phys. Rev. B **49**, 4338. 68

Coldea, R., D. Tennant, and Z. Tylcznski, 2003, Phys. Rev. B **68**, 134424. 71

Fuhramann, A., D. Heilmann, and H. Monien, 2006, Phys. Rev. B **73**, 245118. 82, 83

Georges, A., G. Kotliar, W. Krauth, and M. J. Rozenberg, 1996, Rev. Mod. Phys. **68**, 13. 1, 9, 51

Hafermann, H., S. Brener, A. N. Rubtsov, M. I. Katsnelson, and A. I. Lichtenstein, 2007, Pis'ma v ZhETF **86**, 769. 52, 62

Haule, K., 2007, Phys. Rev. B **75**, 155103. 32

Held, K., A. A. Katanin, and A. Toschi, 2008, arXiv:0807.1860. 67

Hettler, M. H., M. Mukherjee, M. Jarrell, and H. R. Krishnamurthy, 2000, Phys. Rev. B **61**, 12739. 18

Honchkeppel, S., F. Assaad, and W. Hanke, 2008, cond-mat/0801.3377. 69

Hubbard, J., 1963, Proc. Roy. Soc. London A **276**, 238. 1

Huse, D., and V. Elser, 1988, Phys. Rev. Lett. **60**, 2531. 72

Imai, Y., and N. Kawakami, 2002, Phys. Rev. B **65**, 233103. 72

Jarrell, M., 1992, Phys. Rev. Lett. **69**, 168. 15

Kancharlar, S. S., and S. Okamoto, 2007, Phys. Rev. B **75**, 193103. 85

Katanin, A. A., A. Toschi, and K. Held, 2008, arXiv:0808.0689. 67

Kotliar, G., S. Savrasov, G. Pallson, and G. Biroli, 2001, Phys. Rev. Lett. **87**, 186401. 18

Kusunose, H., 2007, J. Phys. Soc. Jpn. **75**, 054713. 47

Kyung, B., G. Kotliar, and A.-M. Tremblay, 2006, Phys. Rev. B **73**, 205106. 22

Maier, T., M. Jarrell, T. Pruschke, and M. H. Hettler, 2005, Rev. Mod. Phys. **77**, 1027. 2, 18, 19

Merino, J., B. Powell, and R. McKenzie, 2006, Phys. Rev. B **73**, 235107. 73

Metzner, W., and D. vollhardt, 1989, Phys. Rev. Lett. **62**, 324. 9

Moreo, A., 1993, Phys. Rev. B **48**, 3380. 60, 61, 65, 68, 69, 99

Mott, N., 1968, Rev. Mod. Phys. **40**, 677. 1

Mueller-Hartmann, E., 1984, Z. Phys. B **57**, 281. 9

Nozieres, P., 1964, *Theory of interacting fermi systems* (W. A. Benjamin, INC., New York. New York). 56, 57

Ohashi, T., T. Momoi, H. Tsunetsugu, and N. Kawakami, 2008, Phys. Rev. Lett. **100**, 076402. 72

Okamoto, S., A. Millis, H.Monien, and A. Fuhrmann, 2003, Phys. Rev. B **68**, 195121. 18

Park, H., K. Haule, and G. Kotliar, 2008, arXiv:0803.1324. 85

Potthoff, M., 2003, Eur. Phys. J. B **36**, 335. 18

Rice, T., and D. McWhan, 1970, IBM J. Res. Develop , 251. 1

Rubtsov, A. N., M. I. Katsnelson, and A. I. Lichtenstein, 2008, Phys. Rev. B **77**, 033101. 47, 50, 52

Rubtsov, A. N., v. v. Savkin, and A. I. Lichtenstein, 2005, Phys. Rev. B **72**, 045128. 25, 26, 89, 90

Shimizu, Y., K. Miyagawa, K. Kanoda, M. Maesato, and G. Saito, 2003, Phys. Rev. Lett. **91**, 107001. 71, 99

Slezak, C., M. Jarrell, T. Maier, and J. Deisz, 2006, cond-mat/0603421. 47

Srivastava, P., and V. Singh, 2005, Phys. Rev. B **72**, 224409. 79

Stanescu, T. D., and G. Kotliar, 2006, Phys. Rev. B **74**, 125110. 22

Tamura, M., and R. Kato, 2002, J. Phys.: Condens. Matter **14**, 729. 71

Tokar, V. I., and R. Monnier, 2007, cond-mat/0702011. 47

Toschi, A., A. A. Katanin, and K. Held, 2007, Phys. Rev. B **75**, 045118. 47, 63

Vilk, Y., L. Chen, and A.-M. Tremblay, 1994, Phys. Rev. B **49**, 13267. 9

Vilk, Y., and A.-M. Tremblay, 1997, cond-mat/9702188. 69, 99

Werner, P., A. Comanac, L. de'Medici, A. J. Millis, and M. Troyer, 2005, cond-mat/**0512727**. 25, 26, 32, 89

Werner, P., and A. J. Millis, 2006, Phys. Rev. B **74**, 155107. 25, 26, 32, 34, 89

Acknowledgments

Today, at the stage of my graduation, I would like to thank all the persons who contributed to my education in Bonn.

My deepest gratitude goes to Hartmut Monien. As my advisor, his encouragement at times when I was full of frustration, his tolerance for my inefficiency, his friendship and also his protection greatly benefits me. Being his student is wonderful. I still remember the first discussion I had with him, the first physics problem he explained to me and the first lecture I heard. I greatly appreciate him for introducing me to this interesting project. He always believes in me no matter the results is expected or not. I have always been fascinated by his great physical intuition and achievements in so many fields, which inspires and enriches my growth as student. To be a scientist like him is my dream. I adore him more than he knows.

Being a member of the Bonn Cologne Graduate School (BCGS), I want to thank Dr. Thrun and Ms. Weiss for their administrative work. Being a member of this graduate school is an honor to me. I have enjoyed the discussion and the relaxed atmosphere in this big family. But I need to apologize for my being dilatory in learning German. Special thanks go to Prof. Krug of Cologne university. Being my second mentor in BCGS, his suggestions and advice about how to start academic research gave me a lot of help. I have enjoyed the meetings and discussions with him every time.

Many thanks to our secretaries D. Fassbender, P. Zuendorf, Dr. Andreas Wisskirchen and all the faculty members in the Physics Institute. Without their help, my studying and living here would have been full of trouble. I appreciate Ms. P. Zuendorf sharing her family stories with me on the way to PI. I want to thank Dr. Andreas for his help on the computer. He is a really nice person whom one want to make friends with.

I want to thank Xiaobin Cao, Yesenia Arredondo Leon and Hunpyo Lee, to work and collaborate with them was a great joy. I want to emphasize my great gratitude to Yesenia. I want to thank her for the useful suggestions about the Ph.D defence and her endless help for taking care of my documents and all the necessary trivial details concerning my promotion when I was not in Bonn. Without her, I can not imagine how hard the promotion is for me who do not understand German. I also want to thank all my Chinese friends in Bonn, their friendship drove away my loneliness. I enjoyed every dinner party and hiking with them.